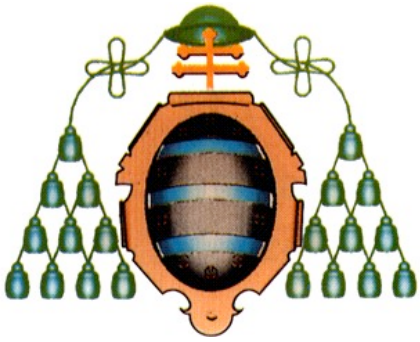

UNIVERSIDAD DE OVIEDO

Programa de Doctorado en Materiales

Magneto-transport properties of manganite/secondary phase inhomogeneous systems

TESIS DOCTORAL

Abdelmoez Ahmed Mohammed Ahmed Hussein

Enero 2017

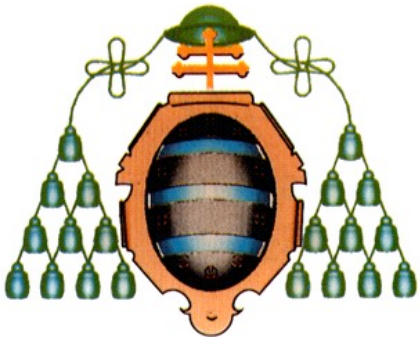

UNIVERSIDAD DE OVIEDO

Programa de Doctorado en Materiales

Magneto-transport properties of manganite/secondary phase inhomogeneous systems

TESIS DOCTORAL

Blanca Hernando Grande

Ahmed Mohamed Ahmed Aly

RESUMEN DEL CONTENIDO DE TESIS DOCTORAL

1.- Título de la Tesis	
Español: Propiedades de magnetotransporte de sistemas inhomogéneos manganita/fase secundaria.	Inglés: Magneto-transport properties of manganite/secondary phase inhomogeneous systems.

2.- Autor	
Nombre: Abdelmoez Ahmed Mohammed Ahmed Hussein	Pasaporte:
Programa de Doctorado: Materiales	
Órgano responsable: Departamento de Ciencia de los Materiales e Ingeniería Metalúrgica.	

RESUMEN (en español)

Se ha estudiado la influencia de la granularidad artificial en las propiedades relacionadas en manganitas, introduciendo fases secundarias en una manganita ferromagnética, obteniéndose así un sistema inhomogéneo *manganita/fase secundaria*. El aislante TiO_2 se adicionó a la manganita ferromagnética $La_{0.7}Ba_{0.3}MnO_3$ (LBMO) en proporciones: x=0.02, x=0.04, x=0.06 y x=0.08, en el sistema LBMO/*x*TiO_2. TiO_2 precipita en las fronteras de grano de LBMO aumentando su resistencia (R). Dicho incremento disminuye la conducción apareciendo el fenómeno de "spin-tunneling", originándose el efecto de magnetorresistencia (MR) a bajo campo. El valor máximo para LBMO se incrementa desde un 3% hasta -3.3 %, -3.5 % y -3.7%, con las adiciones de TiO_2: x= 0.02, 0.04 y 0.06. Las propiedades magnetocalóricas (MC) del sistema compuesto mejoran notablemente, manteniendo el rango de temperatura de trabajo. La potencia de enfriamiento se incrementa desde 35 J/kg hasta 51 J/kg, 47 J/kg, 50 J/kg y 49 J/kg con las adiciones de TiO_2: x=0.02, 0.04, 0.06 and 0.08, en un campo magnético de 1.5 T. Se analizó la influencia de la temperatura de recocido sobre las propiedades MC del sistema LBMO/*x*TiO_2, observándose que se modifica la distribución de TiO_2 en las fronteras de grano de LBMO variando sus propiedades magnéticas. El sistema LBMO/*x*TiO_2 fue recocido a 600ºC y 800ºC; a 800ºC condujo a respuestas magnéticas y MC óptimas. Se adicionó Ni en polvo, nanohilos de Ni, nanopartículas de Ag, y Ag oxidada en polvo en LBMO, comprobándose que la variación en la R de las fronteras de grano y las propiedades derivadas dependen del tamaño de la fase. La capacidad de refrigeración de 44 J/kg de LBMO se incrementa a 107 J/kg con Ni en polvo, y a 167 J/kg con nanohilos de Ni. Se analizó la correlación entre las propiedades MC y de transporte en LBMO. El orden/desorden de spin determina el efecto MC, MR y R a temperatura de Curie. El efecto MC puede ser escalado por R a T_c, y por MR mediante un factor K.

RESUMEN (en Inglés)

We have studied the artificial granularity effect on related properties in manganites, by introducing secondary phases into a ferromagnetic manganite forming an inhomogeneous *manganite/secondary phase* system. TiO_2 insulator was introduced as a secondary phase into the ferromagnetic $La_{0.7}Ba_{0.3}MnO_3$ (LBMO) manganite with ratios (x=0.02, x=0.04, x=0.06 and x=0.08) forming the LBMO/*x*TiO_2 system. TiO_2 precipitates at the grain boundaries of the LBMO increasing their resistance (R), and decreasing the conduction leading to the spin tunneling effect and the low field magnetoresistance (MR) effect, whose peak value for LBMO is enhanced from 3% to -3.3 %, -3.5 % and -3.7% with TiO_2 addition for x= 0.02, 0.04 and 0.06 ratio. An improvement in magnetocaloric (MC) properties in comparison with LBMO at the same working temperature is observed. Its relative cooling power is promoted from 35 J/kg to 51 J/kg, 47 J/kg, 50 J/kg and 49 J/kg with the introduced TiO_2 for x=0.02, 0.04, 0.06 and 0.08, at 1.5T applied field. Annealing is found to modify the TiO_2 distribution at the grain boundaries of the LBMO leading to a change in magnetic and MC properties. LBMO/*x*TiO_2 system was annealed at 600 °C and 800 °C. Annealing at 800 °C promotes the best magnetic and MC properties. Secondary phases including Ni powder, Ni nanowires, Ag nanoparticles and Ag oxide were introduced into LBMO. The change in grain boundaries R results a secondary phase size-dependent effect, which makes related properties also size-dependent ones. An improvement in the MC properties is observed. The refrigerant capacity power value of LBMO is improved from 44 J/kg to 107 J/kg for Ni powder and to 167 J/kg for Ni nanowires introduction. MC and transport properties correlation was found. The spin order/disorder determines MC effect, MR and R at Curie temperature. The MC effect can be well scaled by R at T_c, and by MR through a K factor.

SR. PRESIDENTE DE LA COMISIÓN ACADÉMICA DEL PROGRAMA DE DOCTORADO EN MATERIALES

To my later mom and little Misses Rania & Reham

Acknowledgments

In the next few words, I would like to thank and express my gratitude to everybody who supported or helped me in this work.

I would like to thank the supervisors **Prof. Blanca Hernando Grande** for the real support, help, guidance and the fruitful discussions, and **Prof. Ahmed Mohamed Ahmed Aly** for discussions.

It was a pleasure to work in the *Magnetic Materials and Nanomaterials* research group in Department of Physics, Oviedo University with ***Prof. Agustín Antonio Fernández Suárez, Prof. Victor Manuel del la Prida Pidal, Dr. Victor Vega and Dr. Rafael Caballero-Flores***. I enjoyed too much their colleagueship and appreciate their continuous assistance in work.

I also would like to acknowledge the technical support provided by other research groups in sample preparation and some measurements. **Prof. Marta Ellena M. E. Díaz-García, Jorge and Christian** in Department of Physical and Analytical Chemistry, Faculty of Chemistry. **Prof. Julián González Estévez** and **Dr. Mihail Ipatov,** Applied Physics I Laboratory, Department of Physics and Materials University of País Vasco UPV/EHU, San Sebastián-Donostia. ***Prof. Francisco Rivadulla Fernández*** in center of Biological chemistry and Molecular Materials Investigation (CIQUS), University of Santiago de Comostela.

I would like to acknowledge the work financial support provided by the Spanish MINECO Ref. MAT201347231-C2-1-P and MAT2013-48054-C2-2-R, by the Asturias Government Ref. FC-15-GRUPIN14-085 research projects. Also I acknowledge my own financial support provided by the Egyptian Ministry of Higher Education.

I greatly thank **Prof. Blanca Hernando, Victor Vega** and **R. Caballero-Flores** for the very nice time and the continuous assistance in general life in Oviedo, and I specially thank my friends **M. El-Sharouny, M. Salah, M. Hamdy, Abdallah** and **Ali** who have kept in touch despite the far away distance.

Finally, I would like to express my deep gratitude to the family my **dad**, **later mother**, elder brothers **Moutaz**, **Moutasem** and little sisters **Rania** &**Reham**.

Abstract

The magnetoresistive and magnetocaloric properties of manganite compounds have drawn much attention due to their technological applications. The granularity effect plays a key role in almost of all manganites properties. Accordingly, in this work we have studied the artificial granularity and its effect on the related properties in manganites. This has been achieved by introducing secondary phases into a ferromagnetic manganite material forming an inhomogeneous *manganite/secondary phase* system.

TiO_2 insulator was introduced as a secondary phase with the ferromagnetic $La_{0.7}Ba_{0.3}MnO_3$ manganite compound with different ratio (x=0.02, x=0.04, x=0.06 and x=0.08) forming the $La_{0.7}Ba_{0.3}MnO_3/xTiO_2$ system. TiO_2 insulator precipitates at the grain boundaries of the $La_{0.7}Ba_{0.3}MnO_3$ compound increasing their resistance. The increase in the grain boundaries resistance decreases the conduction leading to the spin tunneling effect, which in turn results in the low field magnetoresistance effect. Moreover, the low field magnetoresistance effect peak value of $La_{0.7}Ba_{0.3}MnO_3$ compound is enhanced from 3% to -3.3 %,-3.5 % and -3.7% with TiO_2 addition for x= 0.02, 0.04 and 0.06 ratio, respectively. A notable improvement in the magnetocaloric properties of the $La_{0.7}Ba_{0.3}MnO_3$ compound at the same working temperature range has been also observed. Its relative cooling power is promoted from 35 J/kg to 51 J/kg, 47 J/kg, 50 J/kg and 49 J/kg with the TiO_2 introduction for x=0.02, 0.04, 0.06 and 0.08, respectively, at 1.5T applied magnetic field. The annealing temperature influence on the magnetocaloric properties of the $La_{0.7}Ba_{0.3}MnO_3/xTiO_2$ is studied. The annealing treatment is found to modify the

TiO_2 distribution at the grain boundaries of the $La_{0.7}Ba_{0.3}MnO_3$ leading to a change in the magnetic properties. In this work, $La_{0.7}Ba_{0.3}MnO_3/xTiO_2$ system was annealed at two selected temperatures of 600 $^{\circ}$C and 800°C. The experimental results show that the annealing process at the higher temperature of 800°C promotes the best magnetic and magnetocaloric properties, which are mentioned before.

In addition to the secondary phase ratio effect, the secondary phase size influence on granularity and related properties was studied. Secondary phases in different sizes including Ni powder, Ni nanowires, Ag nanoparticles and Ag oxide were introduced into the $La_{0.7}Ba_{0.3}MnO_3$ compound. In this case, the change in grain boundaries resistance was found to be a secondary phase size-dependent effect, which makes the other related properties also size-dependent properties. For instance, the room temperature magnetoresistance of $La_{0.7}Ba_{0.3}MnO_3$ compound is changed from -1.23% to -5.25 % and -7.9 % with Ag nanoparticles and Ag oxide secondary phases introduction, respectively. Furthermore, an improvement in the magnetocaloric properties is observed but depends on the introduced secondary phase size, since, the RCP value of $La_{0.7}Ba_{0.3}MnO_3$ compound is improved from 44 J/kg to 107 J/kg Ni powder and to 167 J/kg for Ni nanowires introduction.

A correlation between the magnetocaloric effect and transport properties was analyzed in the $La_{0.7}Ba_{0.3}MnO_3$ compound. The spin order/disorder feature plays an important role in the magnetocaloric effect, magnetoresistance and resistivity behavior around the Curie temperature. The obtained results show that the magnetocaloric effect can be well scaled by the electrical resistivity around T_c, and by the magnetoresistance through a K factor.

Resumen

Las propiedades magnetoresistivas y magnetocalóricas de los compuestos de manganita, presentan un enorme interés desde el punto de vista de aplicaciones tecnológicas. El carácter granular juega un papel fundamental en la mayoría de las propiedades de las manganitas. En consecuencia, en este trabajo se ha estudiado la influencia de la granularidad artificial en las propiedades relacionadas con la misma en manganitas. El método utilizado en este estudio, ha sido la introducción de diversas fases secundarias en un material de manganita ferromagnética, obteniéndose así un sistema inhomogéneo *manganita / fase secundaria*.

El aislante TiO_2 se introdujo en el compuesto de manganita ferromagnética $La_{0.7}Ba_{0.3}MnO_3$ con diferentes adiciones: x=0.02, x=0.04, x=0.06 y x=0.08, correspondientes al sistema $La_{0.7}Ba_{0.3}MnO_3/xTiO_2$. El aislante TiO_2 precipita en las fronteras de grano del compuesto $La_{0.7}Ba_{0.3}MnO_3$ aumentando su resistencia. El incremento en la resistencia de las fronteras de grano disminuye la conducción apareciendo el fenómeno de "spin-tunneling", que a su vez origina el efecto de magnetorresistencia a bajo campo. Además, el valor máximo del efecto de magnetorresistencia a bajo campo para la manganita $La_{0.7}Ba_{0.3}MnO_3$ se incrementa desde un 3% hasta
-3.3 %, -3.5 % y -3.7%, con las adiciones respectivas de TiO_2: x= 0.02, 0.04 y 0.06. Simultáneamente se ha observado una mejora notable en las propiedades magnetocalóricas del sistema compuesto en comparación con las de la manganita citada, y en idéntico rango de temperatura de

trabajo. La potencia de enfriamiento se incrementa desde 35 J/kg hasta 51 J/kg, 47 J/kg, 50 J/kg y 49 J/kg con las adiciones de TiO_2 respectivas: x=0.02, 0.04, 0.06 and 0.08, en un campo magnético aplicado de 1.5 T.

También se ha analizado la influencia de la temperatura de tratamientos térmicos sobre las propiedades magnetocalóricas del sistema $La_{0.7}Ba_{0.3}MnO_3/xTiO_2$. Se ha observado que el tratamiento de recocido modifica la distribución de TiO_2 en las fronteras de grano de $La_{0.7}Ba_{0.3}MnO_3$ variando sus propiedades magnéticas. En este trabajo, el sistema $La_{0.7}Ba_{0.3}MnO_3/xTiO_2$ fue recocido a dos temperaturas específicas: 600ºC y 800ºC. Los resultados experimentales demostraron que el proceso de recocido realizado a la temperatura más elevada, 800ºC en este caso, conduce a la respuestas magnética y magnetocalórica óptimas mencionadas anteriormente.

Aparte del efecto debido a la proporción de fase secundaria sobre la granularidad y las propiedades relacionadas con ella, se ha estudiado la influencia del tamaño de dicha fase en el comportamiento magnético y de magnetotransporte del sistema inhomogéneo. Para ello, se adicionaron fases secundarias con tamaños diferentes tales como Ni en polvo, nanohilos de Ni, nanopartículas de Ag, y Ag oxidada en polvo en la manganita $La_{0.7}Ba_{0.3}MnO_3$. Así, se pudo comprobar como la variación en la resistencia de las fronteras de grano depende del tamaño de la fase secundaria, y de forma que las propiedades relacionadas dependen también de dicho parámetro. Por ejemplo, la magnetorresistencia a temperatura ambiente de $La_{0.7}Ba_{0.3}MnO_3$ de -1.23% aumenta, respectivamente, a -5.25 % y a -7.9 % con la adición como fase secundaria de nanopartículas de Ag y de Ag oxidada en polvo. Respecto

a la respuesta magnetocalórica, se optimiza también dependiendo del tamaño de la fase secundaria puesto que la capacidad de refrigeración de 44 J/kg del compuesto $La_{0.7}Ba_{0.3}MnO_3$ se incrementa hasta 107 J/kg con la introducción de Ni en polvo, y hasta 167 J/kg al adicionar nanohilos de Ni.

Se ha analizado una correlación entre las propiedades magnetocalóricas y de transporte en la manganita $La_{0.7}Ba_{0.3}MnO_3$. El orden/desorden de spin influye de forma determinante en el efecto magnetocalórico, en la magnetorresistencia y en el comportamiento de la resistividad en el entorno de la temperatura de Curie. Los resultados obtenidos muestran que el efecto magnetocalórico puede ser escalado por la resistividad eléctrica alrededor de T_c, y por la magnetorresistencia mediante un factor K.

Contents

CH.1 Introduction

Pervoskite doped manganites with the $A_{1-x}B_xMnO_3$ formula (A is a rare earth element and B is a divalent or monovalent ion) were discovered for first time in 1950 by *G. H Jonker* and *J. H. Van Santen* [1]. These materials exhibit an interesting correlation between their electrical and magnetic properties, where, resistivity (ρ) shows a metal-semiconductor transition near the Curie temperature (T_c) as can be seen in Fig. 1.1. This correlation was explained by Zener double exchange (DE) model [2]. Manganites oxides interest with several outstanding phenomena associated with their structural, electrical and magnetic properties as the colossal magnetoresistance (CMR) [3] and the magnetocaloric effect (MCE) [4] phenomena. Several fundamental studies have proved that the electro-magnetic response of manganites relies on the mixed valence state Mn^{3+}/Mn^{4+} that plays a key role in the DE mechanism, the Mn-O-Mn angle and the e_g electron mobility. Various complicated interactions are involved in these oxides among charge, spin, orbital and lattice as DE interaction, superexchange interaction and Jahn-Teller lattice distortion. Such interactions and distortions take part in the electro-magnetic properties of these materials and the related phenomena as phase separation, charge ordering, half metallicity, and magnetoresistive properties [5].

In principal, the potential applications of manganites depend on their sensitivity to the applied magnetic fields. This has stimulated the efforts to investigate various doping ions in **A** and **B** sites as La-Ba-Mn-O [6], Sm-Sr-Mn-O [7] and Nd-Pb-Mn-O [8] compounds. In addition, some attention has been paid to explore the effect of Mn site partial substitution on the magnetoresistive properties. Positively, the CMR have shown a high sensitivity to this process,

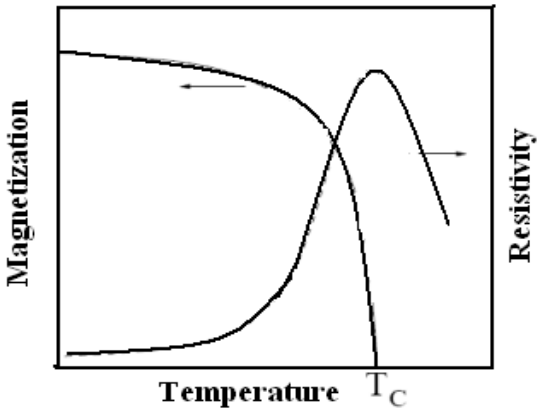

Fig. 1.1: Magnetic-transport properties correlation in manganites.

being notably enhanced as reported in several works [9]. Only one difficulty that faces the CMR technological implementations, which is that the CMR effect can be only triggered at several Tesla of applied magnetic field. Therefore, the attention has focused on another kind of MR that is called the low field MR (LFMR). Numerous works have discussed the appearance of LFMR in granular manganites pointing to the grain boundaries (GBs) relevant role [10]. This discovery has increased the interest in GBs synthesis and their modification either by annealing process [11], preparation methods [12] or artificial defects [13]. Granularity promotion by artificial defects is the most prominent method that has shown a good LFMR promotion. It can be simply performed by introducing interfaces or secondary phases into ferromagnetic manganites materials [14] as $La_{0.7}Sr_{0.3}MnO_3/ZrO_2$ [15], $La_{0.67}Ca_{0.33}MnO_3/ZnO$ [16] and $La_{0.67}Ba_{0.33}MnO_3/YSZ$ [17] systems.

The LFMR mechanism has been carefully studied and attributed to the spin polarized tunneling and scattering process across GBs according to the

polarization ability [18]. It is noteworthy to state that the highest LFMR values are observed below T_c due to the extrinsic nature of this MR effect, however, the room temperature LFMR values are still suitable for some technological applications [19].

Another magnetic feature shown by manganites oxides is the change in entropy under the effect of magnetic field application/removal, which is used in MCE applications as in magnetic refrigeration technology. Recently, the interest in magnetic cooling has been increased especially after clean energy devices have been claimed in comparison with the conventional gas compression mode ones [20]. This new refrigeration technique interests with several prominent features as the high efficiency, the energy saving and the environmental friendly effects. In spite of the numerous magnetic materials that have been explored for the MCE applications, the Gd rare earth metal is considered as the most promising room temperature refrigerant element [21]. However, its usage is limited due to some disadvantages such as the high cost and the toxicity. As magnetic materials, manganites have been investigated for magnetic cooling technology, and have shown a notable MCE response around their T_c [22]. The interest in manganites may refer to their outstanding physico-chemical properties as the high magnetization, the high T_c, the chemical stability, the simple preparation methods, the low cost and the low magnetic hysteresis that have put these materials in comparison with Gd and its based alloys [23, 24]. For example, $La_{0.7}Ca_{0.3}MnO_3$ shows a MCE response of 5.27 J/kg.K at 1.5T applied magnetic field, which is nearly twice larger than the Gd based alloys in low magnetic fields [25],

and $La_{0.87}Sr_{0.13}MnO_3$ shows 5.8 J/kg.K at 5T [26]. In addition to the observed enhancement in the MCE with the partial substitution of Mn ion by other elements as Sn, Ti and Cr [27].

CH. 2 Phenomena and concepts

The tremendous phenomena in manganites are governed by structural and electro-magnetic interactions. This chapter discusses the most important concepts in manganites to have a deep understanding of the related phenomena.

2.1 Electronic Structure

Manganites are pervoskite structured oxides, which is a sublattice unit cell as shown in Fig. 2.1a. This is an ideal pervoskite unit cell, where **A** & **B** ions occupy the cube corners, Mn ion locates in the cube center and **O** atom occupies the cube faces forming an octahedral shape with Mn ion (MnO_6) [28]. The isolated Mn atom has 25 electrons with an incomplete *d* shell ($3d^5$). The *d* orbital spins are aligned in parallel, maintaining *Hund's* rule and keeping the system at the minimum energy. This configuration may be somewhat different in the non isolated Mn atom. For example, in MnO_6 octahedra there is an induced energy arising from the crystal field that leads to system instability. To get rid of this energy excess, the adjacent *d* orbitals have to degenerate into two energy sets of orbitals (see Fig. 2.1b). The energy sets are a lower energy triple set ($\boldsymbol{t_{2g}}$) of d_{xy}, d_{yz}, d_{zx} levels and a higher double energy set ($\boldsymbol{e_g}$) with d_x^2-$_y^2$, d_{3Z}^2-$_r^2$ levels. Mn^{3+} ion has 4 electrons in the *d* orbital distributed as 3 electrons in the $\boldsymbol{t_{2g}}$ (*t-core*) and one electron in the $\boldsymbol{e_g}$ band. The $\boldsymbol{e_g}$ band plays an important role in the conduction, where, it overlaps with the *P-level* of oxygen atom forming the conduction band [29]. In addition, the $\boldsymbol{e_g}$ electron is a loosely bounded state that can freely itinerate between Mn ions controlling the conduction and the related properties [30].

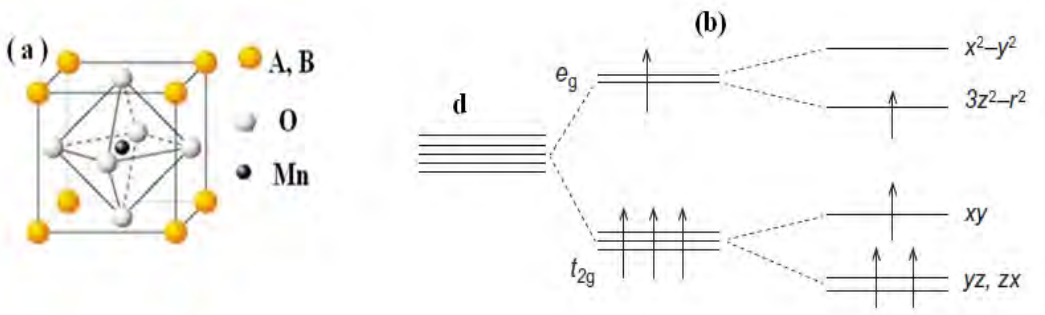

Fig. 2.1: (a) The pervoskite unit cell structure and (b) *d* level splitting.

$AMnO_3$ parent compound is an antiferromagnetic insulator with an orthorhombic structure [31,32]. It mainly contains Mn^{3+}, which is a Jahn-Teller (JT) distortion active ion and this may be the reason for the insulating nature of this compound. As **A** ions are partially substituted by **B** ions, Mn^{4+} ions are induced with the same substitution ratio. In this case, two oxidation states of Mn ion exist in the system (Mn^{3+} and Mn^{4+}) that is called a mixed valence state. The presence of Mn^{4+} ion enhances the orthorhombic crystal structure of the parent compound to the rhombohedral one that is characterized by the easy carrier transport [33], because Mn^{4+} is an inactive ion for JT distortion. This change in the crystal structure improves the electrical properties through the e_g electron itineration between Mn^{3+} and Mn^{4+} ions, which drives $AMnO_3$ to ferromagnetism. The ferromagnetism of these oxides is a compositional dependent property starting at an optimal value of x (Mn^{4+} content), and only these intermediate compositions are ferromagnetics and undergo the metal-insulator transition. Whereas, x=0 and x=1 compounds are neither ferromagnetics nor good electrical conductors, in contrast, they are semiconductors due to the mixed valence state absence.

2.2 Percolation and phase separation

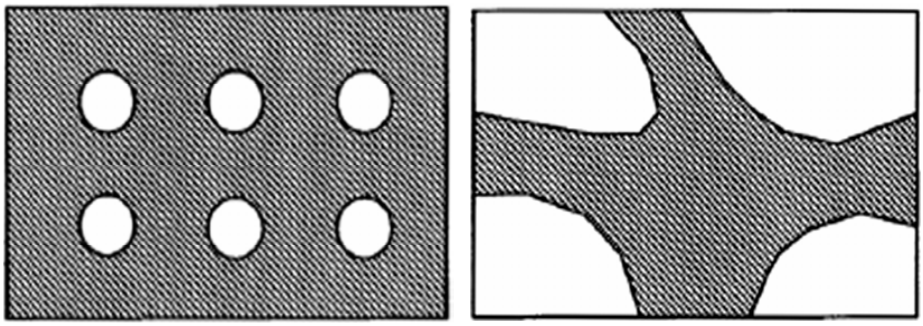

Fig. 2.2: The shaded area is the FM regions, while the white islands are the AFM insulating phase.

The partial substitution of **A** ions by **B** ions creates a hole in the pervoskite unit cell that increases in number with increasing **B** doping level (x). The adjacent holes percolate with each other forming clusters that increase in size with increasing doping level, and at a certain doping ratio (percolation threshold), the ferromagnetic phase is formed (see Fig. 2.2). This inhomogeneity introduces the phase separation concept. Phase separation means a coexistence of different phases with different structural, electronic and magnetic properties. In manganites, it appears as a coexistence of an antiferromagnetic phase with the main ferromagnetic one at distinct doping values. Phase inhomogeneity is observed in the purest single crystal that makes its origin an ambiguous matter, however, it is useful in some phenomena as the exchange bias effect [34]. These insulating phases can be static and sometimes affected by temperature changes [35] and magnetic fields [36]. Besides the DE interaction, percolation and phase separation managed to explain the metal-insulator resistivity transition [37] and present an acceptable explanation for the CMR effect in manganites.

2.3 Interactions in manganites

2.3.1 Double exchange interaction (DE)

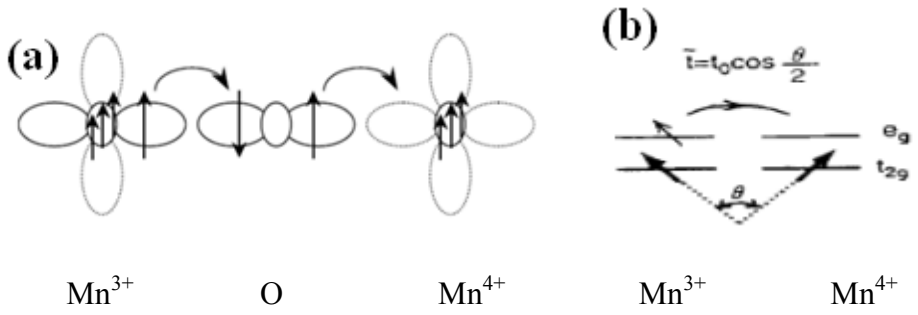

Fig. 2.3: (a) The DE interaction and (b) the transfer integral angle dependence.

In 1951, *Zener* succeeded to explain the electro-magnetic correlation in manganites oxides by the so called DE interaction [2]. This model depends on the valence exchange between Mn^{3+} and Mn^{4+} ions. *Zener* visualized hole transfer between the adjacent Mn ions as following: the $\boldsymbol{e_g}$ electron transfers from the Mn^{3+} ion to the oxygen atom then to the Mn^{4+} ion, and vice-versa (see Fig. 2.3a). These simultaneous two processes are called the DE model. In such systems, these exchange interactions can be infinite only in case of the parallel alignment of the *t-core* spins for both Mn^{3+} and Mn^{4+} ions (pointing in the same direction). This is because the spin direction cannot be changed during hopping process, and according to *Hund's* rule the anti alignment of the unpaired electrons is not allowed. Fundamentally, the *t-core* electrons are localized and cannot participate in conduction, whereas, $\boldsymbol{e_g}$ electrons may be localized or itinerant. Only $\boldsymbol{e_g}$ electrons can participate in conduction through hopping process that becomes easier in the Mn *t-core* parallel alignment spins (up or down). *P. W. Anderson and H. Hasegawa* [38] have suggested the $\boldsymbol{e_g}$ electron transfer dependence on the

relative angle between the two Mn *t-core* spins (θ) (as seen in Fig. 2.3b). This has been illustrated mathematically as $t_{ij} = t_0 \cos(\theta_{ij}/2)$, where, t_{ij} is known as the *transfer integral*, which reveals the DE strength dependence on the transfer integral.

2.3.2 Superexchange interaction (SE)

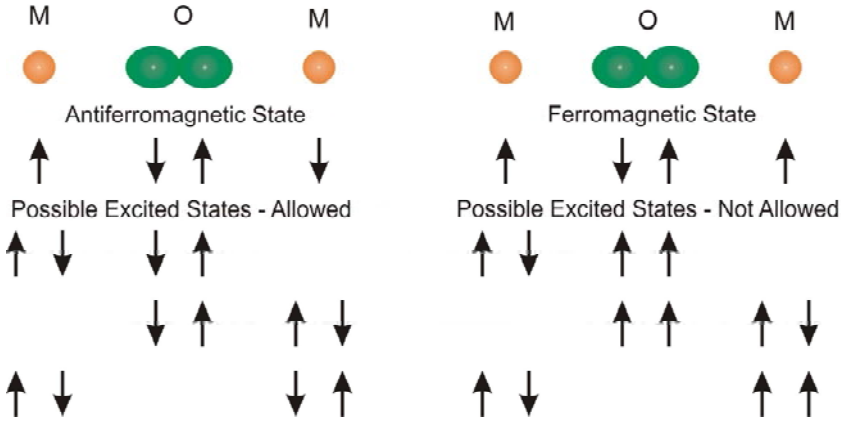

Fig. 2.4: The superexchange interaction

Besides the DE interaction, ferromagnetism in manganites oxides may be driven by the SE interaction [39]. This interaction was suggested by *H. A. Kramer* [40] to explain the magnetic properties of transition metal oxides. SE is an indirect interaction occurs between non neighboring magnetic ions (Mn) with the same valence separated by a non magnetic ion (O). This interaction happens when the distance between magnetic ions is too large for the direct exchange interaction. The SE interaction is an electronic exchange between Mn ions from the same *2p* oxygen orbital that has antiparallel spins according to Pauli exclusion principle leading mostly to antiferromagnetism. The SE interaction occurs only when the *t-core* spins of the magnetic ions show anti-parallel alignment. Because this is the

only case that preserves Pauli exclusion principle, where the electronic transfer breaks this principle in the parallel alignment of *t-core* spins as can be seen in Fig. 2.4. Whereas, if the two magnetic ions are in an antiparallel alignment, the transfer between them will be available. Sometimes, SE interaction leads to a ferromagnetic coupling, this happens only when electrons from the magnetic ions interact with electrons from different orbitals in the oxygen atom [41].

2.4 Distortions

Ionic size, crystal field and cation displacement are crucial parameters in the pervoskite structure formation, which make such ideal structure is hard to be obtained and instead a lot of distortions are induced. In this part, we discuss some of these distortions that face the ideal pervoskite structure.

2.4.1 MnO_6 octahedra tilting

Ionic size mismatch among A, B and Mn ions may lead to structure instability and result in a distorted pervoskite unit cell. As a measurement of this ionic size mismatch, the tolerance factor (F) in Eq. 2.1 was suggested by *V. Goldschmidt* [42], r_A is the A ionic radius, r_B is the B ionic radius, r_O is the Oxygen ionic radius and r_{Mn} is the Mn ionic radius. The ideal pervoskite structure has F=1 due to the well matching between ions radius and the same equilibrium distances among each others. Actually, various ions have different ionic size, and to maintain the system minimum free energy ions should move away from their essential site to new equilibrium positions. This creates free spaces in the lattice, and the MnO_6 octahedra have to rotate or tilt to fill this space leading to a change in the Mn-O and the (A,B)-O distances, which in turn changes F from unity and deforms the pervoskite unit cell. This distortion decreases angle between ions

$$F = \frac{(\langle r_{A,B}\rangle + r_O)}{\sqrt{2}(\langle r_{Mn}\rangle + r_O)} \qquad (2.1)$$

That affects carriers hopping amplitude, mobility and localization. The tolerance factor can be considered as a measurement of the pervoskite structure stability, since the stable pervoskite structure can be formed in the 0.89<F<1.02 range [43].

2.4.2 Jahn-Teller (JT) distortion

In MnO_6 octahedra, the *3d* levels of Mn ion are splitted into the e_g and the t_{2g} sets due to the crystal field. According to JT theory, this is an unstable system with energy excess. The system tends to get rid of this energy excess by spontaneous deformation through an additional splitting in both e_g and t_{2g} sets as shown in Fig. 2.5a [44]. This effect is known as JT distortion, which controls the e_g electron localization and the insulating phase stabilization. It is important to say that JT distortion is mainly related to the Mn^{3+} ions and not to the Mn^{4+} ions (see Fig. 2.5b). There are three types of JT distortion Q_1, Q_2 and Q_3 modes according to the distortion shape and direction (see Fig. 2.5c). Q_3 distortion mode is a longitudinal distortion occurs along the $d_{3z^2-r^2}$ orbitals and it is accompanied by a contraction in the $d_{x^2-y^2}$ orbital direction. This leads to an increase in the two long Mn-O bonds length and decreases the four short Mn-O bonds length [45]. Q_2 distortion is an orthorhombic distortion mode, where the two long Mn-O bonds length is constant. However, the variation occurs only in the tetrahedral shape, where, every two opposite oxygen atoms move towards each other and simultaneously the other opposite two oxygen atoms move outwards and vice-versa. Q_1 distortion mode is called breathing distortion, where, it results from the difference in the octahedra sizes due to the difference in Mn^{3+} and Mn^{4+} ionic size

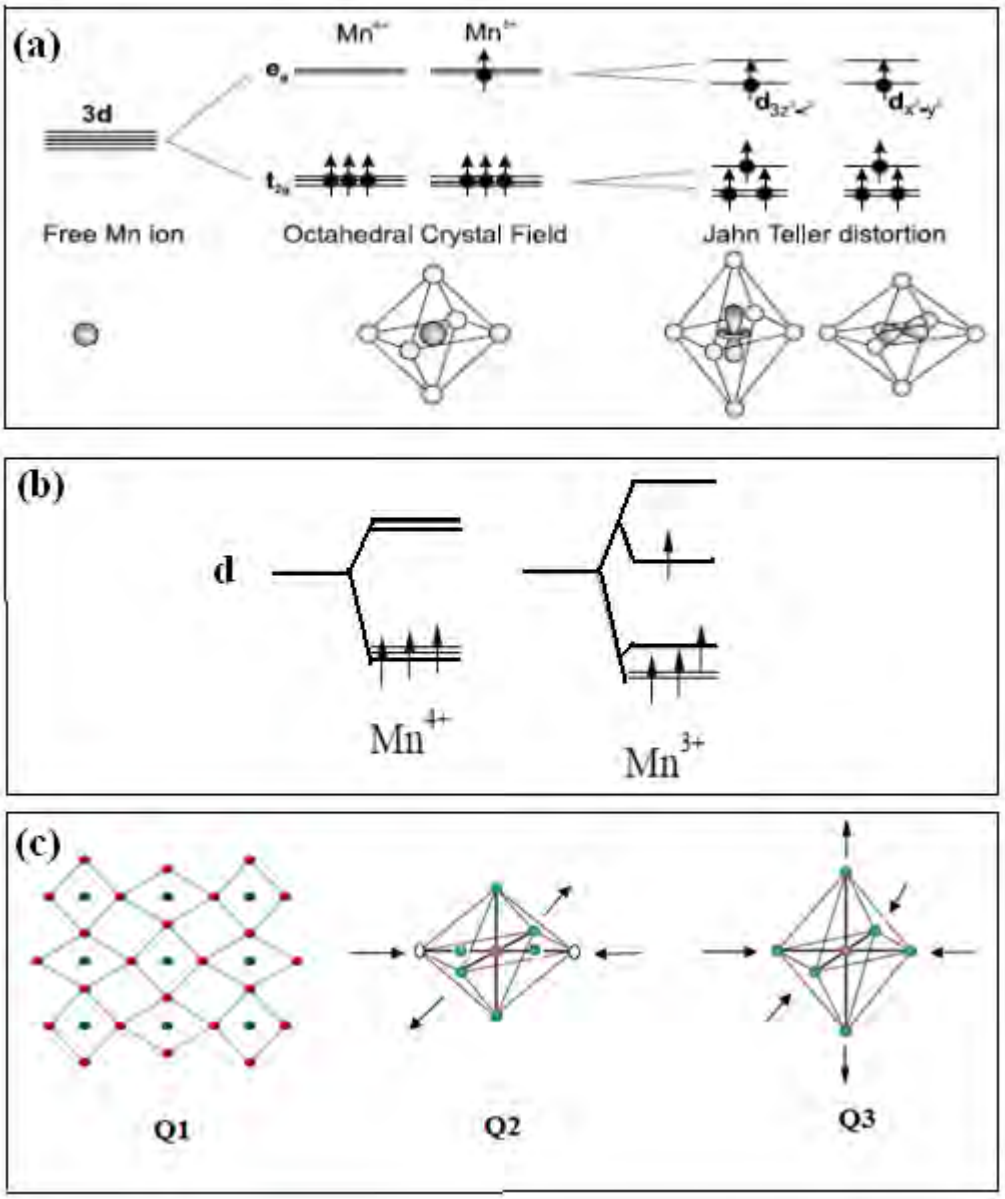

Fig. 2.5: (a) The deformation stages in MnO_6 Octahedra, (b) effect of Jahn-Teller distortion on Mn^{3+} and Mn^{4+} ions and (c) Jahn-Teller distortion modes.

2.4.3 Polaron

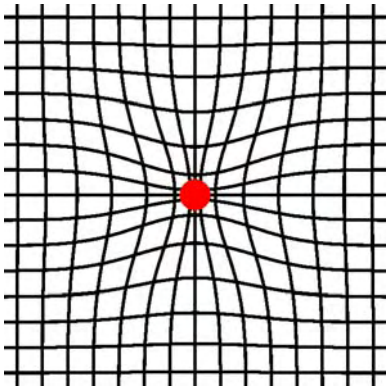

Fig. 2.6: Schematic plot for the Polaron concept, the red circle represents a charge and the black lines are the lattice.

Polaron is a quasi-particle consisting of a charge and a local distortion. Basically, the electron existence near an ion for some time deforms the lattice. In the *3d* metals, the average life-time of an electron near an ion is 10^{-15} seconds, which is a very short time for crystal polarization. If the electron life-time increases by any mechanism to 10^{-12} seconds, the electron can be attracted by positive ions and pushed away by negative ions. As a consequence, if the electron tries to move away, it will be forced to go back again to its initial position. When the electronic wave function is localized in the range of lattice parameters, the polaron is called "*small Polaron*", while, when the wave function is localized in a radius larger than lattice parameters it is called "*Large Polaron*". The small polaron model can be used to describe the conduction in ionic semiconductors, where there is a strong interaction between electron and lattice that lowers the electron mobility. In this case, the electron is being "self-trapped" in its own polarization field [46]. The polaron movement mechanism in lattice depends on the temperature range. At high temperatures, the polaron moves by hopping

mechanism leading to the thermal activated mobility [47] that requires a mixed valence state for occurrence [48], while at low temperatures, it moves through quantum tunneling.

2.5 Phenomena

2.5.1Magnetoresistance (MR)

MR is a change in the electrical resistivity under the effect of magnetic field application. It can be formulated as in Eq. 2.2, where, ρ_0 and ρ_H are resistivities in zero and non zero applied magnetic fields, respectively. This effect was discovered in ferromagnetic transition metals [49] as a directional dependent effect. This reveals the resistance change dependence on the angel between the applied magnetic field and the electric current direction (parallel or perpendicular), and this is known as the anisotropic magnetoresistance (AMR). Later, the magnetic and non magnetic multilayered compounds show a higher MR effect known as the "Giant magnetoresistance" (GMR) [50]. In 1993 and 1994, a huge MR was discovered in manganites oxides [51, 52], it was greater than the GMR effect and sometimes it closes to 100% being known as the colossal magnetoresistance (CMR). Many theories have been proposed to explain the CMR mechanism as DE, phase separation, Jahn-Teller distortion and polaronic effects. These theories have suggested the key role played by the Mn^{3+}/Mn^{4+} mixed valence state in the CMR phenomenon. The CMR is an intrinsic effect occurs around T_c, and arises from the spin disorder suppression under the effect of high magnetic field values, which retard their technological implementation. Relatively high values of MR have been observed in polycrystalline granular materials and multilayered manganites at low applied magnetic fields [18].

$$MR = \frac{\rho_{H-}\rho_0}{\rho_0} \qquad (2.2)$$

This is the case of LFMR, it is an extrinsic effect and has been attributed to carriers scattering and spin polarized tunneling across GBs [18]. Accordingly, some efforts have been devoted to polycrystalline and granular manganites in an attempt to enhance the LFMR, especially with artificial GBs that increase the spin tunneling and hence lead to the LFMR effect [53].

2.5.2 Magnetocaloric effect (MCE)

In an adiabatic process, magnetic field can cool or heat magnetic materials due to the variation in their internal energy. This is called the MCE effect, it can be generally defined as the temperature change of magnetic material due to magnetic field application/removal. In fact, the MCE property is associated with the magnetic entropy change (ΔS). To visualize this concept, let us consider a system of paramagnetic or ferromagnetic spins. The total entropy of this system consists of two components arising from the magnetic spin ordering and the lattice entropy responsible for system temperature. Magnetic field application aligns spins in parallel reducing the spin entropy, which are disordered by the thermal vibration. Thermodynamically and under adiabatic considerations, the system total entropy should be constant. Therefore, the decrease in magnetic spin entropy should be compensated by an increase in the lattice entropy, which in turn increases the temperature and heats up the material. The total entropy of magnetic material can be expressed as in Eq. 2.3 [54], where, $\boldsymbol{S_m}$ is the magnetic spin entropy, $\boldsymbol{S_L}$ is the lattice entropy and $\boldsymbol{S_e}$ is the electron entropy contributions in total entropy.

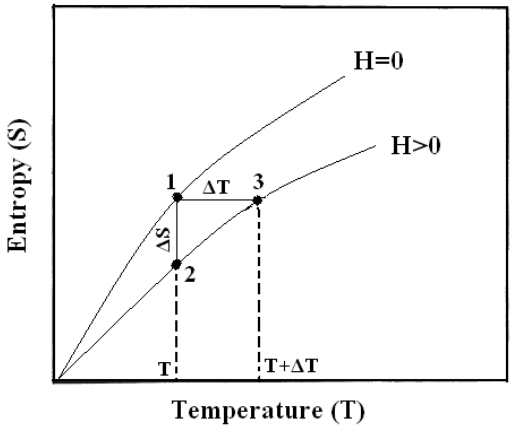

Fig. 2.6: Relation between entropy and temperature under magnetic field application.

$$S(H,T) = S_m(H,T) + S_L(H,T) + S_e(H,T) \quad (2.3)$$

$$\Delta S(H,T) = \Delta S_m(H,T) = S(H_1,T) - S(H_2,T) \quad (2.4)$$

$$\Delta S_m(H,T) = \int_0^H \frac{\delta M}{\delta T}\, dH \quad (2.5)$$

$$\Delta S(T, \Delta H) = \sum \frac{M_i - M_{i+1}}{T_i - T_{i+1}} \Delta H \quad (2.6)$$

$$RCP = \Delta S_{Max} \times \delta T_{FWHM} \quad (2.7)$$

Neglecting $\boldsymbol{S_e}$ component, Eq. 2.3 can be modified to Eq. 2.4, which can be expressed as the Maxwell equation in Eq. 2.5 [55]. In the small discrete fields and temperature intervals, Maxwell equation can be expressed as in Eq. 2.6 [56], M_{i+1} and M_i are the magnetization values measured at T_{i+1} and T_i temperatures in magnetic field change ΔH. Fig. 2.6 visualizes the MCE, where, magnetic field application decreases system entropy. Adiabatically, this can be imagined as two processes, the first one is the entropy change at a constant temperature (isothermal from 1→2) and the second is a temperature change from T to T+ΔT (isofield from 2→3). Both isothermal and isofield components contribute in the magnetic entropy change, magnetic field application decreases magnetic entropy and the

isofield component (2→3) leading to an increase in the MCE (ΔT_{ad}).

The efficient MCE material should interest with a high value of ΔS (ΔS_{max}) at a wide temperature range. Accordingly, the magnetic cooling efficiency or magnetic refrigeration of any system can be determined in terms of the relative cooling power (RCP) in Eq. 2.7 [57] that is pointing to the transferred heat between cold and hot reservoirs in a refrigerator during one ideal thermodynamic cycle [58], δT_{FWHM} is the full width at half maximum of ΔS vs. T curve.

CH. 3 Technological applications and current work

Pervoskite manganites oxides are suitable materials for many applications, for example, they can be used in bolometric applications as a result of the semiconductor-metal resistivity transition. Also, the high sensitivity to the applied magnetic fields enables manganites to be good applicants for magnetic sensing technology as spin valves and magnetoresistive sensors, which are more sensitive than Hall effect based sensors [59]. In this part, we will detail some of the most important manganites applications in various technologies.

3.1 Applications

3.1.1 Spin-valve read/write heads

In the past, hard disk drives were consisting of ferromagnetic metallic zones and one copper tip head used for both reading and writing processes. During writing process, electric current flows through the copper coil tip inducing magnetic field that aligns moments in the ferromagnetic zone and codes the information data into **1** bit. Vice-versa, in reading process an induced electric current flows through the copper tip when it passes over the aligned moments. The real problem is related to the storage capacity. The increase in storage capacity means an increase in bytes number per square inch, but they cannot be detected due to the weak sensitivity of the copper head tip. This problem is solved by the spin-valve write/read heads. The spin-valve read/write head consists of four layers (1) a ferromagnetic layer working as a sensor is called the *free layer* touching a disk without specific moment orientation. (2) A non magnetic layer is called the *spacer*. (3) A magnetic layer with a fixed moment orientation is called the *pinning layer*. (4) A protection insulator layer for the pinning layer from

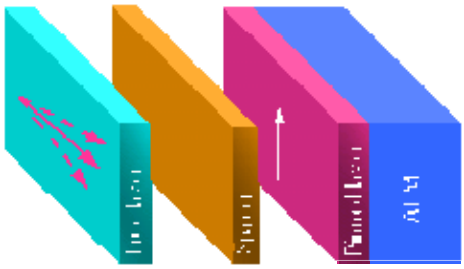

Fig. 3.1: The layers of the spin valve read/write head tip in hard disk drives.

external magnetic fields. When the free layer passes over a magnetized area on the disk, it changes its orientation to match this area. , The new orientation of the free layer spins can be in the same/opposite direction of the pinning layer. In the similar direction case, electrons can flow easily with low resistance, and then the computer computes **1** bit. In contrast, if case of the opposite orientation, electrons find a difficulty in flowing due to the higher resistance, and then the computer computes **0** bit.

3.1.2 Magnetic tunneling junction sensors (MTJs)

MTJs consist of two magnetic layers separated by an insulator one. When it is exposed to an external magnetic field, a voltage difference is induced between the two magnetic layers leading to electrons flow across the junction. The electron flow occurs through the insulator layer by the tunneling effect according to the magnetization direction in the two magnetic layers. The current flow is higher when the two magnetic layers have the same magnetization direction and vice-versa. This illustrates the change in device resistance with the applied magnetic field. In addition, MTJ also can be used as an electrical isolator, where, the usual signal isolator devices have some problems as the frequency performance limitation and the high power consumption, therefore, the MTJ based bridges

provide a proper solution for this problem.

3.1.3 Bolometric applications

The metal-semiconductor resistivity transition in manganites oxides can be used in resistive bolometers as the infrared (IR) sensors. Resistive bolometers depend on the temperature dependence of resistivity, i.e., materials should have a temperature coefficient resistance (TCR). The main idea behind the IR detectors refers to the temperature change of material due to the IR radiation absorption. IR thermal detectors sensors are considered as good detecting systems due to the small size, the lightness and the low power in comparison with the photon sensors that require cooling systems.

3.1.4 Biological applications

Biomolecular detection based magnetoresistive bio-chips plays an important role in health care area. These magnetoresistive bio-chips provide a good alternative to the fluorescent marker devices. The functionality of these GMR sensors refers to their high sensitivity to the weak magnetic fields of biological active agents as protein, drugs and cells [60]. Such sensors show good advantages as the low cost and the high signal to noise ratio in detection process.

3.1.5 Civil engineering

GMR sensors can be used for measuring the small magnetic perturbations caused by metallic bodies over earth magnetic field, as industrial machines vibrations. The small magnetic field produced by these vibrations over the earth magnetic field is converted to resistance by the GMR magnetic field gradient sensors [59], and so it can be easily detected.

3.2 Current work, motivation and aims

This work concerns with the *manganite/secondary phase* systems, which are inhomogeneous systems consisting of a ferromagnetic manganite and a secondary phase or interface materials. A remarkable feature characterizing these systems is the interaction lack between the manganite and the secondary phase materials. Due to this interaction lack, the secondary phase/interface is expected to be segregated among the manganite material grains. This fact increases the GBs resistance that interrupts carriers conduction between grains. Where, the secondary phase works as an energy barrier leading to the spin tunneling and the LFMR effect. The complete interaction lack keeps the intrinsic properties of the manganite material unchanged such as the T_c value. Thus, the T_c related phenomena as the MCE can be tuned at the same working temperature range (around T_c), in contrast with the usual partial substitution manganites systems that result in a change in the T_c, which in turn changes the MCE working temperature range.

Accordingly, the aim of this work is to study the effect of GBs resistance on the magnetoresistive and the MCE properties of $La_{0.7}Ba_{0.3}MnO_3$ compound. This is by introducing interfaces or secondary phases with this manganite compound. The study contains two main parts, the effect of interface ratio on the GBs resistance in $La_{0.7}Ba_{0.3}MnO_3/xTiO_2$ system and the GBs sensitivity to the interface size in $La_{0.7}Ba_{0.3}MnO_3/M_{0.02}$ system, where, M=Ni element powder, Ni nanowires, Ag oxide powder and Ag nanoparticles.

CH. 4 Experimental technique

This chapter describes the experimental methods and techniques used in samples preparation and measurements. The inhomogeneous systems of $La_{0.7}Ba_{0.3}MnO_3/xTiO_2$ (x=0, 0.02, 0.04, 0.06 and x=0.08) and $La_{0.7}Ba_{0.3}MnO_3/M_{0.02}$ (M is Ni nanowires, Ni element powder, Ag oxide powder and Ag nanoparticles) systems were prepared in several steps. $La_{0.7}Ba_{0.3}MnO_3$ manganite compound was prepared by the sol-gel method, TiO_2 nanotubes were prepared by the electrochemical anodization method, and Ni nanowires was prepared by the pulsed electrochemical deposition method. Ni element, Ag oxide and Ag nanoparticles are commercial raw. And the final inhomogeneous composites were prepared by the solid state reaction method. We also detail the characterization techniques and facilities used in structural examination, electrical and magnetic measurements.

4.1 Samples preparation

4.1.1 $La_{0.7}Ba_{0.3}MnO_3$ (LBMO)

The LBMO compound was prepared by the sol-gel method. This process started by dissolving stoichiometric amounts of $LaN_3O_9.6H_2O$, $Ba(OOCCH_3)_2$ and $Mn(OOCCH_3)_2.4H_2O$ salts individually in distilled water. The solutions were mixed and stirred together. Citric acid was added with 1:1 volume ratio during the stirring process that resulted in a white colloid, and then the colloid was dried at 80 °C. After drying, a brown xerogel was obtained, it was ground and dried at 600 °C for 8 hours to remove organic compounds. The resultant black powder was ground, pressed and sintered at 1200 °C for 24 hours. These procedures can be summarized in a schematic plot as in Fig. 4.1(this figure was quoted from

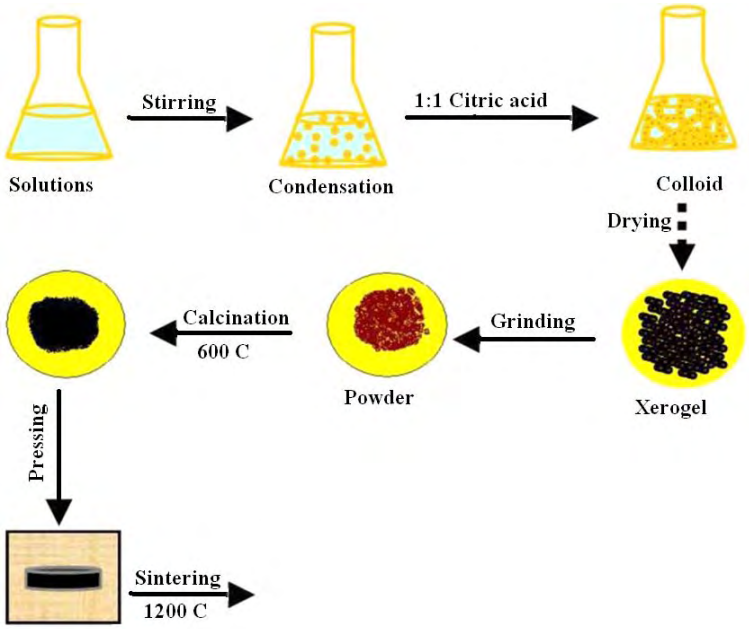

Fig. 4.1: Schematic figure for the sol-gel procedures.

D.G. Kuberkar et al [61] with some modifications).

4.1.2 TiO_2 nanotubes preparation

TiO_2 nanotubes (NTs) were prepared by the electrochemical anodization method reported in Ref. [62]. Ti foils with a high purity of 99.6 % were cleaned ultrasonically in acetone, isopropanol, ethanol and de-ionized water, respectively. The anodization process was carried out at room temperature for 24 hours in an electrochemical cell with platinum grid cathode at a constant dc voltage of 60 V. The electrolyte solution was a mixture of ammonium fluoride (0.3%), ethylene glycol and de-ionized water (1.8%). The resultant TiO_2 NTs were annealed at 400 $^{\circ}$C for 2 hours to increase their crystallinity [63].

4.1.3 Ni nanowires preparation

Ni nanowires (NWs) were prepared by the pulsed electrochemical deposition (PED) method [64]. First, nanoporous alumina membranes were prepared by the electrochemical anodization, high purity Al foils were loaded in an electrochemical cell as an anode. They were polished chemically at low temperature using perchloric acid and ethanol for 5 minutes under a constant voltage of 20V. First anodization process was performed for 24 hours with 40V in 0.3M oxalic acid as an electrolyte at 5°C with a continues stirring. A second anodization process was carried out at the same conditions. The Alumina barrier layer thinning process was performed by a progressive reduction of anodization voltage to 4.5V.

The PED process was performed using a complex electrolyte consisting of 300 g/L $NiSO_4{\cdot}6H_2O$, 45 g/L of $NiCl_2{\cdot}6H_2O$ and 45 g/L of boric acid with 4.5 pH at room temperature accompanied by successive potentiostatic and galvanostatic pulses in the millisecond range, followed by 0.7 seconds as a rest time.

4.1.4 Manganite/secondary phase preparation

LBMO/xTiO$_2$ composites (x=0, 0.02, 0.04, 0.06 and 0.08), $La_{0.7}Ba_{0.3}MnO_3/Ni_{0.02}$ and $La_{0.7}Ba_{0.3}MnO_3/Ag_{0.02}$ systems were prepared using the solid state reaction method. Stoichiometric amounts of the LBMO and the secondary phases were mixed, pelletized and sintered at 800 °C for 24 hours.

4.2 Characterization

4.2.1 Structure and surface morphology

Structural properties were examined by the x-ray diffraction (XRD) technique at room temperature using a Phillips X'Pert Pro MPD model diffractometer with CuK_α radiation (λ= 1.5406Å) in the angle range 20°-80°. Structural analysis as lattice parameters, cell volume and symmetry were obtained through the XRD patterns refinement with Rietveld analysis method [65] using the FULLPROF program. The quality of these refinements is drawn through the refinement factors as the goodness of fitting (χ^2), the crystallographic factor (R_F) and the Bragg factor (R_B). Crystallite size (P) was calculated from the XRD patterns using Laue-Scherrer equation, where $P= G \lambda/\beta \cos\theta$, G is the shape factor (0.89), and β is the full width at half maximum of the XRD peak. The microstructure and surface morphology were investigated by a scanning electron microscope (SEM) instrument JOEL JSM-6610LV model.

4.3. Measurements

4.3.1 Electrical measurements

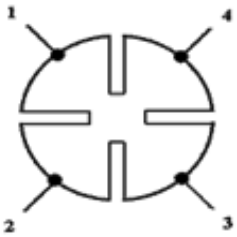

Fig. 4.2: Van der Pauw four-point technique.

Electrical resistivity (ρ) was measured in the presence and the absence of 0.5T applied magnetic field using the Van der Pauw four-point technique. The Copper tips were pasted on sample surface using silver paste in a square shape as seen in Fig. 4.2, two tips for current and the other ones for voltage. ρ was

$$\rho=(\pi d/\ln 2)\, R \qquad (4.1)$$

calculated using Eq. 4.1, where, π=3.14, ***R*** is the resistance in ohms and ***d*** is the sample thickness in cm. MR calculations were obtained from the field and zero field resistivity using Eq. 2.2.

4.3.2 Magnetic measurements

The magnetization dependence of temperature was measured at 100 Oe applied magnetic field in the temperature range of 100-400K. The isothermal magnetization curves used in the MCE calculations were measured in the temperature range of 250-395K at $\mu_0 H$=0-3T. All magnetic measurements were performed using a Versa-Lab vibrating sample magnetometer (VSM) Quantum Design instrument.

CH. 5 Transport properties of LBMO/xTiO$_2$ system

5.1 Structural properties

Fig. 5.1 shows the room temperature XRD patterns of the LBMO/xTiO$_2$ composites annealed at 800°C. The single phase of the undoped LBMO compound indicates the high homogeneity due to the complete interaction between ions. There are additional peaks at 2θ= 25.32° and 48.25° in doped composites belong to the TiO$_2$. The coexistence of TiO$_2$ and LBMO phases in doped composites suggests their interaction lack that is supported by the increase in the TiO$_2$ peaks intensity with increasing its content. The TiO$_2$-LBMO interaction lack preserves the R-3c rhombohedral structure of LBMO in all composites as it is proved by Rietveld refinement in Fig. 5.1, and the refinement factors are displayed in Table 5.1. SEM micrographs in Fig. 5.2 also support the TiO$_2$-LBMO interaction lack, where, they show the TiO$_2$ NTs destruction (during preparation process) and their precipitation as segregated grains between the boundaries and on the surfaces of LBMO grains. As the TiO$_2$-LBMO interaction lack was confirmed by the XRD and the SEM, it can be said that it is responsible for the stability in structural properties of the LBMO/xTiO$_2$ system detailed in Table 5.1 as the R-3c rhombohedral structure and the insignificant change in cell volume, lattice constants, grain size and crystallite size (P). The notable smaller value of the XRD crystallite size in comparison with the SEM grain size in all composites may suggest crystallites collectivization inside grains as a result of structural defects and/or internal stresses in the LBMO compound [66].

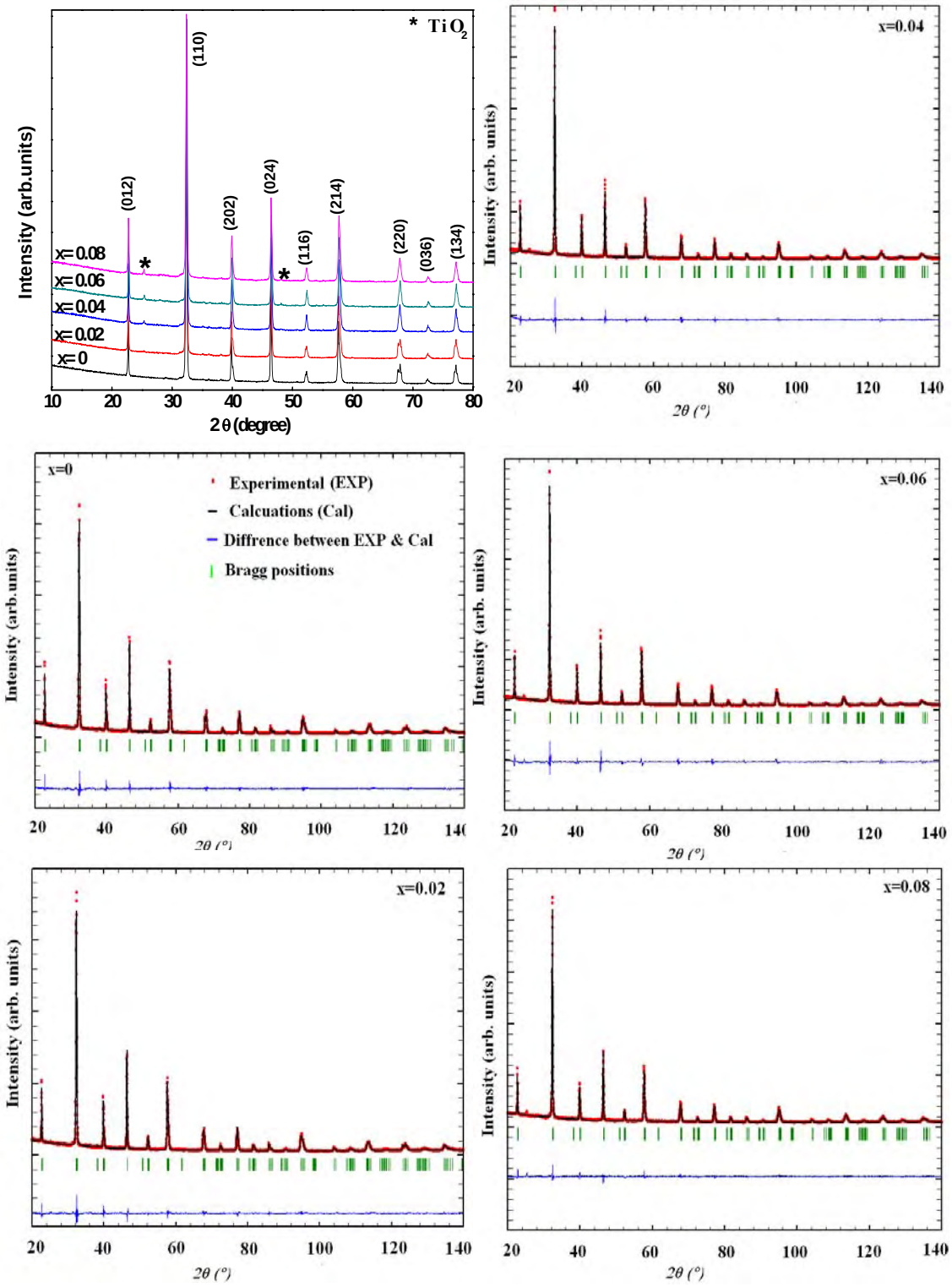

Fig. 5.1: Room temperature XRD patterns and Rietveld profiles of LBMO/xTiO$_2$ composites annealed at 800°C.

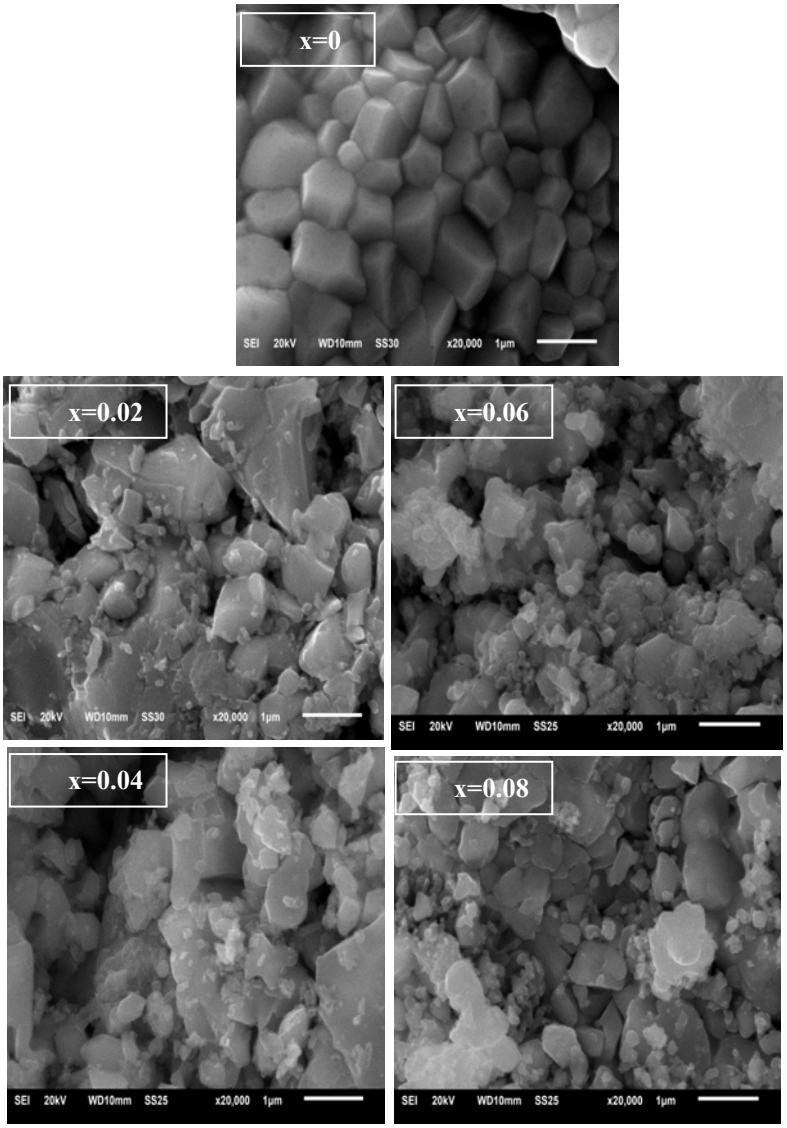

Fig. 5.2: SEM micrographs of LMBO/xTiO$_2$ composites annealed at 800 ˚C.

Table 5.1: Lattice constants, cell volume (V), SEM grain size (G), crystallite size (P), χ^2, R_F and R_B for LBMO/xTiO$_2$.

Composite	a(Å)	c(Å)	V(Å)^3	G (μm)	P(nm)	χ^2	R_F	R_B
x=0	5.543	13.4	358.86	0.748	32	3.12	5.4	5.30
x=0.02	5.540	13.4	358.52	0.659	33	2.65	3.1	3.02
x=0.04	5.534	13.5	358.25	0.659	33	3.39	4.0	3.35
x=0.06	5.534	13.5	358.20	0.684	34	5.39	4.5	4.13
x=0.08	5.536	13.4	358.22	0.635	34	2.85	4.6	3.98

5.2 Transport properties

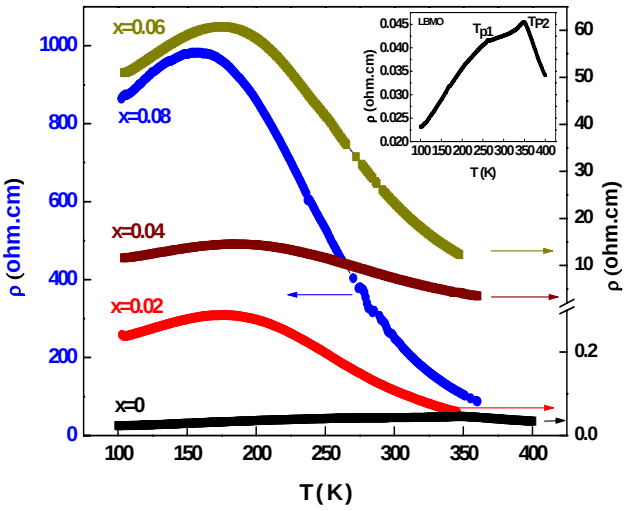

Fig. 5.3: The temperature dependence of zero field resistivity for LBMO/*x*TiO$_2$ composites and the inset shows a clear vision of the undoped LBMO compound.

Fig. 5.3 shows the temperature dependence of zero field resistivity, ρ(T), for the LBMO/*x*TiO$_2$ composites. As common in Ba and small grain size manganites [67-70], LBMO compound shows a double-peak resistivity as shown in the inset of Fig. 5.3. The smooth low temperature broad transition at T_{p1} reflects the interfacial tunneling effect at GBs [71], which arises from the magnetic ordering difference between the grain surface and core. While, the high temperature sharp transition, T_{p2}, represents the real T_{ms} that is ascribed to the DE interaction between Mn^{3+} and Mn^{4+} ions (Mn^{3+}-O-Mn^{4+}) [2], which is responsible for the metallic behavior below this temperature. The TiO_2 secondary phase increases the LBMO resistivity and decreases its T_{ms} with a discontinuity in the T_{ms} value at x=0.04 (see Table 5.2) in agreement with [15,16,72]. To explain the effect of secondary phase ratio on electrical properties, we should take into account the grain effects (size and distribution). But, the negligible change in

grain size, as clear from Table 5.1, suggests considering only the effect of grain distribution.

Conduction in granual manganites occurs through the direct contact between grains that work as conduction channels [73]. As our system contains two different kinds of grains, then, it is expected to get two different kinds of conduction channels. The main conductive channels of the LBMO grains, which are responsible for the properties, and the secondary insulating channels of the TiO_2 grains, which are distributed at the boundaries and on the surfaces of the LBMO grains. Therefore, the change in the LBMO transport properties can be understood according to the conduction interruption between the ferromagnetic grains due to the TiO_2 addition. The segregated TiO_2 weakens the LBMO grains connectivity and increases their boundaries resistance [17], which hinders conduction, increases resistivity and decreases T_{ms} [15, 74]. The increase in GBs resistance with the TiO_2 addition can be inferred from the low temperature resistivity (ρ_{100K}) increase, as seen in Fig. 5.4 that is mainly arising from GBs [14]. The T_{ms} discontinuity behavior at the x=0.04 composite agrees with the reported results in Refs. [72, 75], and refers to the possibility of TiO_2 agglomeration as interstitial grains between LBMO grains opening new conductive parallel channels [16]. It is noteworthy the large increase in the $x \geq 0.06$ composites resistivity that may be attributed to a small partial substitution of Mn^{3+} ions by Ti^{4+} ions in the LBMO lattice. This promotes the resistivity with an intrinsic component that is induced from structural distortions and ferromagnetic interactions suppression. In details, the partial substitution of Mn^{3+} by Ti^{4+}

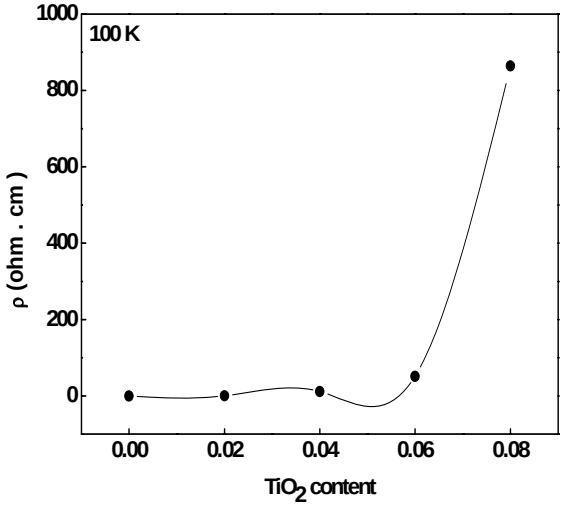

Fig. 5.4: The low temperature resistivity of LBMO/*x*TiO_2 composites at 100K.

suppresses the ferromagnetic DE interactions (Mn^{3+}-O-Mn^{4+}) due to the non-participation of Ti^{4+} ions in this mechanism (Mn^{3+}-O-Ti^{4+}). In addition, the ionic size difference between Ti^{4+} ions (0.605 Å) and Mn^{3+} ions (0.66 Å) leads to a distortion in the LBMO lattice due to the decrease in the Mn-O-Mn angles and the e_g electron mobility. Both consequences of Mn^{3+} partial substitution lead to a stronger localization of the e_g electron and a larger increase in the resistivity for x≥0.06 composites. The Mn^{3+} partial substitution suggestion at x≥0.06 composites will be supported later by the magnetic measurements.

Table 5.2: T_{ms} (K), SPH, VRH parameters and MR_{100K} (%) for LBMO/*x*TiO_2 composites.

composite	T_{ms}(K)	θ_D (K)	υ_{Ph} (Hz) x10^{13}	E_ρ(mev)	N(E_F) (eV^{-1} Cm^{-3})	R_h (Å) 300K	E_h(mev) 300 K	$MR_{100\,K}$ (%)
x=0	350	716	1.49	110.02	20.4 x 10^{20}	13.19	50.5	-11.19
x=0.02	179	560	1.16	136.96	7.14 x 10^{20}	17.15	65.7	-15.49
x=0.04	186	589	1.22	139.49	6.06 x 10^{20}	17.87	68.5	-15.54
x=0.06	174	571	1.19	142.18	4.77 x 10^{20}	18.97	72.7	-12.89
x=0.08	163	568	1.18	176.87	3.45 x 10^{20}	20.44	78.3	-9.08

5.3 Conduction mechanisms in LBMO/*x*TiO_2 system

To recognize the nature of conduction mechanism in regions above and below T_{ms}, the resistivity data were checked with well established models and experimental equations in each region. In the semiconducting region, above T_{ms}, the resistivity data were analyzed using the small polaron hopping (SPH) and the variable range hopping (VRH) models. The SPH model with $\boldsymbol{\rho/T=\rho_\alpha \exp(E_\rho/k_B T)}$ equation [76] is well applicable at $T>\theta_D/2$ temperature range as shown in Fig. 5.5, where $\boldsymbol{\rho_\alpha}$ is a constant, $\boldsymbol{E_\rho}$ is the activation energy at high temperatures, $\boldsymbol{k_B}$ is the Boltzmann constant, $\boldsymbol{\theta_D}$ is the Debye temperature and $\boldsymbol{\theta_D/2}$ is the linearity deviation temperature with this model. While, the VRH model with the $\boldsymbol{\sigma=\sigma_0 \exp(-T_0/T)^{1/4}}$ expression [76] is well fitted with the resistivity data at $T_{ms}<T<\theta_D/2$ as shown in Fig. 5.6, where $\boldsymbol{T_0=18/k_B N(E_F)a^3}$ is the Mott characteristic temperature, $\boldsymbol{N(E_F)}$ is the density of states near the Fermi level $\boldsymbol{(E_F)}$ and $\boldsymbol{a}$ is the localization length that equals 0.45 nm as reported in Ref. [77]. According to the VRH model at $T_{ms}<T<\theta_D/2$ temperature range, carriers hop from site to site with hopping energy $\boldsymbol{E_h}$ passing a distance $\boldsymbol{R_h}$, which are temperature dependent parameters and can be determined from the $\boldsymbol{E_h(T)=1/4k_B T^{3/4} T_0^{1/4}}$ and $\boldsymbol{R_h(T)=3/8a(T_0/T)^{1/4}}$ equations [78]. The continuous increase in the GBs thickness and resistance with the TiO_2 addition increases carriers localization. This increases the required distance for hopping $\boldsymbol{(R_h)}$, which decreases transport across grains leading to a decrease in the $\boldsymbol{N(E_F)}$ (see Table 5.2). Then, for an easy transport between grains, carriers need more energy to overcome barriers and localization, this explains the monotonic increase of $\boldsymbol{E_\rho}$ and $\boldsymbol{E_h}$ with increasing TiO_2 content, as seen in

Table 5.2, which is in agreement with the reported results in Ref. [11]. The promotion in carriers localization with TiO_2 addition increases the SPH temperature range of the LBMO compound, this can be inferred by the decrease in the $\boldsymbol{\theta_D}$ and the phonon frequency (υ_{Ph}) values as seen in Table 5.2 (υ_{Ph} has been determined from $\boldsymbol{h\upsilon_{Ph}=k_B\theta_D}$ relation, **h** is the Planck constant).

On the other hand, the resistivity data in the metallic region, below T_{ms}, were examined by the empirical equations Eq. 5.1, Eq. 5.2, Eq. 5.3 and Eq. 5.4. Where, $\boldsymbol{\rho_0}$ is the resistivity component arising from the GBs and the temperature independent parameters, $\boldsymbol{\rho_2 T^2}$ term arises from the electron-electron interactions, $\boldsymbol{\rho_{2.5} T^{2.5}}$ term arises from the electron-magnon interactions, $\boldsymbol{\rho_{4.5} T^{4.5}}$ term arises from the spin wave scattering process and $\boldsymbol{\rho_5 T^5}$ arises from the electron-phonon interactions. The LBMO compound resistivity data satisfies Eq. 5.4, as seen in Fig. 5.7. This reveals the roles of GBs, spin wave, electron-electron and electron-phonon interactions in conduction mechanism in this compound. But in doped composites, the resistivity data are much better fitted with Eq. 5.3 (see Fig. 5.7). This excludes the electron-phonon interactions component in doped composites because of the increase in scattering process due to the TiO_2 presence as scattering centers. Generally, Table 5.3 confirms that the GBs component has the most effective role in the resistivity change with TiO_2 addition, supporting the experimental results.

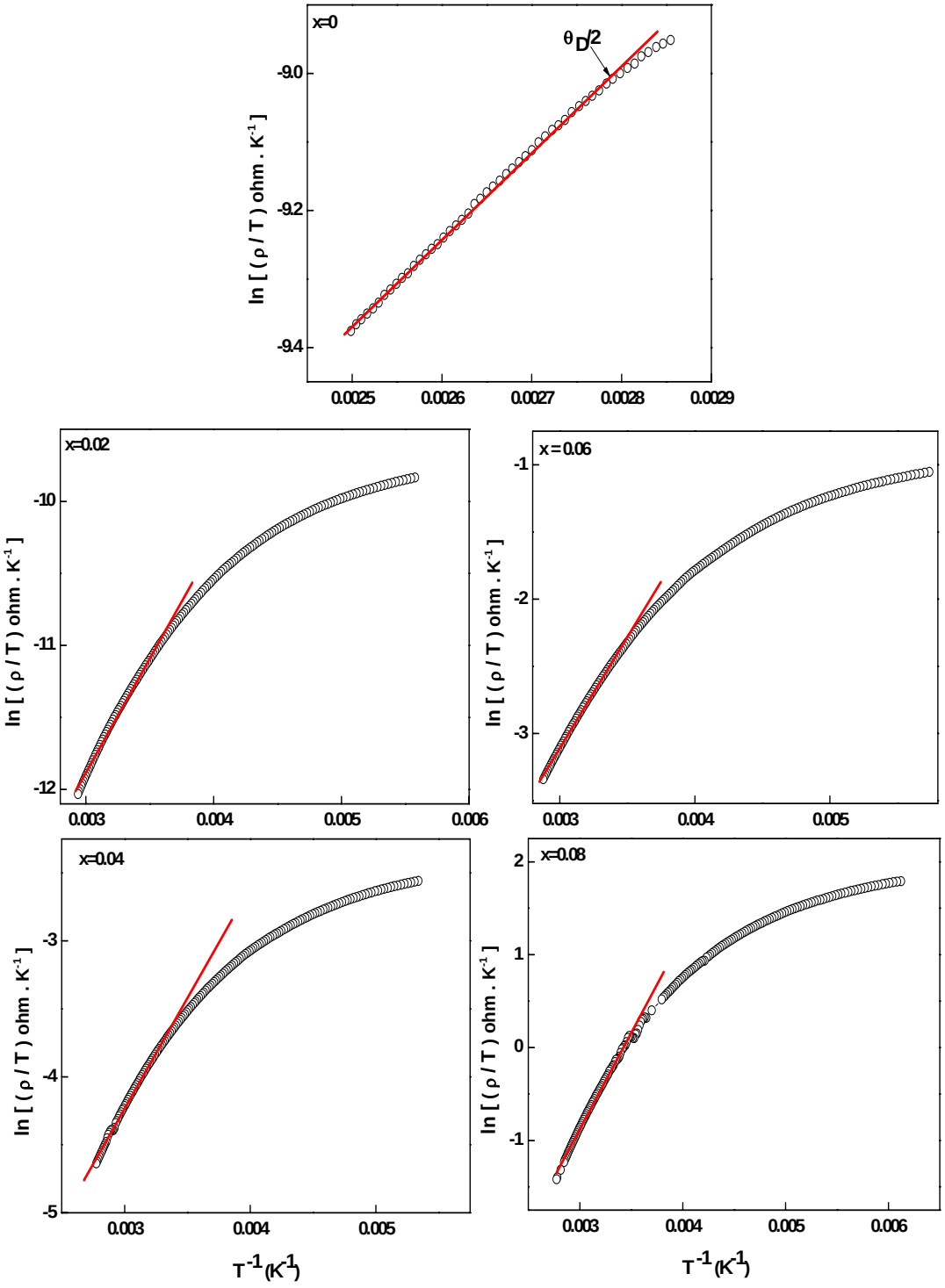

Fig. 5.5: SPH model for the LBMO/xTiO_2 system, the red solid line represents the best fitted points with this model.

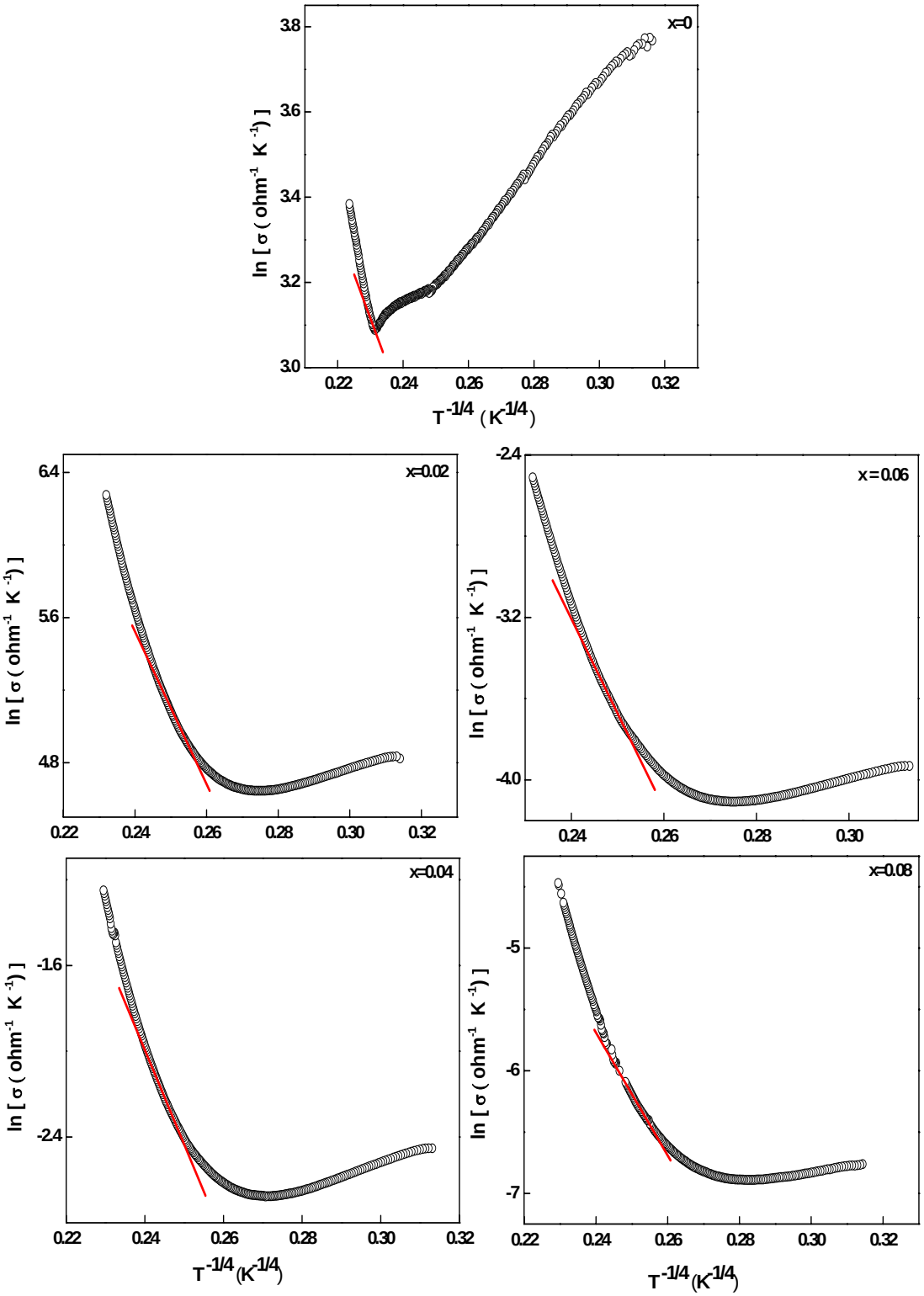

Fig. 5.6: VRH model for LBMO/xTiO$_2$ system, the red solid line represents the best fitted points with this model.

$$\rho=\rho_0+\rho_2T^2 \quad (5.1)$$

$$\rho= \rho_0+\rho_{2.5}T^{2.5} \quad (5.2)$$

$$\rho=\rho_0+\rho_2T^2+ \rho_{4.5}T^{4.5} \quad (5.3)$$

$$\rho=\rho_0+\rho_2T^2+\rho_{4.5}T^{4.5}+\rho_5T^5 \quad (5.4)$$

Table 5.3: The best-fitting parameters in the ferromagnetic region obtained from the experimental Eq. 5.3 and Eq. 5.4 for the LBMO/*x*TiO_2 system.

composite	ρ_0 (Ω.cm)	ρ_2 (Ω.cm)	$\rho_{4.5}$ (Ω.cm)	ρ_5 (Ω.cm)
x=0	0.0145	$7.53x10^{-7}$	$-1.11x10^{-12}$	$4.7x10^{-14}$
x=0.02	0.166	2.26×10^{-7}	-2.41×10^{-13}	-
x=0.04	8.32	3.19×10^{-4}	-2.94 x 10-^{10}	-
x=0.06	37.37	1.35×10^{-3}	-1.45×10^{-9}	-
x=0.08	638.97	2.48×10^{-2}	-3.53×10^{-8}	-

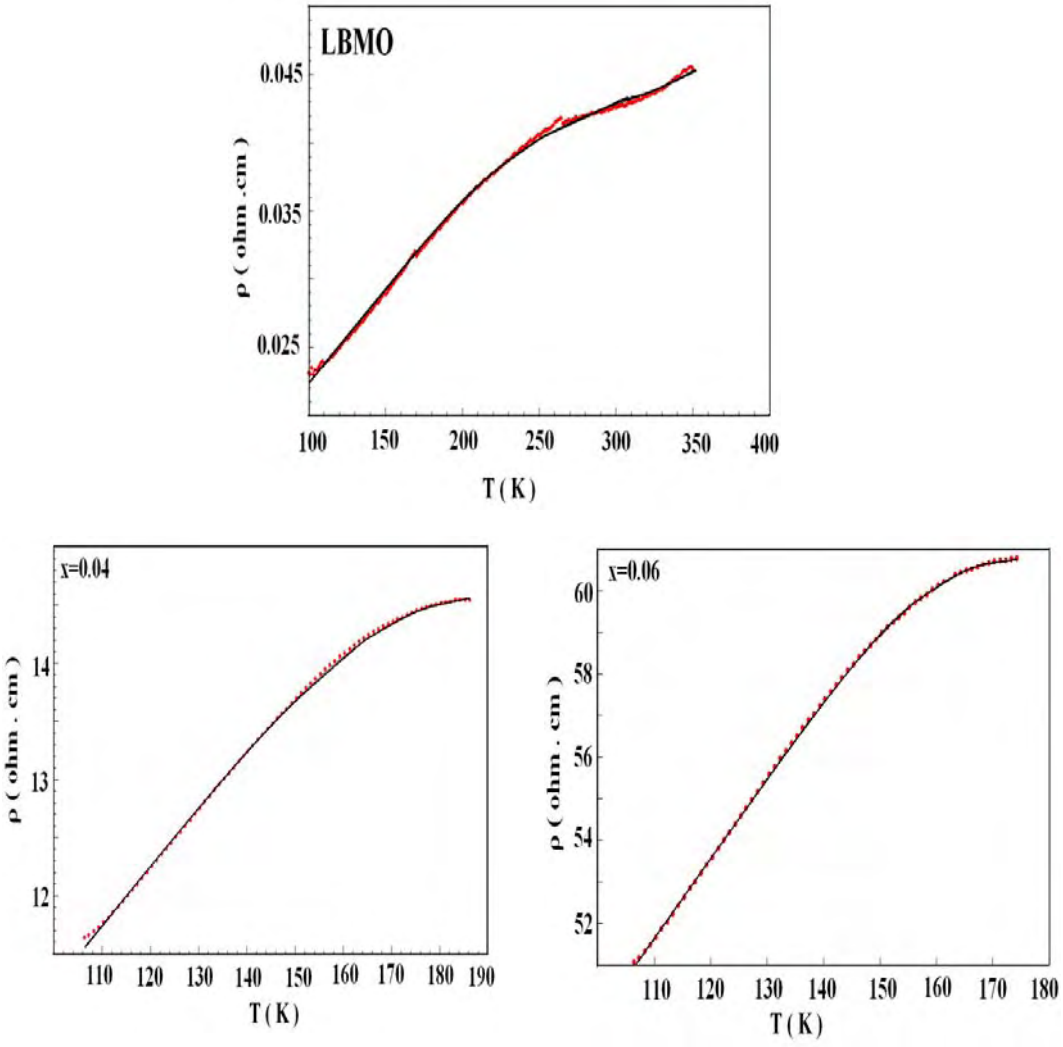

Fig. 5.7: Resistivity data fitting below T_{ms} for the LBMO compound with Eq. 5.4, and x=0.04 & x=0.06 composites with Eq. 5.3, the red points are the experimental data and the black solid line is the fitting equation.

5.4 Magnetoresistive properties

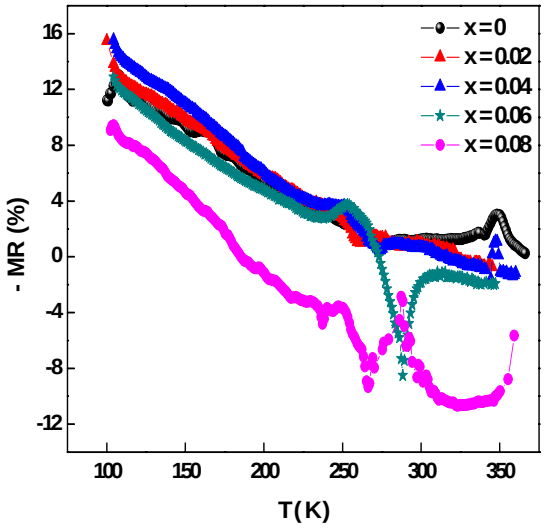

Fig. 5.8: Temperature dependence of magnetoresistance for the LBMO/*x*TiO_2 system.

The temperature dependence of MR is shown in Fig. 5.8 at 0.5T applied magnetic field. The composites with x≤0.04 show a negative MR all over the whole temperature range. Whereas, the x≥0.06 composites show a crossover from negative to positive MR in a plunge at relatively high temperatures that is quite familiar in some manganites [15, 79]. The high values of negative MR are observed at low temperatures decreasing with temperature elevation and passing through a peak, in a similar behavior with reported results in Ref. [9]. The LBMO compound shows a MR peak at T_{ms} temperature with a maximum value of -3%, which is shifted towards lower temperatures and increases in value to -3.3, -3.5 and -3.7% with TiO_2 addition for x= 0.02, 0.04 and 0.06 ratios, respectively. Table 5.2 also shows the low temperature MR value (at 100K) with TiO_2 doping as an evidence of the general MR enhancement. The LFMR enhancement with doping level at x≤ 0.06 refers to the increase in GBs resistance that leads to

carriers scattering and spin- polarized tunneling across GBs [10,18]. But, with further amounts of TiO_2 (x=0.08), the GBs thickness may exceed the spin memory length [80], which decreases the electron tunneling effect and hence the LFMR effect [81].

The negative or positive sign of MR is mainly related to majority and minority spin carriers, respectively, near the $\boldsymbol{E_F}$ [82]. This concept suggests a spin carriers change at x≥0.06 composites. In details, due to the complete TiO_2-LBMO interaction lack at x≤0.04 composites, Ba^{2+} electrons are kept in the $\boldsymbol{e_g}$ band of the LBMO representing major spin carriers near $\boldsymbol{E_F}$ that exhibits a negative MR. While at x≥0.06 composites, the small partial substitution of Mn^{3+} by Ti^{4+} may lead to electronic leakage from Ti^{4+} into LBMO resulting in a change in carriers spin and hence the change in MR sign. In the later scenario, at low temperatures for x≥0.06 composites, Ti^{4+} electrons occupy the $\boldsymbol{e_g}$ band ($e_g^{\downarrow}$ or $e_g^{\uparrow}$ state) of LBMO preserving the majority spin carriers leading to a negative MR [82]. With temperature elevation, the edge of the $t_{2g}^{\downarrow}$ band becomes closer to the $\boldsymbol{E_F}$ than the $\boldsymbol{e_g}$ band. Therefore, it is easier for Ti^{4+} electrons to occupy the $t_{2g}^{\downarrow}$ band rather than the $\boldsymbol{e_g}$ band. In this case, the $t_{2g}^{\downarrow}$ spin orientation becomes in an antiparallel alignment with the system leading to the minority spin carriers near $\boldsymbol{E_F}$ that results in the positive MR at high temperatures [82].

CH.6 Magnetic and magnetocaloric properties of LBMO/xTiO$_2$ system

6.1 Magnetic properties

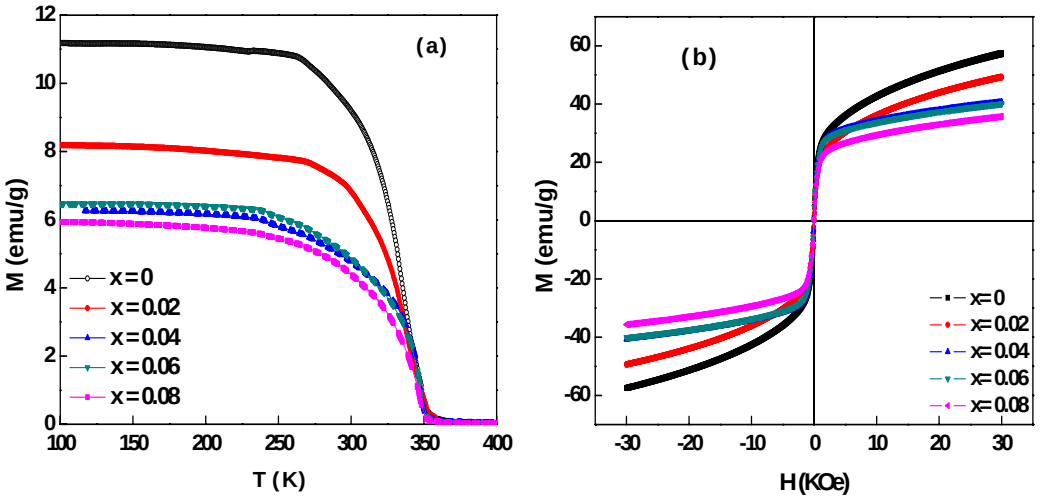

Fig. 6.1: (a) Temperature dependence of magnetization at H=100 Oe, and (b) Hysteresis loop at 300 K for LBMO/xTiO$_2$ system annealed at 800 °C.

Fig. 6.1a shows the temperature dependence of dc magnetization, M(T), at 100 Oe applied magnetic field, where, the ferromagnetic-paramagnetic (FM-PM) transition at T_c characterizes all composites. The sharp drop in magnetic transition of the LBMO compound ensures its high homogeneity as observed in the XRD pattern. While, the relative broadness in the magnetic transition of doped composites refers to the TiO$_2$ presence as an impurity phase [83]. The TiO$_2$ doping decreases system magnetization due to the decrease in the LBMO ferromagnetic ratio. The magnetic transition temperature, T_c, was determined from the minimum of the dM/dT curves and it is listed in Table 6.1. This table shows the T_c independence of TiO$_2$ content, where it shows a constant value of 348K for all composites with insignificant change at x=0.08 composite, in agreement with Refs. [84,85]. The constant value of T_c with TiO$_2$ addition refers to its intrinsic

nature that depends on the ferromagnetic ordering inside the grain [86]. In other words, TiO_2 addition affects only the GBs without any change in the internal grain ferromagnetism due to the TiO_2-LBMO interaction lack, which preserves the T_c value unchanged. Similarly, the insignificant change in the T_c value at x=0.08 composite can be easily understood as based on the change in grain ferromagnetism. Where, the small partial substitution process of Mn^{3+} by Ti^{4+} weakens the LBMO grain ferromagnetism due to the antiferromagnetic Mn^{3+}-O-Ti^{4+} bonds formation that decreases the T_c value. In contrast with T_c, T_{ms} is an extrinsic parameter that can be easily affected by the GBs. Therefore, the T_{ms} occurrence far below the T_c value is reasonable [86, 87] and points out the GBs role as the main source of resistivity change rather than the grain itself [88]. Fig. 6.1b shows the hysteresis loops at 300K, where, a narrow hysteresis characterizes all composites. This figure shows the rapid increase in magnetization at low magnetic fields and the saturation tendency at high magnetic fields. The saturation magnetization decreases with increasing the TiO_2 content as a result of the ferromagnetism dilution and the non magnetic nature of the additive oxide.

Fig. 6.2 shows the isothermal magnetization curves as a function of the applied magnetic field. Below T_c, the magnetization increases sharply with low magnetic fields and saturates at high magnetic fields corresponding to the ferromagnetic behavior. While above T_c, the magnetization increases linearly with the applied magnetic field indicating the paramagnetic behavior. Using the isothermal magnetization curves, the FM-PM transition type can be identified through the respective Arrott plots, which displays M^2 as a function of $\mu_0 H/M$

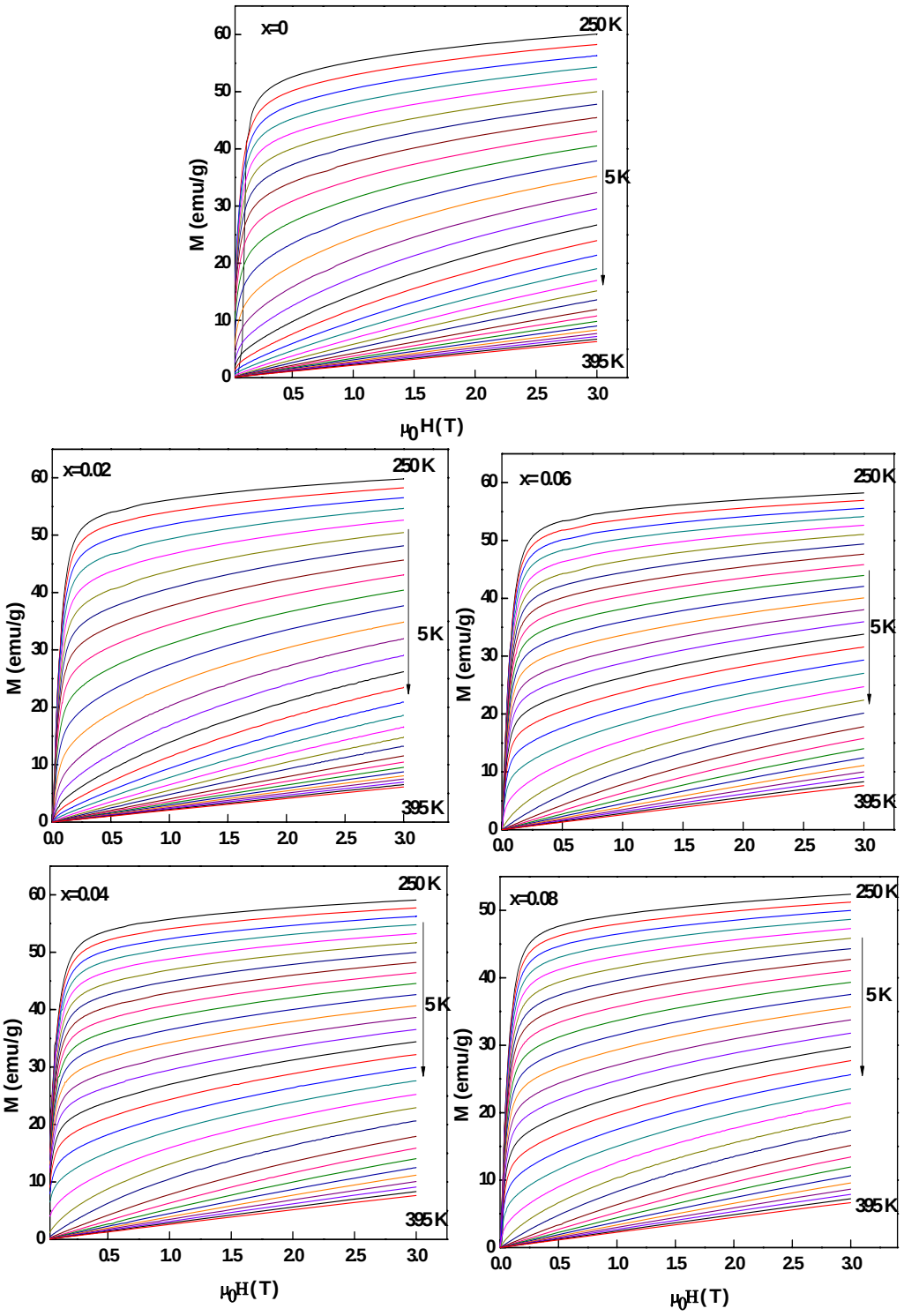

Fig. 6.2: Isothermal magnetization curves at different temperatures of LBMO/xTiO$_2$ system.

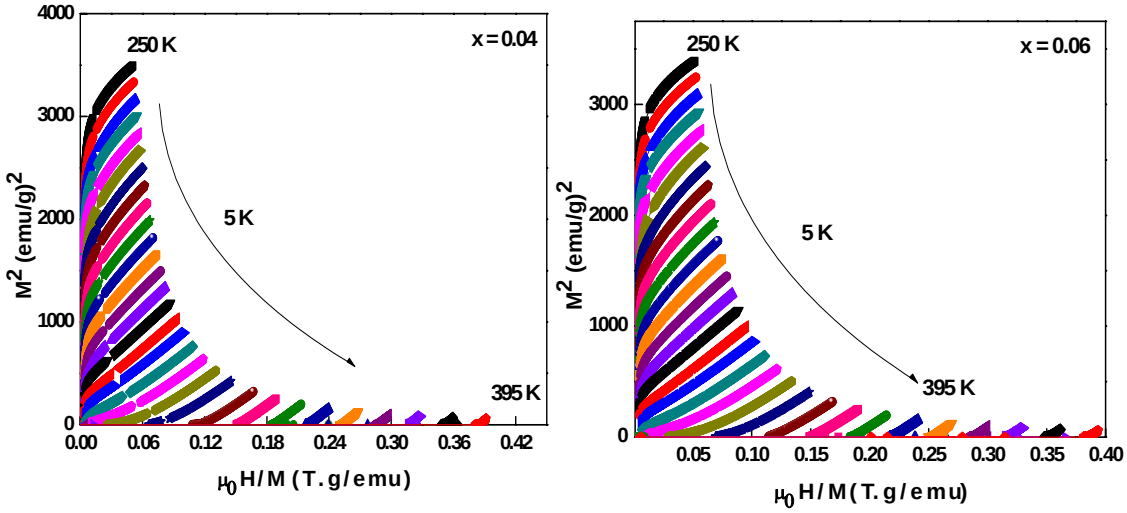

Fig. 6.3: Arrott plots for x=0.04 and x=0.06 composites.

at different temperatures [89] as shown in Fig. 6.3 for x=0.04 and x=0.06 composites as selected composite samples. The magnetic transition type depends on the Arrott plots slope around T_c [90], where, the positive slope reveals a second order magnetic transition; otherwise it indicates a first order type [90]. According to these criteria, the LBMO/xTiO$_2$ composites exhibit a second order magnetic transition because of the positive slope of Arrott plots around T_c.

6.2 Magnetocaloric effect (MCE)

The MCE based on magnetic entropy change, ΔS, was determined from the isothermal magnetization curves using Maxwell's relation in Eq. 2.6. The thermal variation of ΔS at different applied magnetic field changes is shown in Fig. 6.4. ΔS shows negative values with a maximum around T_c (ΔS_{max}) that increases in amplitude with the applied magnetic field. TiO$_2$ addition decreases ΔS_{max} value of the LBMO without significant change in its working temperature range as seen in Fig. 6.5a. This decrease in ΔS_{max} value with TiO$_2$ content refers

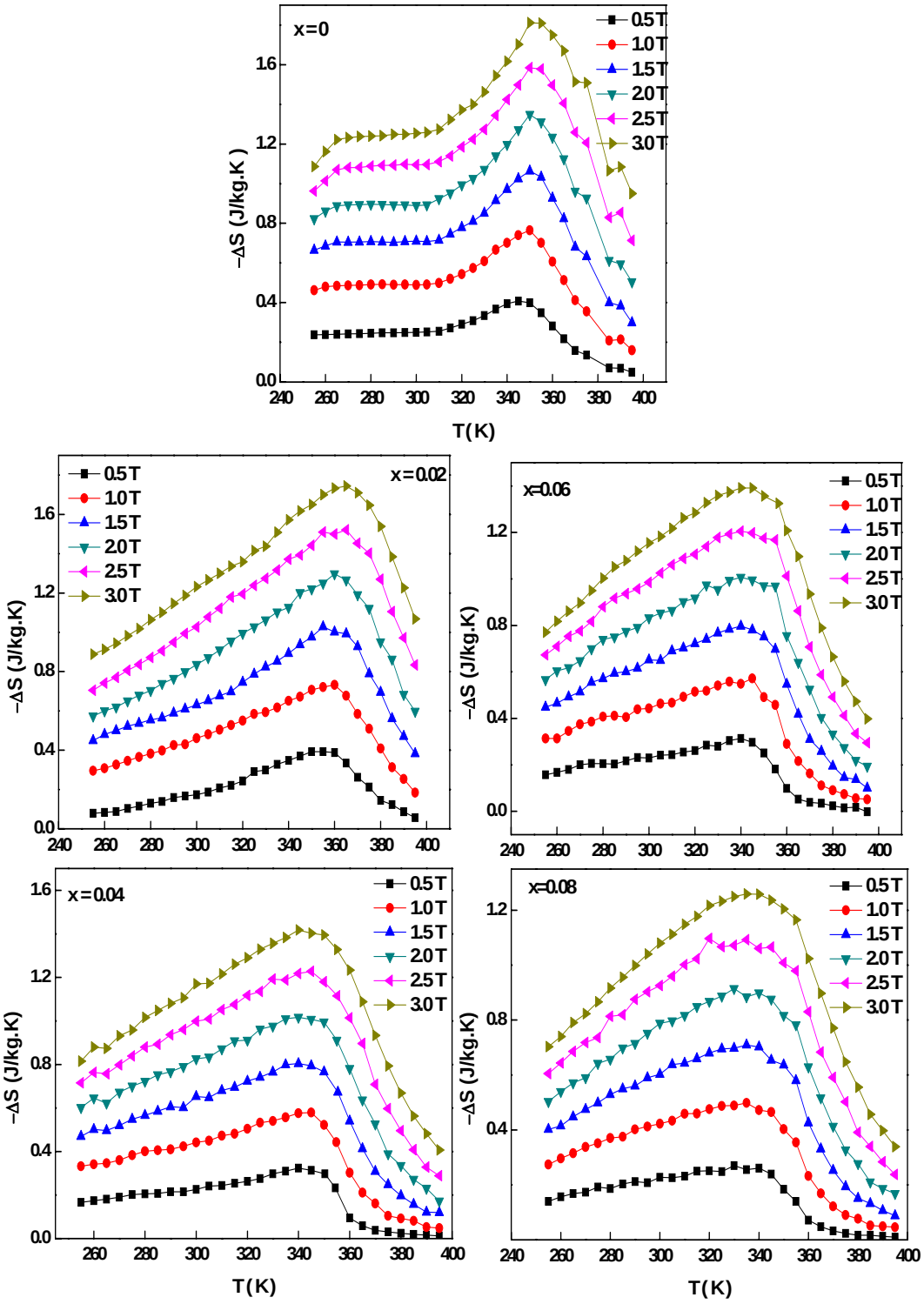

Fig. 6.4: Thermal variation of ΔS at different magnetic field changes for LBMO/*x*TiO$_2$ composites.

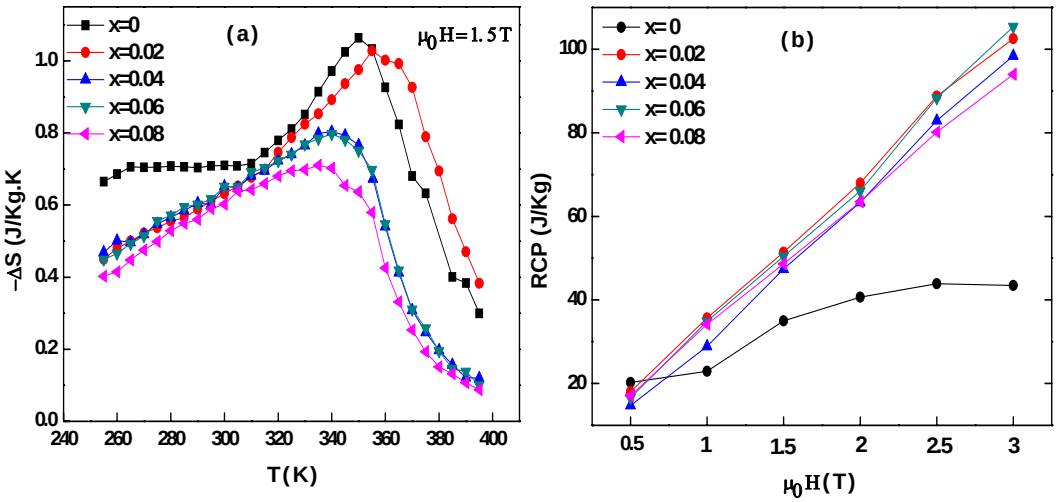

Fig. 6.5: (a) Temperature dependence of ΔS at 1.5T magnetic field change with doping level and (b) the RCP vs. magnetic field change.

Table 6.1: T_c (K), δT_{FWHM} (K) and RCP (J/kg) of LBMO/xTiO_2 system in comparison with the magnetocaloric properties of other manganites.

Composite	μ_0H (T)	T_c (K)	δT_{FWHM} (K)	RCP (J/kg)	Ref
$La_{0.7}Ba_{0.3}MO_3$	1.5	348	32.91	35	This work
$La_{0.7}Ba_{0.3}MO_3/(TiO_2)_{0.02}$	1.5	348	50.02	51	This work
$La_{0.7}Ba_{0.3}MO_3/(TiO_2)_{0.04}$	1.5	348	58.97	47	This work
$La_{0.7}Ba_{0.3}MO_3/(TiO_2)_{0.06}$	1.5	348	63.26	50	This work
$La_{0.7}Ba_{0.3}MO_3/(TiO_2)_{0.08}$	1.5	346	68.49	49	This work
$La_{0.7}Sr_{0.3}MnO_3$	2	369	-	29	[27]
$La_{0.7}Pb_{0.3}MnO_3$	5	352	-	48	[91]
$La_{0.67}Sr_{0.33}MnO_3$	5	370	-	252	[92]
$La_{0.7}Sr_{0.3}Mn_{0.95}Fe_{0.05}O_3$	5	343	-	215	[93]

to the decrease in the LBMO ferromagnetic ratio, while, the negligible change in the temperature position refers to the T_c constant value due to their correlation. Table 6.1 shows the notable enhancement in the RCP values of the LBMO compound with increasing TiO_2 content, and Fig. 6.5b shows the proportional relation of the RCP with the applied magnetic field changes. These results reveal that the RCP enhancement in a *manganite/insulator* system is more likely arising from the change in δT_{FWHM} rather than from ΔS_{max} (see Table 6.1). Table 6.1 also presents a comparison among our system results and other ones reported in works devoted to magnetocaloric properties in different manganites. This comparison suggests our system potentiality in high temperature-low field magnetic refrigeration applications. From MCE measurements, we can draw an interesting feature of the *manganite/insulator* system related to the RCP variation at the same temperature range. In more details, ΔS shows a maximum value around T_c and any attempt to enhance this value by the partial substitution with other element leads to a change in the T_c value, which in turn changes the RCP working temperature range. According to our results, this rarely happens in *manganite/insulator* system because of the interaction lack between the insulator and the manganite materials that preserves the T_c value of the manganite system without any change, and also keeps the RCP working temperature range unchanged. In this way, if we choose a manganite material with an optimum T_c, especially in the room temperature range, then we can get enhanced MCE properties in the same temperature range.

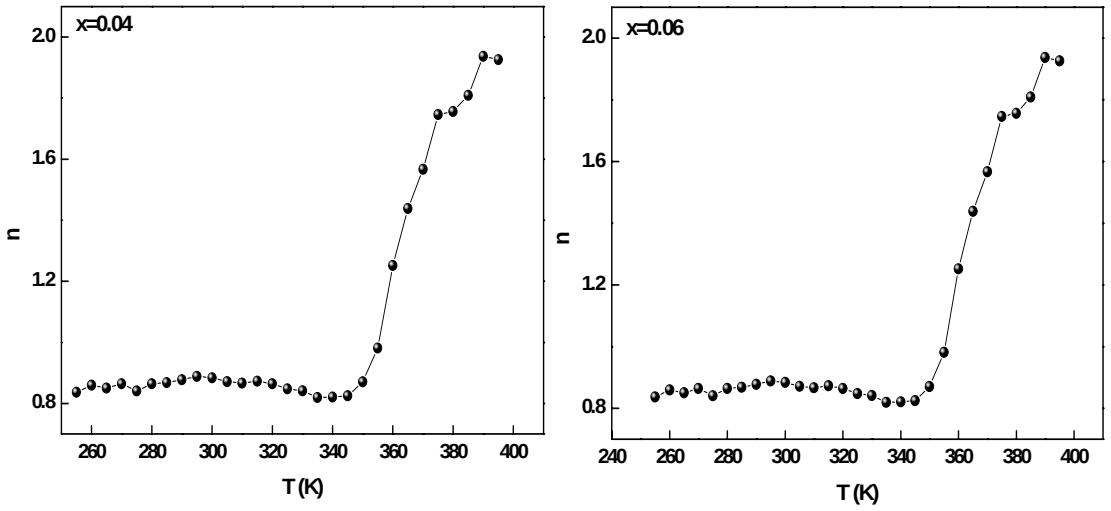

Fig. 6.6: The temperature dependence of the exponent power n for x=0.04 and x=0.06 composites.

As the second order transition has been proved for the LBMO/xTiO$_2$ system, thus, the magnetic field dependence of ΔS should obey $\mathbf{\Delta S=a(\mu_0 H)^n}$ relation [94], where ***a*** is a constant and ***n*** is an exponent power depending on the sample magnetic state. According to the mean field theory, the ***n*** value at T_c, [$n(T_c)$], is 0.67 [94], however, $n(T_c)$ for some manganites does not match well this value [95]. The temperature dependence of the exponent power ***n*** is displayed in Fig. 6.6 for x=0.04 and x=0.06 composites as selected samples. These figures show a rough decrease in the ***n*** value at low temperatures passing through a minimum near the T_c, then increases sharply. The ***n*** value for all composites was found to be 0.87, which is very close to these reported in manganites and rare earth metal materials [96, 97], however, it deviates a little from the mean field theory value. This deviation may refer to a local inhomogeneity or superparamagnetic clusters near T_c [98, 99].

$$G(M, T)= G_0+ \frac{a(T)}{2} M^2 + \frac{b(T)}{4} M^4+\frac{C(T)}{6} M^6+\ldots\ldots\ldots- \mu_0 H \quad (5.1)$$

$$\mu_0 H = a(T)\, M+ b(T)\, M^3+ c(T)\, M^5 \quad (5.2)$$

$$-S\,(T, \mu_0 H) = \left(\frac{\delta G}{\delta T}\right) \mu_0 H = \frac{a(T)}{2}\frac{\delta M^2}{\delta T} + \frac{b(T)}{4}\frac{\delta M^4}{\delta T} + \frac{c(T)}{6}\frac{\delta M^6}{\delta T} \quad (5.3)$$

To identify the origin of different contributions to the MCE in the LBMO/xTiO$_2$ system, we have made a theoretical modeling based on *Landau theory* [100] for the MCE experimental results that takes into account elastic, magnetoelastic and magnetoelectronic coupling effects. According to this theory, the magnetic energy (***M***) can be involved in *Gibb's* free energy as in Eq. 5.1, where **a**, **b** and **c** are *Landau* thermodynamic temperature dependent coefficients that have been determined from Eq. 5.2 (the equilibrium state of Eq. 5.1 ($\delta G/\delta T=0$)). Basically, **a** and ***b*** coefficients play important role in ΔS of manganites [95], because, they can provide information about some related magnetic properties. For example, ***a(T)*** coefficient in Fig. 6.7 is positive in agreement with Ref. [101] and shows a minimum around 330K, which is far somewhat from the T_c experimental value (348K). Also, the positive value of ***b*** at T_c, ***b*(T_c)**, indicates the second order transition [100, 102], as seen in Fig. 6.7, confirming the results obtained from Arrott plots. ΔS calculations based on *Landau* theory are obtained using Eq. 5.3 resulting from *Gibb's* energy differentiation with respect to the temperature. Fig. 6.8 shows these calculations in comparison with the experimental results derived from Maxwell equation. The observed difference between them indicates that the magnetocaloric properties arise only due to the magnetic entropy change, in agreement with [103], and

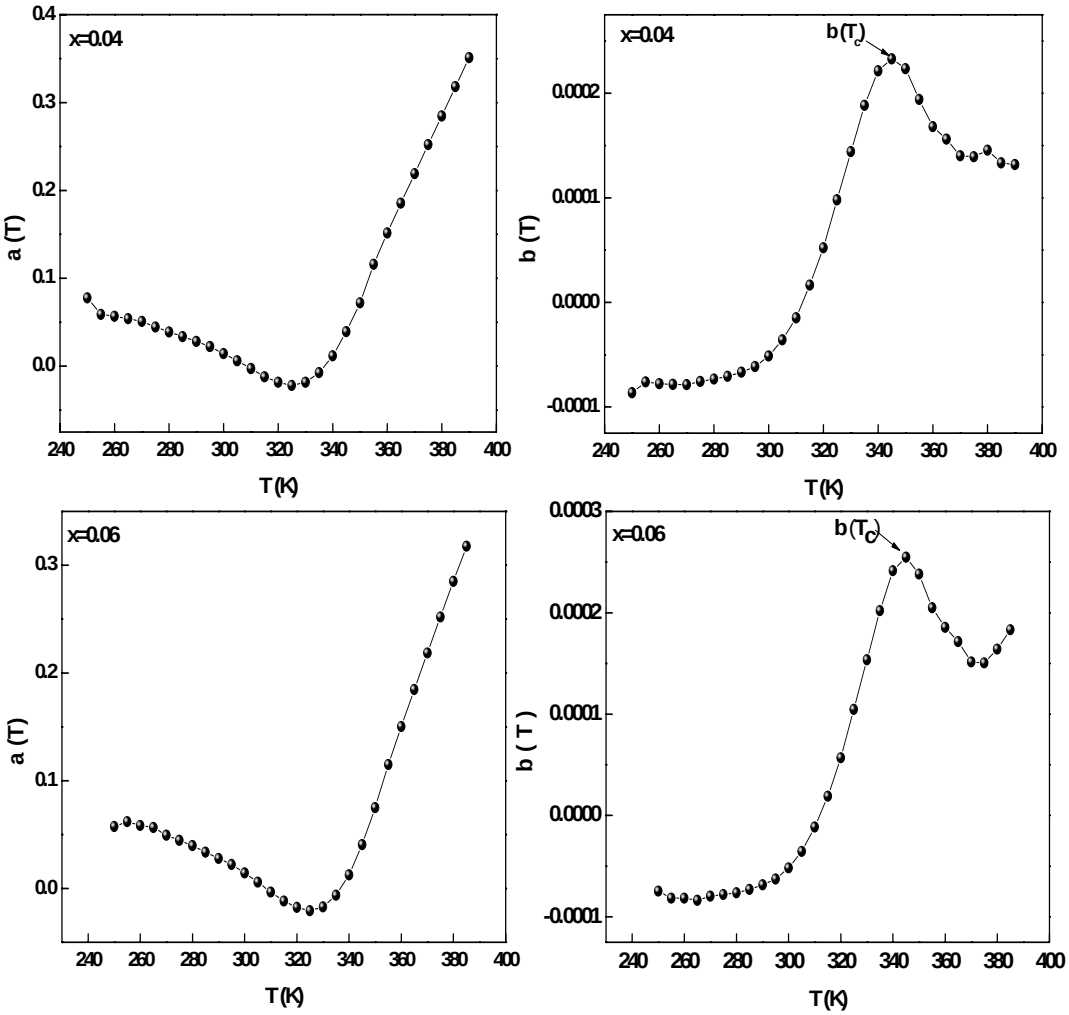

Fig. 6.7: Thermal variation of Landau coefficients (a and b) for x=0.04 and x=0.06 composites.

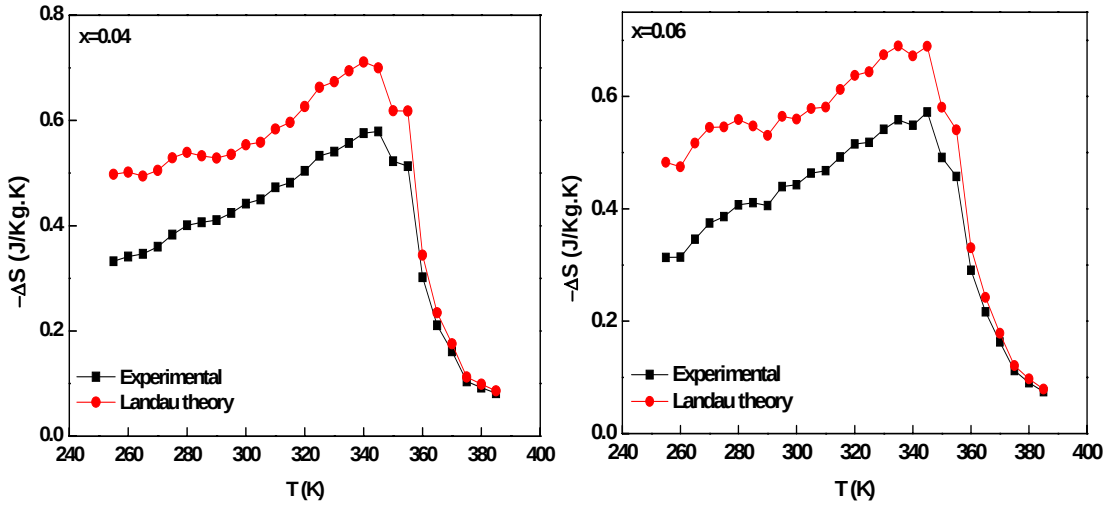

Fig. 6.8: Comparison between the experimental values and Landau based calculation of ΔS at a magnetic field change of 1T, for x=0.04 and x=0.06 composites.

suggests the non participation of elastic, magnetoelastic and magnetoelectronic coupling involved in *Landau* theory. And this may be the reason for the difference between the experimental T_c value and the deduced one from **a(T)** coefficient.

CH. 7 Influence of annealing temperature on magnetic and magnetocaloric properties

As it has been stated previously, the interaction lack between manganite and insulator materials is the main feature behind the *manganite/secondary phase* system properties. The secondary phase distribution at GBs and on the surface of the manganite grains is suggested to be the key role of these systems properties. It changes the boundaries resistance that is responsible for the magnetization change and the spin tunneling between grains. The secondary phase distribution may be affected by annealing treatment modifying the magnetic properties and their related phenomena. In this chapter, we study magnetic and magnetocaloric properties of LBMO/xTiO$_2$ composites annealed at 600°C for 24 hours and compare these results with those arising from samples annealed at 800°C, x=0.04 and x=0.06 composites have been the selected samples for this study.

7.1 Structural properties

XRD patterns of the LBMO/xTiO$_2$ composites annealed at 600°C and 800°C are shown in Fig. 7.1. The patterns of doped composites show the coexistence of TiO$_2$ peak with LBMO phase for both annealing temperatures revealing the interaction lack preservation with changing the annealing temperature. The TiO$_2$-LBMO interaction lack preservation can be inferred by the quite similar TiO$_2$ peak intensity for both annealing temperatures. This explains the stability in structural properties, for both annealing temperatures, as the R-3c rhombohedral structure, cell volume and crystallite size (see Table 7.1). Rietveld refinements for x=0.06 composite annealed at 600 and at 800°C are also displayed in Fig. 7.1 as an example. SEM micrographs in Fig. 7.2 show the TiO$_2$

Table 7.1: Symmetry, cell volume (V), SEM grain size (G) and XRD crystallite size (P) of LBMO/*x*TiO_2 composites annealed at 600 °C and 800 °C.

composite	condition	symmetry	V $(Å)^3$	G (μm)	P (nm)
x=0	as-prepared	Rhombohedral	358.86	0.74	32
x=0.04	600 °C	Rhombohedral	358.17	0.63	34
	800 °C	Rhombohedral	358.25	0.65	33
x=0.06	600 °C	Rhombohedral	358.23	0.67	33
	800 °C	Rhombohedral	358.20	0.68	34

precipitation at the boundaries and on the surfaces of LBMO grains in samples annealed at both temperatures, revealing the insignificant change in the average SEM grain size and the crystallite size of the LBMO compound after both annealing treatments, as seen in Table 7.1, which also supports the idea of TiO_2-LBMO interaction lack preservation. Moreover, the SEM micrographs show an important feature, they show a different distribution of TiO_2 in both annealing temperatures meaning that the secondary phase is affected by the annealing temperature. TiO_2 grains are less randomized and well agglomerated in composites annealed at the higher temperature of 800°C compared with those annealed at 600°C.

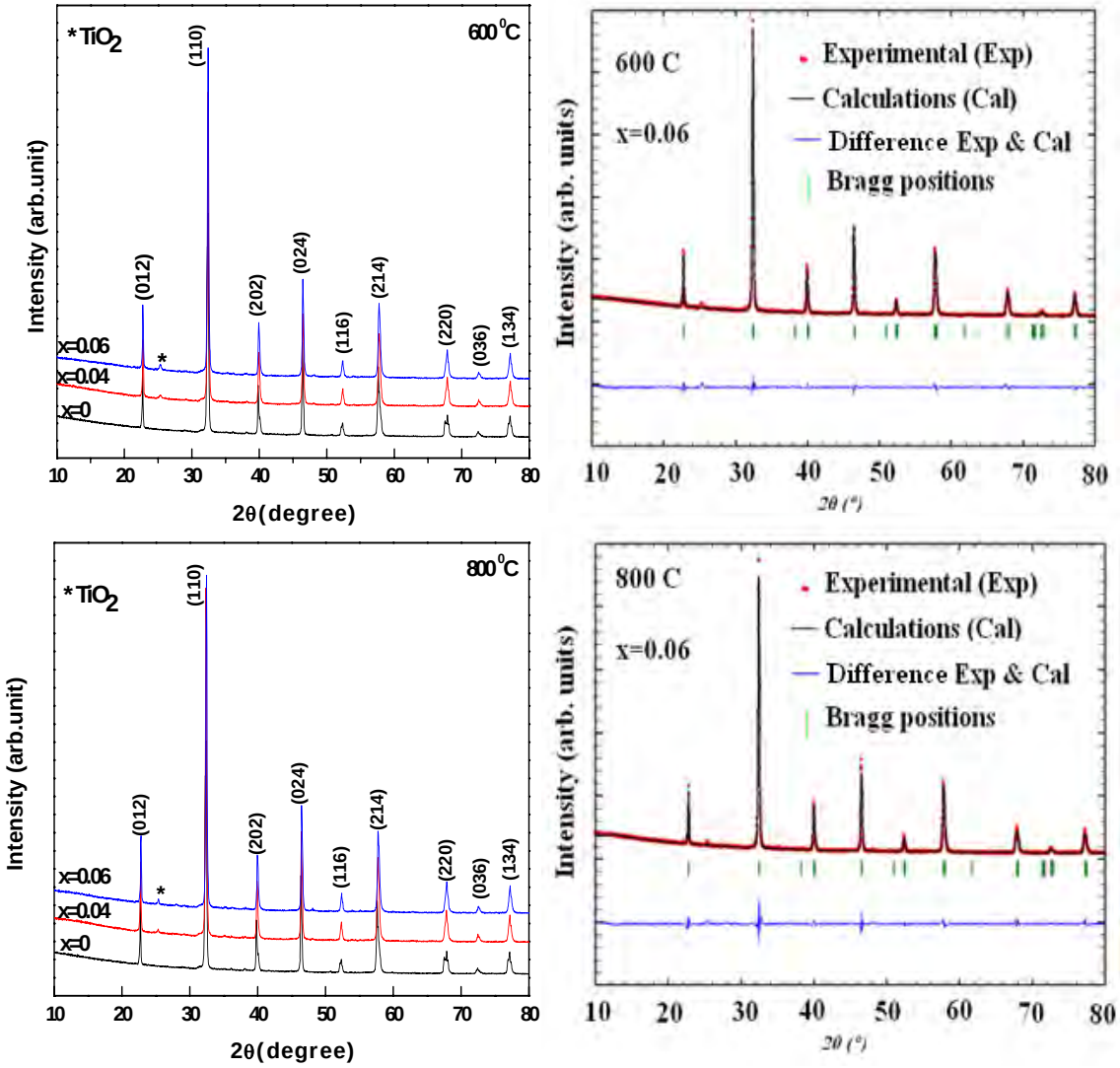

Fig. 7.1: XRD patterns of LBMO/xTiO$_2$ composites and Rietveld refinement profile for x=0.06 composite annealed at 600 and 800 °C.

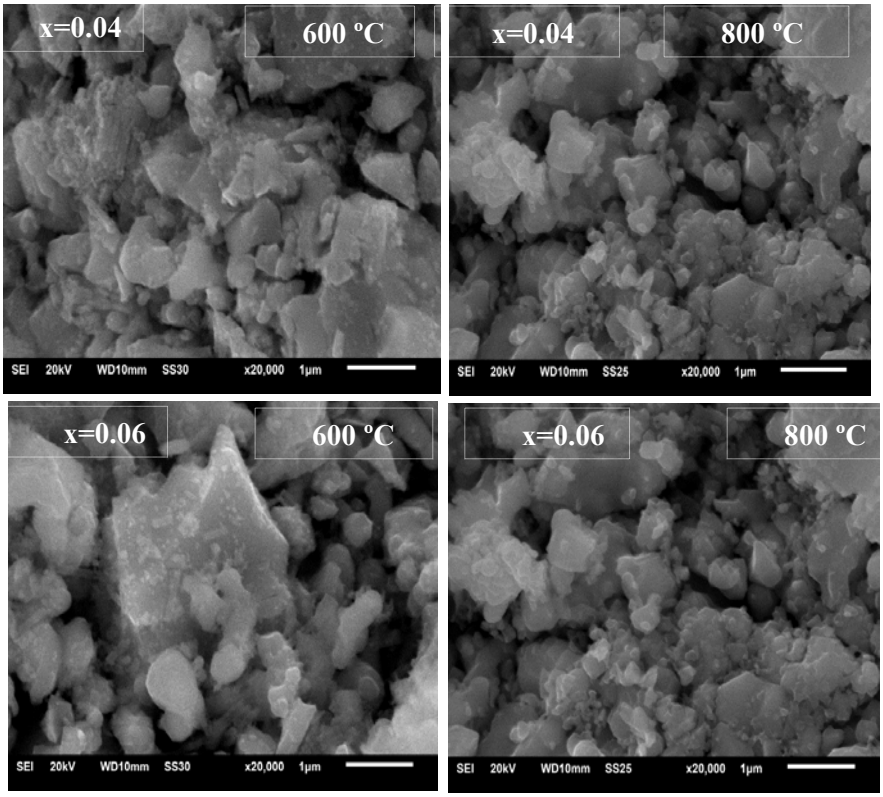

Fig. 7.2: SEM micrographs of LBMO/xTiO$_2$ system for x= 0.04 and x=0.06 composites annealed at 600 and 800 °C.

7.2 Magnetic properties

The thermal variation of dc magnetization at 100 Oe applied magnetic field is shown in Fig. 7.3a and Fig. 7.3b for composites annealed at both annealing temperatures. The FM-PM transition temperature, T_c, is observed at the same value (348 K) for all annealed composites. This means the non effect on grain ferromagnetism by the annealing temperature as a result of the TiO$_2$-LBMO interaction lack preservation. The magnetization value of doped composites increases with rising up the annealing temperature, in agreement with [104,105]. This change in composites magnetization with changing annealing temperature

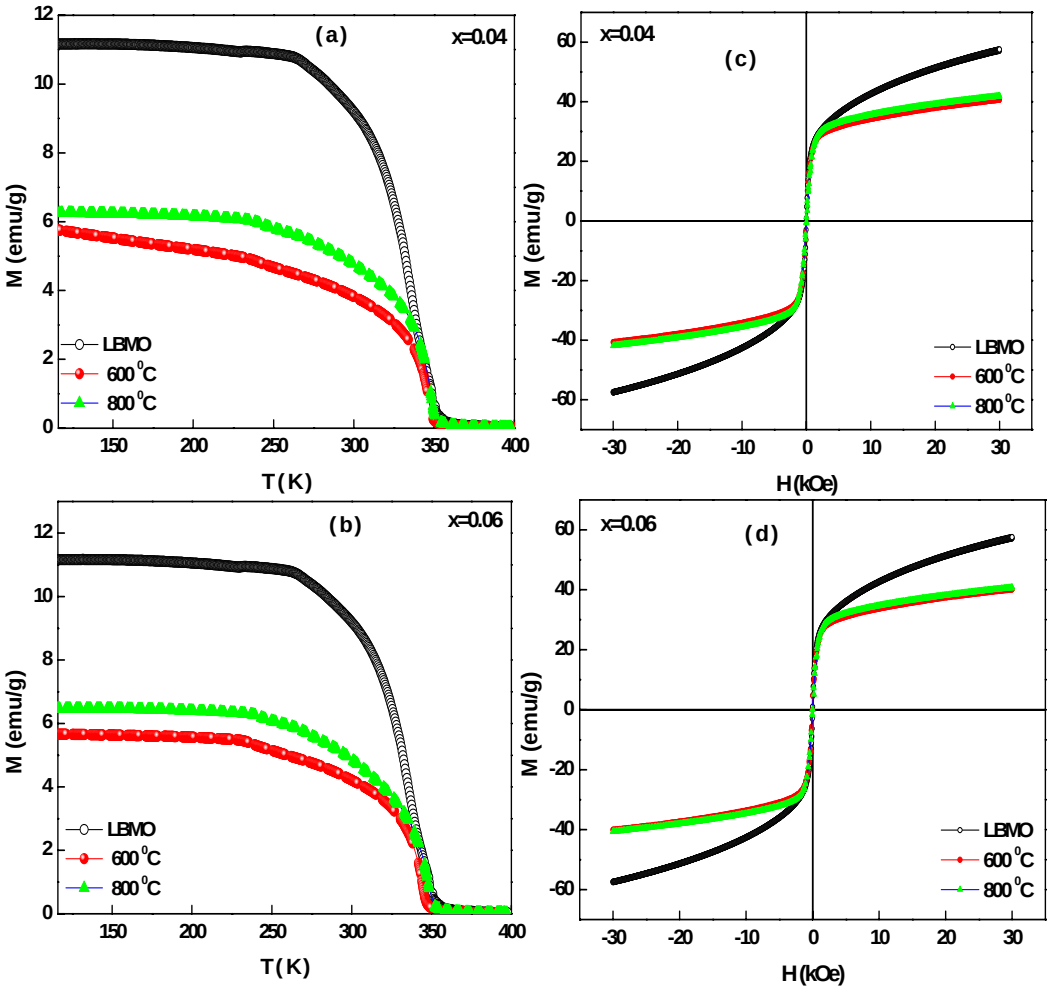

Fig. 7.3: (a), (b) Thermal dependence of magnetization at 100 Oe and (c), (d) hysteresis loops at 300K of LBMO/*x*TiO_2 composites annealed at 600 ºC and 800 ºC, respectively.

Table 7.2: Curie temperature (T_c), saturation magnetization (M_s) and coercive field (H_c) of doped composites annealed at 600 °C and 800 °C.

composite	condition	T_c (K)	M_s (emu/g)	H_c(Oe)
x=0	as-prepared	348	47	50
x=0.04	600 ºC	348	33.7	40
	800 ºC	348	38.4	44
x=0.06	600 ºC	348	31.3	16
	800 ºC	348	35.2	31

may be attributed to intrinsic and/or extrinsic effects. The intrinsic effect is concerned with the changes in LBMO bandwidth or grain size [103]. While, the extrinsic effect arises from GBs that decrease grains connectivity and interrupt interfacial magnetization leading to magnetization pinning. The negligible change in the grain size with changing annealing temperature suggests the intrinsic spin disorder stability [106-108], which indicates the grain size negligible role in the magnetization change. In addition, the change in LBMO bandwidth happens only in case of the partial substitution of Mn ions by Ti^{4+} ions that is excluded in our case due to the complete TiO_2-LBMO interaction lack. This suggests that the magnetization change is more likely arising from an extrinsic effect of the GBs factor rather than intrinsic effect. As a deep insight in the magnetization change, we studied the effect of annealing temperature on GBs. To discuss this point, it is important to keep in mind that the GBs thickness and resistance increase with TiO_2 segregation, which in turn increases the magnetization pinning. The TiO_2 grains agglomeration seems to be enhanced with increasing the annealing temperature (800°C) as seen in Fig. 7.2, this decreases their random distribution at the GBs that decreases the magnetization pinning and hence increases the magnetization value. Vice-versa, annealing process at the lower temperature of 600°C decreases TiO_2 agglomeration increasing their random distribution at the GBs that increases magnetization pinning and hence decreases the magnetization value. According to the annealing temperature effect on TiO_2 distribution and its effect on magnetization value, the experimental results of hysteresis loops in Fig. 7.3c and Fig. 7.3d reveal that the composites annealed at the higher temperature

of 800°C show the highest saturation magnetization (M_s) and coercive field (H_c) values, see Table 7.2, in agreement with [109]. As discussed earlier, this is due to the better ordering and the well agglomeration of TiO_2 grains away from the LBMO GBs in composites annealed at 800°C rather than in those annealed at 600°C.

7.3 Magnetocaloric effect

Fig. 7.4 shows the isothermal magnetization curves of LBMO doped composites annealed at 600 °C and 800°C. Both composites after both annealing treatments show the same behavior in M(H) curves. Where, the magnetization below T_c increases sharply at low magnetic fields thereafter saturates at high magnetic fields, in correspondence with the ferromagnetic behavior. While above T_c, the magnetization changes linearly with the applied magnetic field as a feature of paramagnetism. Arrott plots in Fig. 7.5 show a positive slope around T_c for composites annealed at 600 and 800°C temperatures. The plots indicate the stability of the second order FM-PM transition with changing annealing temperature.

With respect to ΔS, Fig. 7.6 displays the thermal variation of ΔS for doped composites for both annealing temperatures. The effect of different annealing temperature on ΔS_{max} is negligible as we can see in Table 7.3. This is because the change in ΔS_{max} depends on the change in the intrinsic properties of LBMO compound, which are preserved as a result of the TiO_2-LBMO interaction lack. Contrarily, the annealing temperature effect appears clearly on the δT_{FWHM}, where, it increases with the annealing temperature increasing as seen in Table 7.3.

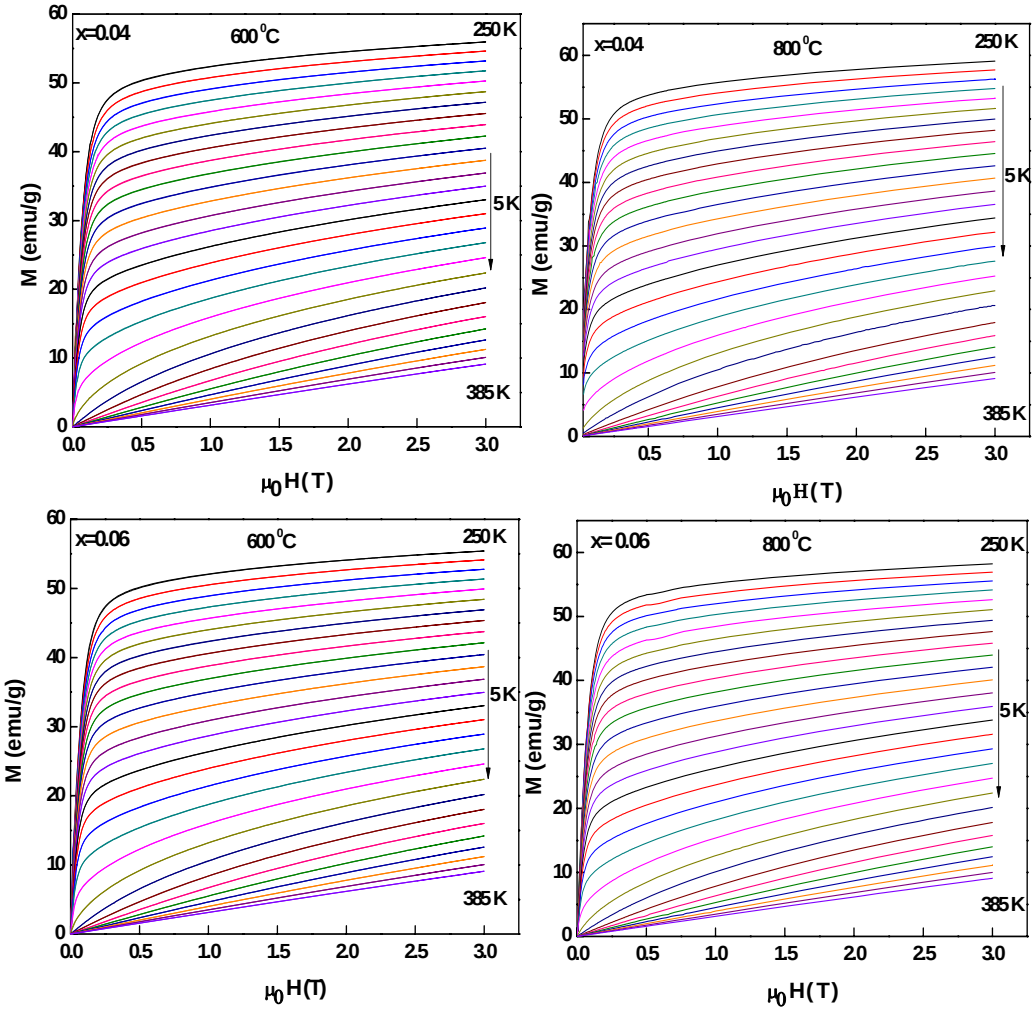

Fig. 7.4: Isothermal magnetization curves of x=0 and doped composites x=0.04 and x=0.06 annealed at 600 ºC and 800 ºC.

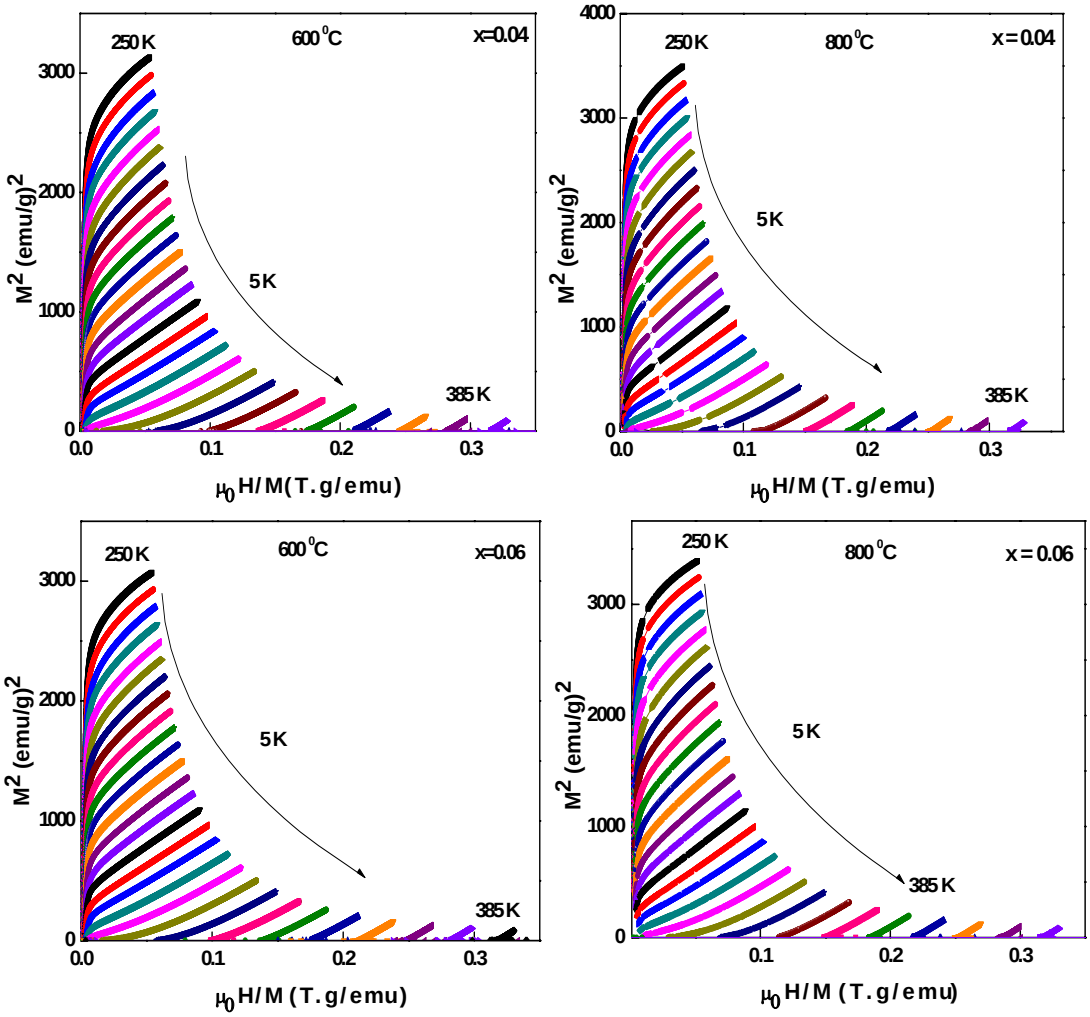

Fig. 7.5: Arrott plots of LBMO/*x*TiO_2 doped composites x=0.04 and x=0.06 composites annealed at 600 °C and 800 °C.

Accordingly, the MCE properties are enhanced. Fig. 7.7a and Fig. 7.7 b show the enhancement in RCP values of doped composites at the same temperature range with the annealing temperature increase. Once again, the promotion in the MCE properties refers to the enhancement in the δT_{FWHM} rather than in ΔS_{max} due to the negligible change in ΔS_{max} with changing annealing temperature. From these results, an important note may be drawn, annealing treatment at the higher temperature of 800°C exhibits interesting results more than ones at 600°C. This suggests using the high annealing temperatures to improve the MCE properties in these systems.

The temperature dependence of the exponent power ***n*** is displayed in Fig. 7.7c and Fig. 7.7d for composites annealed in both annealing temperatures. It is noteworthy that ***n*** values of composites annealed at the higher temperature of 800 °C are closer to the mean field theory value than ones corresponding to samples annealed at the 600 °C.

Based on *Landau* theory, the calculations have shown the negligible effect of annealing temperature on the MCE mechanism. Coefficients ***a*** and ***b*** do not change significantly with changing annealing temperature as shown in Fig. 7.8a and Fig. 7.8b, and $b(T_c)$ still has a positive value confirming the second order transition after annealing treatments. The difference between the experimental value of ΔS and the one based on *Landau* theory can be appreciated in both annealing temperatures, indicating the non effect of annealing temperature on the MCE mechanism.

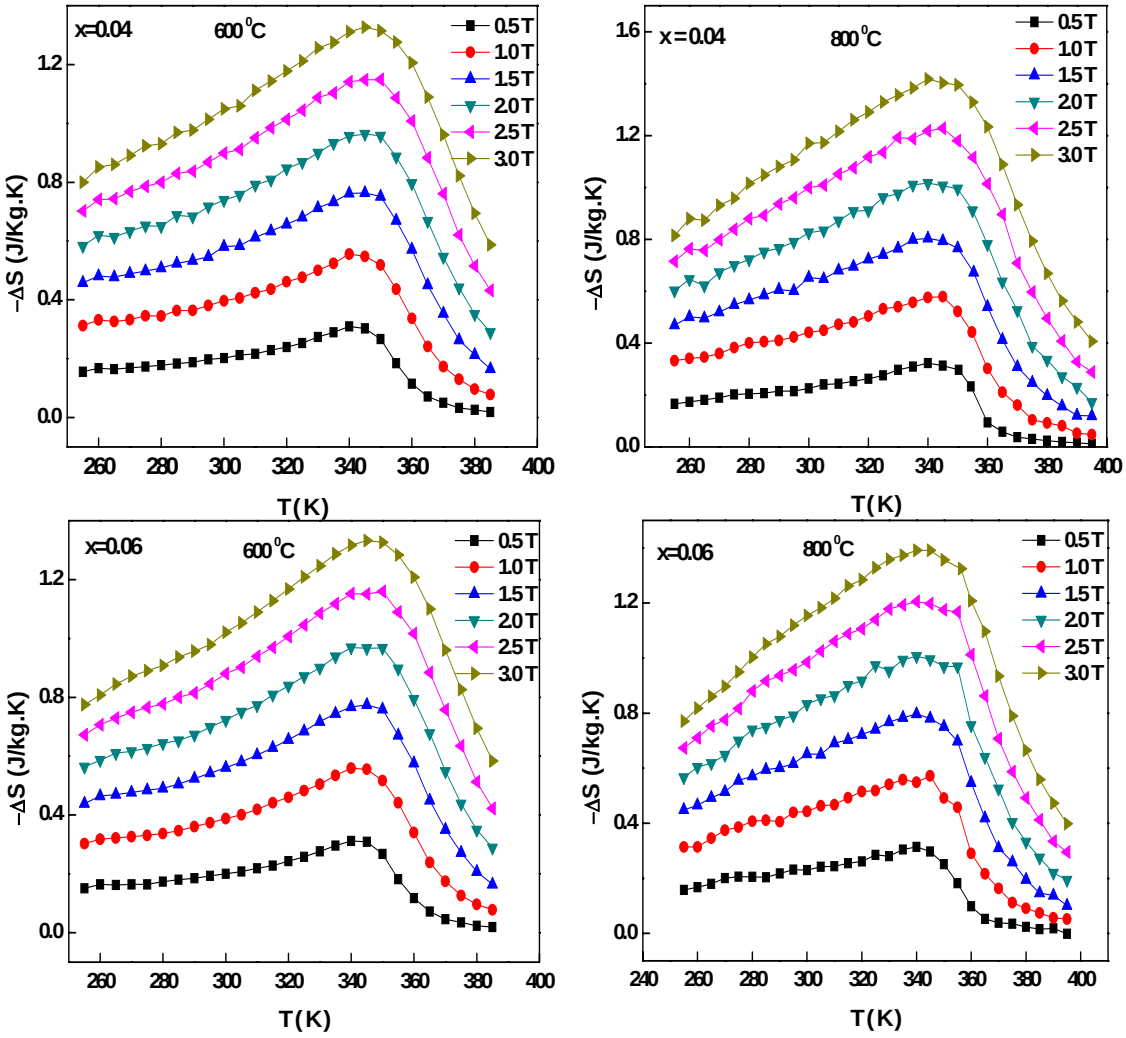

Fig. 7.6: Thermal variation of magnetic entropy change at different magnetic field variations for x=0.04 and x=0.06 composites annealed at 600 ºC and 800 ºC.

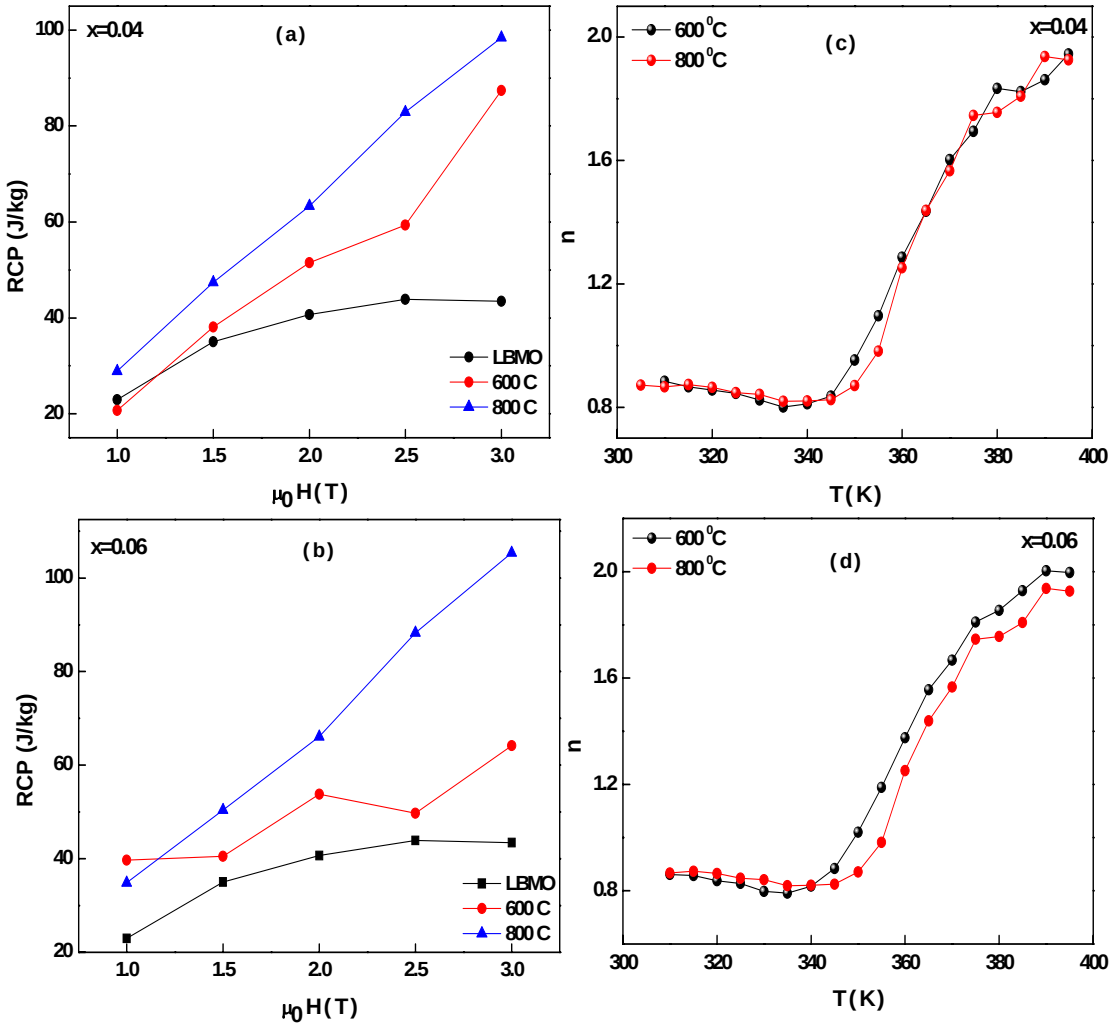

Fig. 7.7: (a), (b) The variation of RCP with magnetic field change and (c), (d) exponent n versus temperature for x=0.04 and x=0.06 composites annealed at 600 ºC and 800 ºC.

Table 7.3: ΔS_{max}, δT_{FWHM}, RCP at magnetic field change of 2T and exponent *n* of composites annealed at 600 ˚C and 800 ˚C.

composite	condition	ΔS_{max}(J/kg .K)	δT_{FWHM} (K)	RCP(J/kg)	n
x=0	as-prepared	-1.34	30.15	40.66	0.7
x=0.04	600 ºC	-0.96	53	50	0.95
	800 ºC	-1.001	62	62	0.87
x=0.06	600 ºC	-0.966	54	52	1.02
	800 ºC	-1.006	66	66	0.87

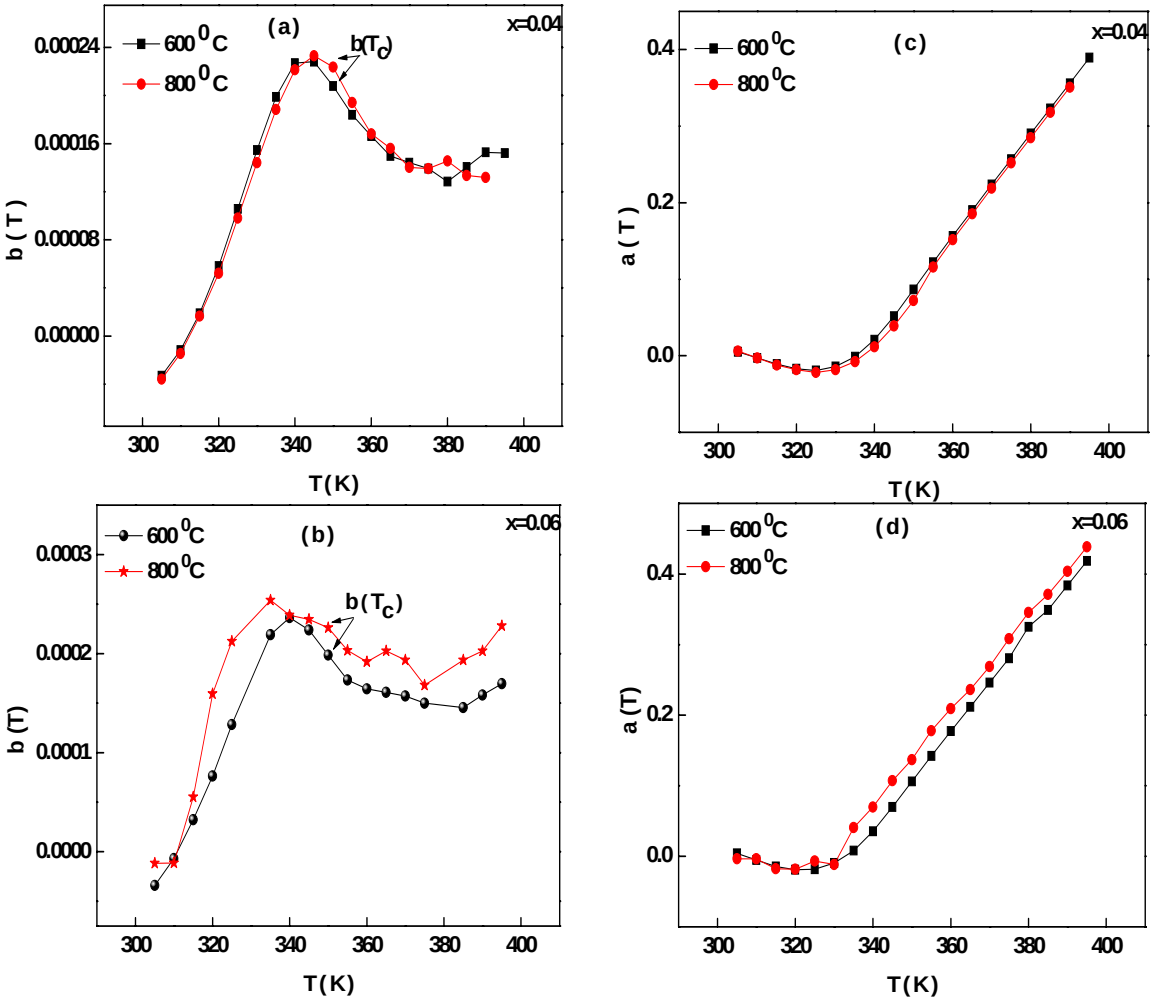

Fig. 7.8: (a, b) and (c, d) The thermal variation of *b* and *a* coefficients, respectively, for x=0.04 and x=0.06 composites annealed at 600 and 800 ºC.

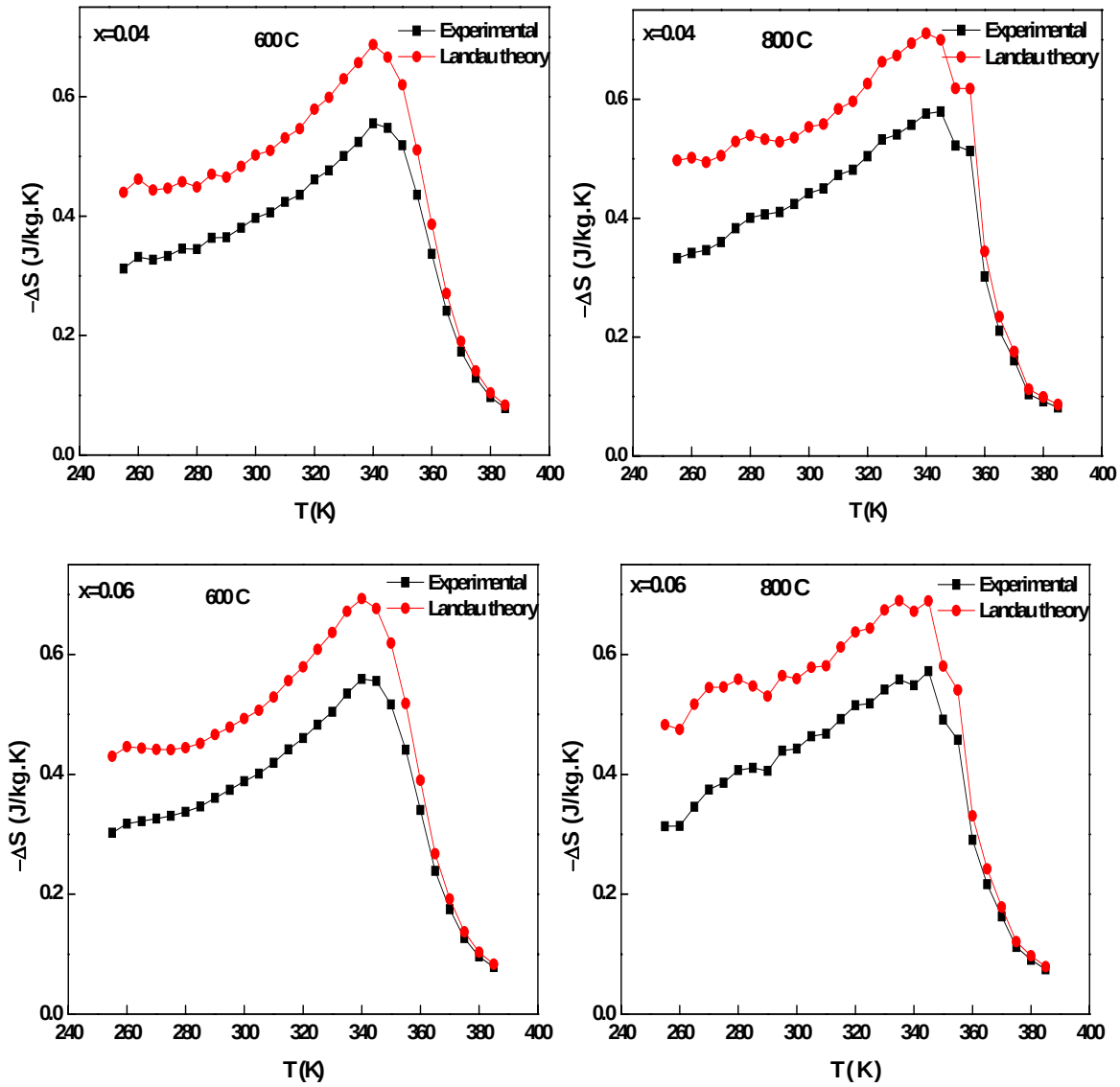

Fig. 7.9: Experimental and Landau theory based calculation of ΔS for magnetic field change of 1T, for x=0.04 and x=0.06 composites annealed at 600 ºC and 800 ºC.

CH. 8 Effect of secondary phase size on the magneto-transport properties of LBMO compound

After the effect of secondary phase ratio and annealing treatment on the magneto-transport properties of LBMO manganite compound have been studied, it is interesting to complete this investigation by studying the effect of interface/secondary phase size. This has been done by introducing different sizes of Ni and Ag secondary phases with the ferromagnetic LBMO manganite compound. In this way we can investigate the GBs resistance sensitivity to the interface size and its effect on transport, magnetic, magnetoresistive and MCE properties of LBMO compound.

8.1 Structural properties

The XRD patterns in Fig. 8.1 show extra peaks of Ni and Ag interfaces with the LBMO phase in doped composites. The existence of these extra peaks in doped composites reveals the dopants interaction lack with the LBMO compound. This suggests the interfaces segregation on the surfaces and between the LBMO GBs, which is confirmed by the SEM micrographs in Fig. 8.2. The interface-LBMO interaction lack leads to the structural properties stability in all composites as the R-3c rhombohedral structure, the insignificant change in the cell volume, the average SEM grain size and the average crystallite size (P) as displayed in Table 8.1, Rietveld profiles are presented in Fig. 8.1c,d. It is noteworthy to state that the XRD analysis exhibits the NiO presence in LBMO/Ni_{powder} composite instead of the Ni element that might be oxidized through the annealing process. Also, it is well observed the higher intensity of the Ni peak in LBMO/Ni_{powder} composite in comparison with this in the LBMO/Ni_{NWs}

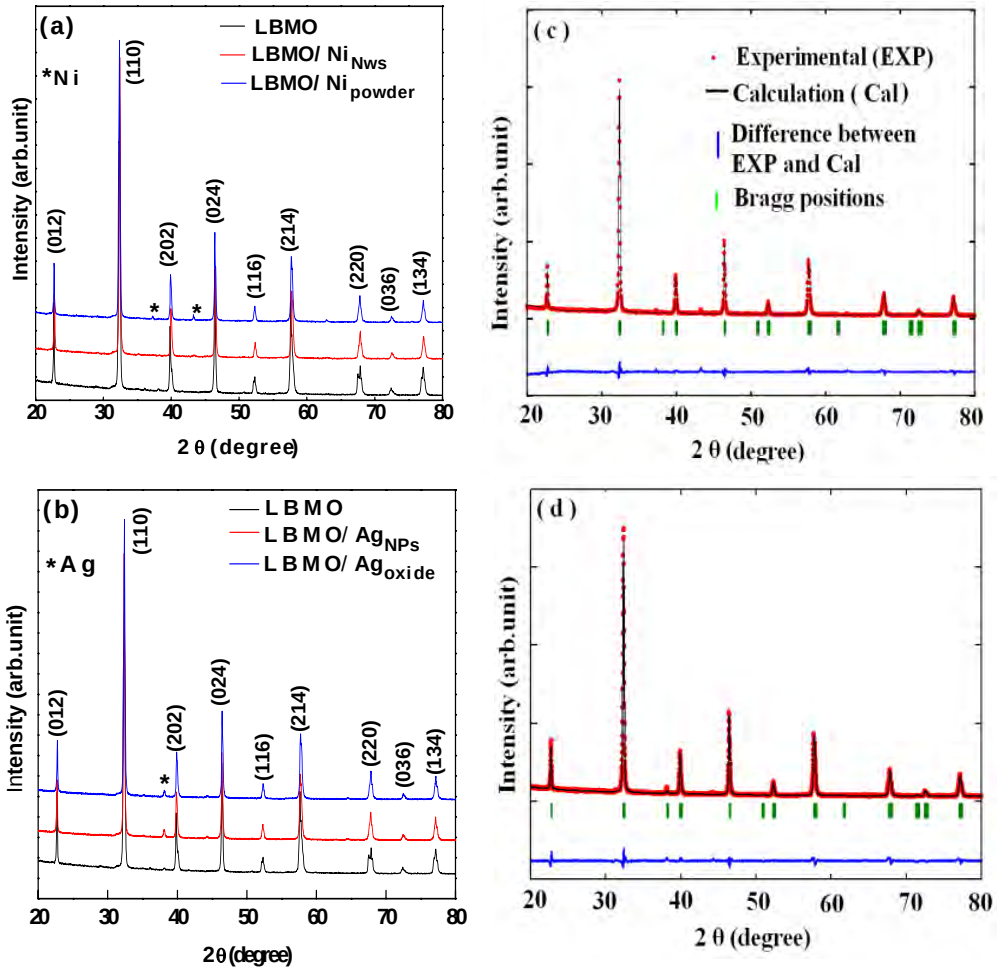

Fig. 8.1: (a), (b) XRD patterns for LBMO/Ni and LBMO/Ag doped composites respectively, and (c), (d) Rietveld profiles for LBMO/Ni_{powder} and LBMO/Ag_{oxide} composites, respectively.

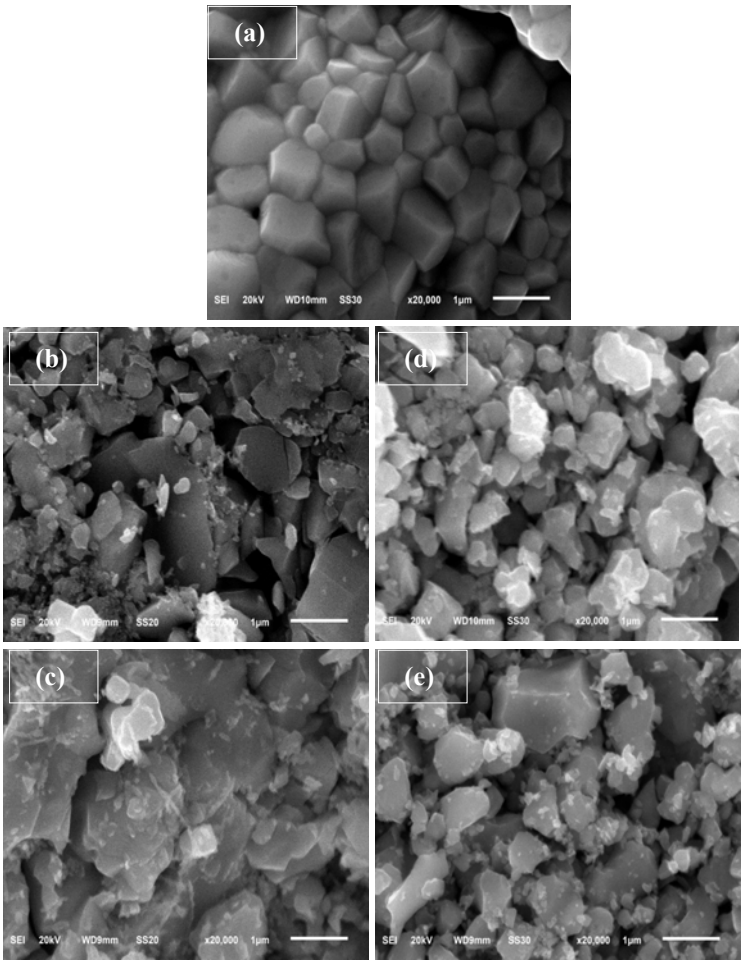

Fig. 8.2: SEM micrographs for LBMO doped composites, where, (a) LBMO, (b) LBMO/Ni_{powder}, (c) LBMO/Ni_{NWs}, (d) LBMO/Ni_{powder} and (e) LBMO/Ag_{NPs} doped composites, respectively.

Table 8.1: Phase symmetry, cell volume (V), the average SEM grain size (G) and the average crystallite size (P) for LBMO doped composites.

composite	Phase symmetry	V(Å)^3	G (µm)	P(nm)
LBMO	R3-c rhombohedral	358.8	0.74	32
LBMO/Ni_{powder}	R3-c rhombohedral	358.5	0.70	35
LBMO/Ni_{Nws}	R3-c rhombohedral	357.0	0.65	34.7
LBMO/Ag_{oxide}	R3-c rhombohedral	358.4	0.72	35.7
LBMO/Ag_{NPs}	R3-c rhombohedral	358.4	0.75	35.4

composite. This difference in peak intensity may be attributed to the smaller size of Ni NWs that enables some of them to interact substitutionally with Mn ions in the LBMO compound, which decreases the segregated amount and leads to the smaller Ni peak intensity in the LBMO/Ni_{NWs} composite. In contrast, the similar Ag peak intensity in both Ag-doped LBMO composites (oxide and NPs) reveals the complete interaction lack between the Ag interfaces and the LBMO compound.

8.2 Transport properties

The temperature dependence of zero magnetic field resistivity in Fig. 8.3 shows the metal-semiconductor transition for all composites at the T_{ms} temperature. The presence of Ni and Ag interfaces increases the LBMO resistivity and shifts its T_{ms} towards lower temperatures (see Table 8.2), in agreement with the results in Refs. [15-17]. Due to the interface-LBMO interaction lack, the change in LBMO transport properties with the introduced interfaces is suggested to has an extrinsic origin arising from the GBs effect. In other words, the presence of such interfaces between LBMO grains increases their boundaries resistance [17] that promotes carriers scattering and increases the resistivity. As mentioned before, the situation is visualized as an interruption in the direct contact between the LBMO grains through the increase in their boundaries thickness due to the interfaces accumulation [73]. The change in GBs resistance with the introduced interfaces can be experimentally realized through the low temperature resistivity increase (ρ_{100K}), see Table 8.2, which mainly arises from the GBs effect [14]. Fig. 8.3 also shows the LBMO resistivity dependence on the interface size, which

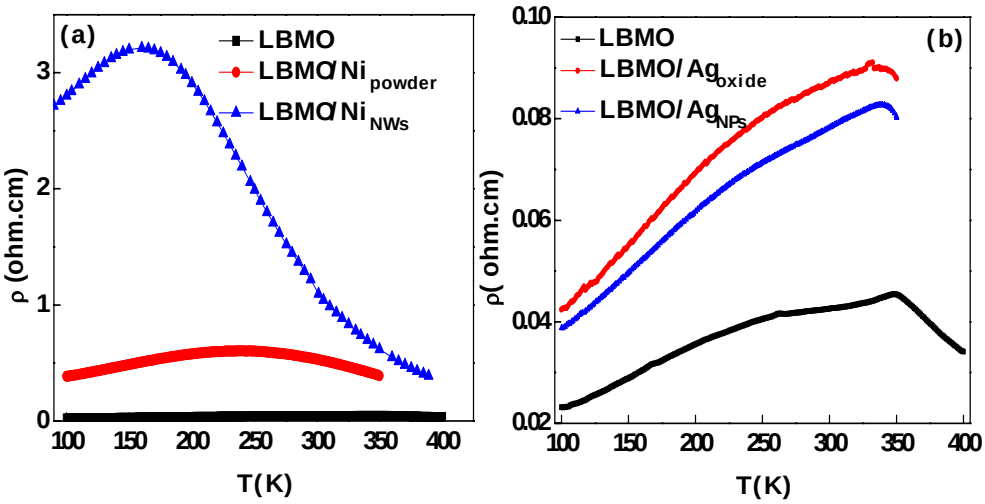

Fig. 8.3: The temperature dependence of resistivity for (a) LBMO/Ni and (b) LBMO/Ag composites, respectively.

reveals the GBs sensitivity to the introduced interface size. For example, the LBMO/Ag_{NPs} composite shows a smaller resistivity and a higher T_{ms} value than the LBMO/Ag_{oxide} composite. This is because of the different interfaces distributions at GBs according to their sizes that leads to different changes in the GBs resistance. The SEM micrographs in Fig. 8.2 show the well agglomeration of the smaller size interfaces (Ni Nws and Ag NPs) away from boundaries leading to a small effect on the GBs resistance in these doped composites. This can be drawn through the smaller value of ρ_{100K} of LBMO/Ag_{NPs} in comparison with LBMO/Ag_{oxide} (see Table 8.2). However, Ni-doped composites do not obey this scenario, where, the LBMO/Ni_{Nws} composite shows a higher resistivity and a smaller T_{ms} value than the LBMO/Ni_{powder} composite in spite of the well agglomerated Ni Nws away from the GBs. This is because the proposed scenario works only with the resistivity arising from extrinsic factors (i.e a change in GBs resistance). While in the LBMO/Ni_{Nws} composite, there is an additional intrinsic resistance component (ρ_{int}). This ρ_{int} arises from the ferromagnetic DE interactions

Table 8.2: Transport, magnetoresistive, magnetic and magnetocaloric parameters for LBMO/$Ni_{0.02}$ and LBMO/$Ag_{0.02}$ systems.

composite	T_{ms}(K)	T_c (K)	$\rho_{100\ K}$ (Ω.cm)	MR_{300K} (%)	δT_{FWHM} (K)	RCP (J/kg)
LBMO	350	348	0.023	-1.23	24	44
LBMO/Ni_{powder}	240	348	0.38	-4.35	70	107
LBMO/Ni_{Nws}	160	342	2.8	8.05	106.7	167
LBMO/Ag_{oxide}	332	348	0.042	-7.9	57.37	92
LBMO/Ag_{NPs}	338	348	0.038	-5.25	58.63	94

(Mn^{3+}-O-Mn^{4+}) suppression and the promotion of Mn-O-Ni bonds due to the small partial substitution of Mn by Ni. Mn-O-Ni bonds are non double exchange interactions with an antiferromagnetic nature and result in a stronger localization of the e_g electron, which explains the notable increase in the resistivity of this doped composite as seen in Fig. 8.3.

8.3 Magnetoresistive properties

Fig. 8.4 shows a negative MR for all composites over the whole temperature range except the LBMO/Ni_{Nws} composite that shows a crossover from negative to positive MR at a certain temperature. The MR of LBMO compound is enhanced in all doped composites (except the LBMO/Ni_{Nws} composite), and the MR peak is shifted towards room temperature with an improvement of -3.7%, -4.9% and -8.2% for Ni_{powder}, Ag_{NPs} and Ag_{oxide} interfaces, respectively, in agreement with Refs.[80,85, 110]. The LFMR promotion includes the room temperature values (300K) as displayed in Table 8.2. The enhanced LFMR with the introduced interfaces refers to the spin polarized tunneling process between

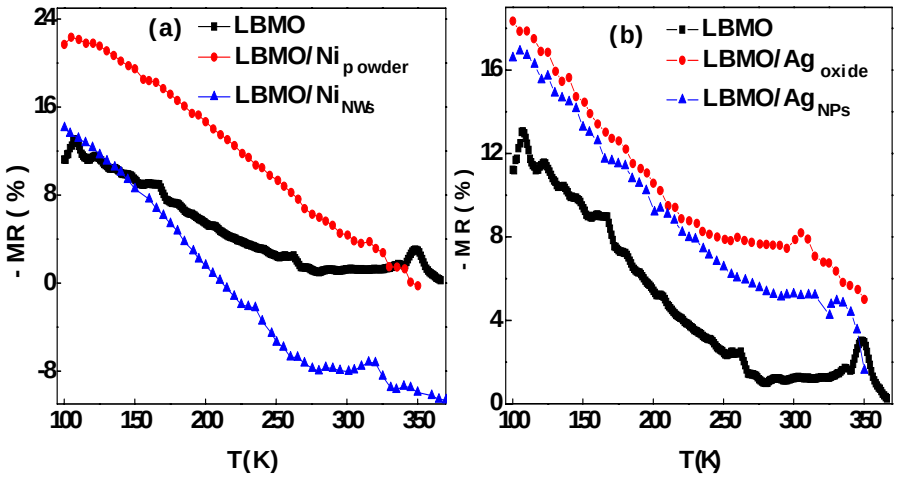

Fig. 8.4: The temperature dependence of MR at 0.5T applied magnetic field for (a) LBMO/Ni and (b) LBMO/Ag composites, respectively.

grains due to the increase in GBs resistance [18, 111]. The LFMR results show an interface size dependent behavior, where, high LFMR values can be observed with the higher interface size as seen in Fig. 8.4. This is because of the spin tunneling process dependence on the GBs thickness, which in turn increases with the interface size.

The anomalous behavior of the MR sign change in the LBMO/Ni_{Nws} composite can be explained (as mentioned in Ch.5) according to the spin carriers near the $\mathbf{E_F}$. The spin carriers change has been suggested to appear in Ni Nws-doped composite. In LBMO compound, Ba^{2+} electrons remain at the e_g band of the Mn ion acting as the major spin carriers near the $\mathbf{E_F}$, which is the negative MR case. This case is preserved in Ni Powder and both Ag-doped composites due to the complete interaction lack. While due to the partial substitution process in the LBMO/Ni_{Nws} composite, Ni electrons occupy the e_g band of Mn ion at low temperatures keeping the majority spin carriers near the $\mathbf{E_F}$ and the negative

MR. However, with temperature elevation Ni electrons are no longer remaining in the e_g band and instead migrate to the $t_{2g}^{\downarrow}$ band whose edge is quite closer to the $\mathbf{E_F}$ than to the e_g band. The occupation of the $t_{2g}^{\downarrow}$ band by the Ni electrons causes these Mn ions to adopt an antiparallel alignment with the system being as minority spin carriers near the $\mathbf{E_F}$ leading to the positive MR [82].

8.4 Magnetic properties

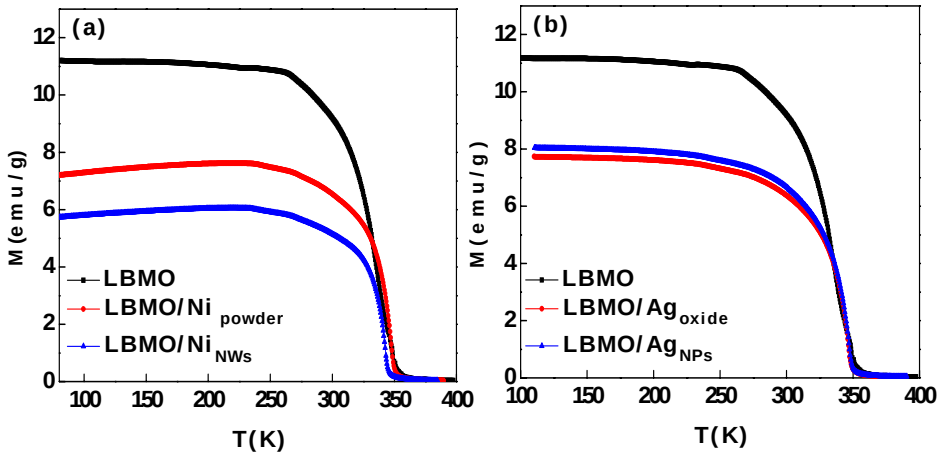

Fig. 8.5: Thermal dependence of dc magnetization at 100 Oe applied magnetic field for (a) LBMO/Ni and (b) LBMO/Ag composites, respectively.

Fig. 8.5 displays the temperature dependence of magnetization curves, at 100 Oe applied magnetic field, for Ni and Ag doped composites. All composites exhibit the FM-PM transition at T_c. Two important features can be drawn from this figure. The first is the constant value of the LBMO compound T_c at 348K with the introduced Ni_{powder} and both Ag interfaces (see Table 8.2), in agreement with results reported in Ref. [112]. The constant value of T_c refers to its intrinsic character and its dependence on the grain internal ferromagnetism, which remains unchanged due to the complete interaction lack in these composites.

Furthermore, the incomplete interaction lack in the LBMO/Ni_{Nws} composite decreases the T_c value to 342K as a result of the Mn ion partial substitution process, which suppresses ferromagnetism due to the Mn-O-Ni antiferromagnetic bonds formation. The second note is concerned with the magnetization change, where, the LBMO magnetization decreases with interfaces introduction. The interaction lack in doped composites excludes intrinsic factors role in the magnetization change and instead shows up the GBs role [112]. In principal, we can say that the ferromagnetism inside LBMO grains is interrupted and pinned by the GBs. And both Ni and Ag interfaces increase the GBs thickness and resistance, leading to an increase in ferromagnetism pinning and confinement inside grains. This explains the LBMO magnetization decrease with interfaces introduction. It is noteworthy the magnetization dependence on the interface size that may be attributed to the GBs resistance sensitivity to the interfaces size. This is because the low GBs resistance reduces pinning effect, therefore, the smaller interface size the higher magnetization value in doped composites, and vice-versa. This is clearly seen in both LBMO/Ag composites, where, the LBMO/Ag_{NPs} composite shows a relatively higher magnetization value than the respective of the LBMO/Ag_{oxide} composite. Again, this explanation may not be convenient for Ni-doped composites, since the LBMO/Ni_{powder} composite shows a magnetization value greater than the LBMO/Ni_{NWs} composite. The reason for this anomalous behavior also refers to the intrinsic effects, which are added to the extrinsic ones due to the small Mn partial substitution process in the LBMO/Ni_{NWs} composite. As a consequence, the magnetization change in this composite consists of two

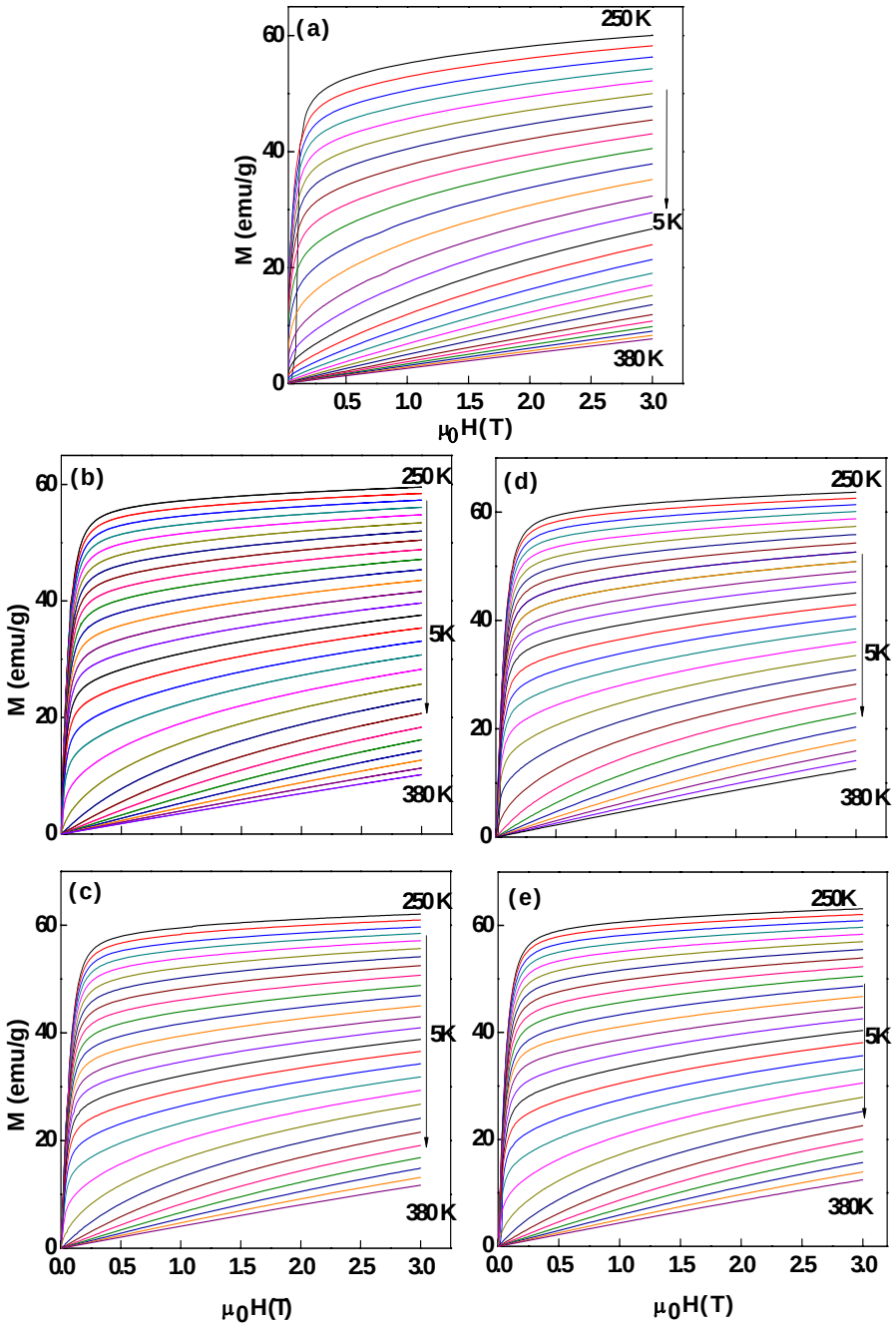

Fig. 8.6: Isothermal magnetization curves of (a) LBMO, (b) LBMO/Ni_{Powder}, (c) LBMO/Ni_{Nws}, (d) LBMO/Ag_{oxide} and (e) LBMO/Ag_{NPs} doped composites.

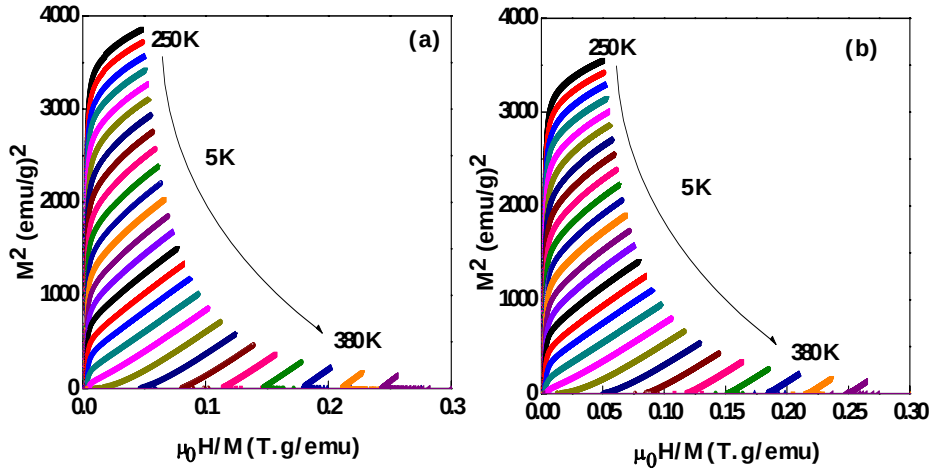

Fig. 8.7: Arrott plots for (a) LBMO/Ni_{Nws} and (b) LBMO/Ni_{powder} doped composites as selected examples.

components, an extrinsic one coming from the magnetization pinning by GBs, and the other arising from the ferromagnetism suppression due to the Mn-O-Ni antiferromagnetic bonds. Fig. 8.6 shows the isothermal magnetization curves of the LBMO compound with different introduced interfaces. The derived Arrott plots in Fig. 7 prove the second order magnetic transition type for all composites due to the positive slope around T_c [90]. This reveals the non impact of LBMO magnetic transition type by the introduced interfaces.

8.5 Magnetocaloric effect

The temperature dependence of ΔS displayed in Fig. 8.8 shows a maximum (ΔS_{max}) around T_c, which increases monotonically in amplitude with the applied magnetic fields. In spite of the negligible change in ΔS_{max} value of LBMO with the introduced Ni and Ag interfaces, there is no registered change in its temperature position that means an unchanged working temperature range (around the same T_c value). The working temperature range stability refers to the intrinsic properties preservation due to the interaction lack. Where, ΔS has a

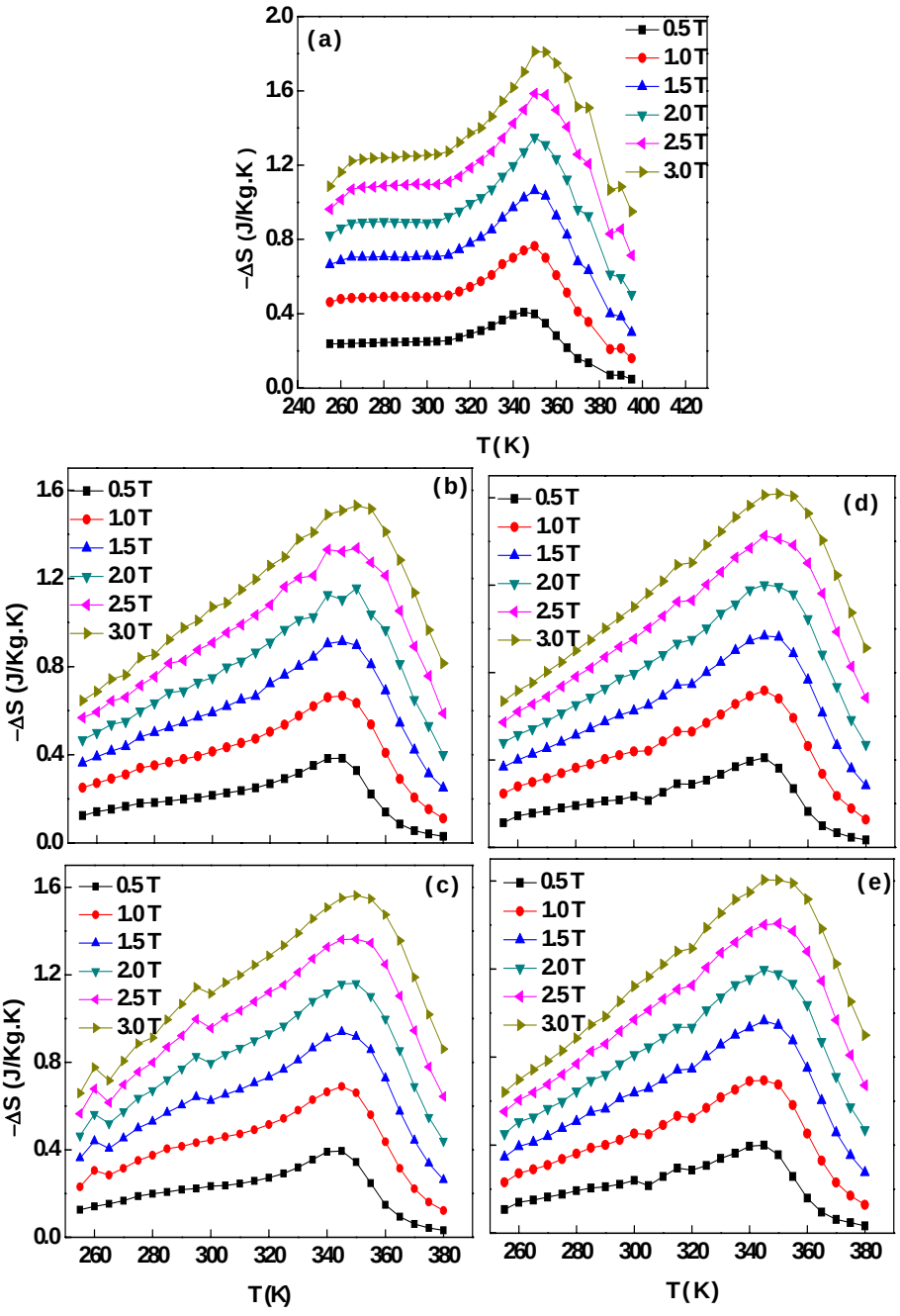

Fig. 8.8: The temperature dependence of ΔS at different applied magnetic field change for (a) LBMO, (b) LBMO/Ni_{Powder}, (c) LBMO/Ni_{NWs}, (d) LBMO/Ag_{oxide} and (e) LBMO/Ag_{NPs} doped composites.

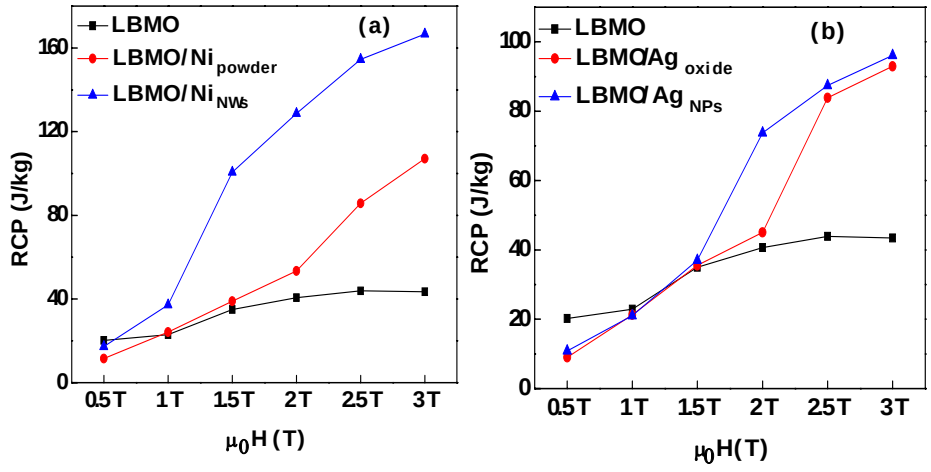

Fig. 8.9: Magnetic field dependence of RCP for (a) LBMO/Ni and (b) LBMO/Ag doped composites.

strong correlation with the ferromagnetic intrinsic Mn^{3+}/Mn^{4+} DE interaction and the T_c that is kept unchanged. Moreover, despite the negligible change in the ΔS_{max} value of the LBMO compound with Ni and Ag interfaces introduction, results in Table 8.2 show the enhancement in the δT_{FWHM} value of the LBMO with the introduced interfaces. This implies an increase in the MCE working temperature range, in agreement with the previous reported results of the LBMO/TiO_2 in ch. 6. RCP values are displayed in Fig. 8.9 and the figure shows the notable enhancement in the RCP values of the LBMO compound with the introduction of Ni and Ag interfaces at applied magnetic fields ≥1.5T. Also, it is noteworthy the greater enhancement with the smaller size introduced interfaces in doped composites in comparison with the larger size ones, in agreement with *M. Pekala et al* .[113]. For example, Table 8.2 shows that the RCP value of the LBMO compound is improved from 44 J/kg to 107 J/kg and 167 J/kg with Ni powder and Ni NWs introduction, respectively, and to 92 J/kg and 94 J/kg with

the introduction of Ag oxide and Ag NPs interfaces, respectively, at 3T applied magnetic field. From MCE measurements, it can be concluded that the magnetocaloric properties of the LBMO compound are enhanced with different interface sizes of Ni and Ag at the same temperature range.

CH. 9 Magnetocaloric-transport properties correlation in LBMO compound

9.1. Aspects

As mentioned earlier, the anomalous behavior of ρ near T_c in manganites has been interpreted using the DE interaction between Mn ions (Mn^{3+}-O-Mn^{4+}) [2]. This anomalous behavior suggests a coupling between magnetic and transport properties. The magneto-transport properties correlation has been described mathematically by *Hundely et al.* through the $\boldsymbol{\rho=\rho_0\, exp\ (-M/\alpha)}$ expression [114], where, $\boldsymbol{M}$ is the magnetization and $\boldsymbol{\alpha}$ is a constant depends on sample magnetic properties. Later, *O'Donnell et al.* suggested the $\boldsymbol{\rho=\rho_0\, exp(-M^2/\alpha)}$ equation [115] as an exact form of this coupling, then after, *Chen et al.* [116] modified the relation to $\boldsymbol{\rho=\rho_0\, exp(-M^2/\alpha T)}$ for small and intermediate magnetization values around T_c. Magnetic field application suppresses resistivity by increasing spin ordering leading to the CMR around T_c, and simultaneously, this is accompanied by a change in ΔS leading to the MCE.

The similar behavior of ΔS, ρ and CMR around T_c supports the magneto-transport correlation and indicates the important role of spin order/disorder feature in these effects. *Xiong et al.* [117] have reported Eq. 9.1 as a mathematical description of ΔS-ρ correlation in magnetic materials, where, $\boldsymbol{H}$ is the applied magnetic field. The magnetic spin-disorder (that characterizes ΔS) is high around T_c and leads to magnetic polarons formation that affect carriers transport and hence ρ [117]. At low temperatures, the ferromagnetic ordering results in magnetic polarons suppression and therefore the validity of Eq. 9.1 is expected to be only around T_c.

$$\Delta S = -\alpha \int_0^H \frac{\delta \ln \rho}{\delta T}\, dH \qquad (9.1)$$

$$\rho(T,H)-\rho(T,0)=K\ [S(T,H)-S(T,0)] \qquad (9.2)$$

$$\Delta\rho_H = K\ \Delta S_M \qquad (9.3)$$

Similarly, a dependence relation has been observed between ΔS and MR ($\Delta\rho_H$) in TmCu and TmAg compounds [118]. *Sakamoto et al.* [119] managed to formulate this dependence in Eq. 9.2, which can be simplified to Eq. 9.3; ***K*** is the proportionality constant. In the following part we will study the correlation between the magnetocaloric effect and transport properties in terms of ΔS, ρ and MR in the $La_{0.7}Ba_{0.3}MnO_3$ manganite compound. The reason for studying this correlation only for the parent compound is that its T_{ms} is very close to T_c, while in doped composites the intense grain boundaries affect the T_{ms} and shift it far away from T_c.

Fig. 9.1a shows the temperature dependence of field and zero-field resistivity of the LBMO compound. The zero-field T_{ms} (350K) of LBMO compound is very close to its reported T_c (348K). With the magnetic field application, the resistivity is suppressed and the T_{ms} is shifted towards higher temperatures of 360K, 365K and 370K for 1, 2 and 3T applied magnetic fields. This effect is ascribed to the spin order enhancement with the applied magnetic field that promotes the DE interaction leading to an easy carriers transport. Resistivity suppression with magnetic field application leads to the CMR effect around T_c. Fig. 9.1b shows that the high values of MR at low temperatures decrease with temperature increasing and passing through a sharp peak near T_c. The low temperature MR refers to the extrinsic spin dependent tunneling effect

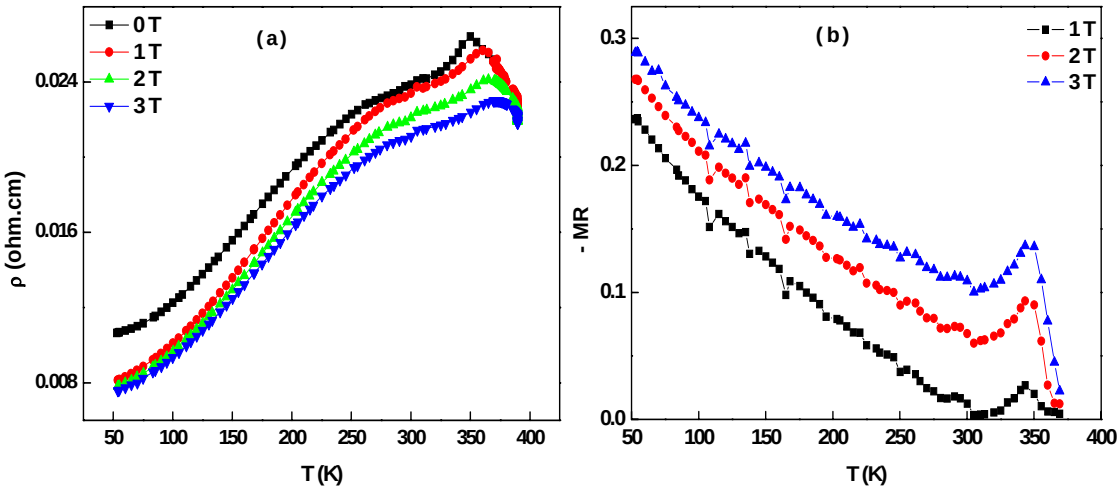

Fig. 9.1: The temperature dependence of (a) resistivity and (b) magnetoresistance for LBMO compound at 1, 2 and 3T applied magnetic fields.

and scattering process across GBs [18]. While, the CMR peak around T_c is an intrinsic resultant of the spin disorder suppression and the DE mechanism [1].

9.2 Magnetocaloric effect-resistivity correlation

The thermal variation of experimental ΔS and ΔS based on electrical resistivity calculations, $\Delta S\ (\rho)$, for the LBMO compound are presented in Fig. 9.2, α=240 emu/g as reported by *Patra et al.* [120]. The observed similar behavior between these two curves reveals the influence on electrical transport by magnetic polarons around T_c, which are driven by magnetic disorder (ΔS) [117]. This also shows the important role of the spin order/disorder feature in ΔS and ρ phenomena. In other words, magnetic field application aligns magnetic spins in parallel direction with the applied magnetic field enhancing the ferromagnetic spin ordering. The spin entropy decrease is compensated by the increase in lattice entropy (ΔS) [121] leading to heat release, magnetic polarons formation and resistivity peak around T_c due to carriers scattering by spin-disorder [122].

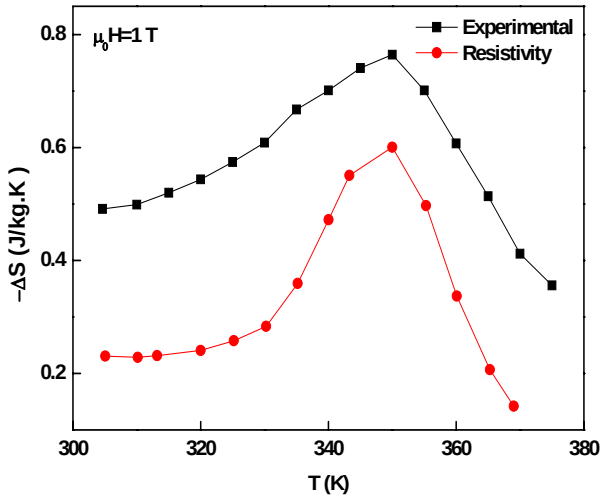

Fig. 9.2: Thermal variation of the experimental ΔS and resistivity based ΔS calculations at 1 T applied magnetic field.

In spite of the similar behavior of experimental *ΔS* and *ΔS (ρ)* curves, the correspondence in values is not achieved. This deviation may be due to an additional contribution of a non magnetic component in *ρ* rather than the spin ordering feature. This non magnetic contribution arises from the electron-phonon interaction induced by lattice polarons [18,115]. In more details, the measured *ρ* consists of two components, a magnetic one (ρ_{sd}) arising from carriers scattering by spin-disorder and a non magnetic component ($\rho_{el\text{-}ph}$) arising from the electron-phonon interaction as proved in ch.5. Therefore, the spin order/disorder common origin of *ρ* and *ΔS* suggests the similar shape of the experimental and the calculated magnetic entropy change (ΔS and $\Delta S(\rho_{sd})$ respectively), while the non correspondence in their values is attributed to the non magnetic resistivity component that damps the total *ΔS(ρ)*.

9.3 Magnetocaloric effect-magnetoresistance correlation

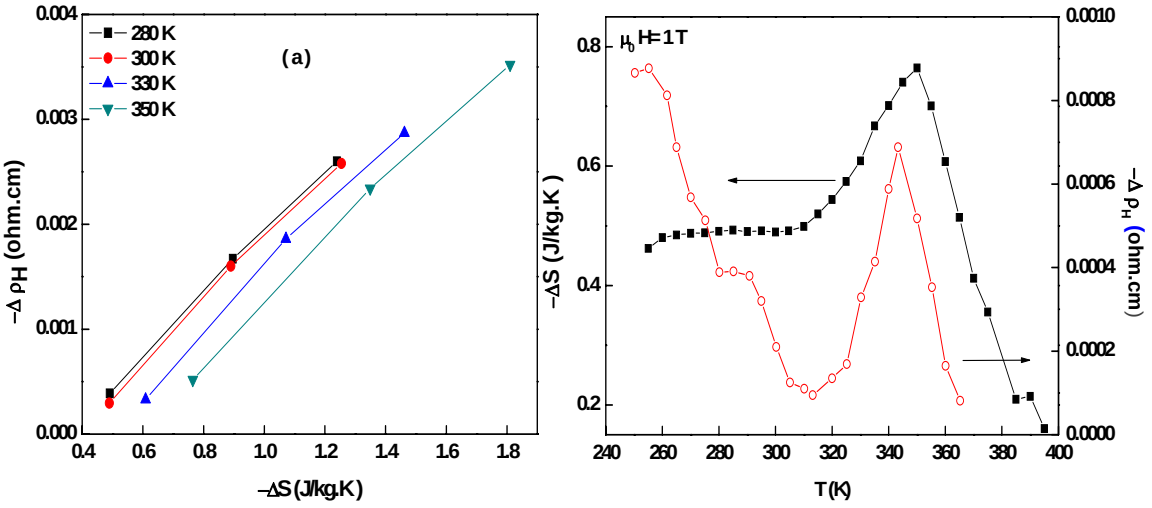

Fig. 9.3: (a) ΔρH vs ΔS relation at different temperatures, and (b) Thermal variation of the experimental ΔS and ΔρH at 1T applied magnetic field.

The proportional relation between ΔS and MR ($\Delta\rho_H$) has been observed in several ferromagnetics as $La_{0.6}Sr_{0.4}CoO_3$, $SrRuO_3$ and $CoPt_3$ [119]. This proportional relation is observed also in the LBMO compound as shown in Fig. 9.3a, revealing the constant relation of $\Delta\rho_H/\Delta S$, with a temperature independent constant ***(K)*** value of $29\text{x}10^{-4}$ $\Omega\text{cmJ}^{-1}\text{Kkg}$. Fundamentally, the constant relation between ΔS and $\Delta\rho_H$ in Eq. 9.3 shows that $\Delta S \approx \Delta\rho_{Hsd}$ due to their common origin of the spin order/disorder feature around T_c, where $\Delta\rho_{Hsd}$ is the MR arising from the spin disorder suppression, and this explains the appearance of ΔS and $\Delta\rho_H$ peaks around T_c in Fig. 9.3b. Despite the similar behavior between ΔS and $\Delta\rho_H$ curves around T_c in Fig. 9.3b, the shape of respective curves is different, i.e., $\Delta\rho_H(T)$ curve looks sharper than the experimental $\Delta S(T)$ curve in agreement with the reported results of $La_{0.825}Sr_{0.175}MnO_3$ [119]. This difference in broadness

suggests the participation of an additional mechanism in the *MR* other than the intrinsic factors [123]. In other words, *MR* around T_c is not totally arising from the spin-disorder suppression (MR_{sd}), but, there are another contributions arising from some effects as Jahn-Teller distortion and electronic phase separation [124]. This supports *Millis et al.* suggestion that the spin ordering or the DE cannot individually explain the CMR [123].The notable difference in behavior at low temperatures between $\Delta\rho_H(T)$ and $\Delta S(T)$ refers to a different mechanism of $\Delta\rho_H(T)$ other than the spin disorder suppression in this temperature range. At low temperatures, the granular nature of the LBMO compound leads to carriers transport through the spin dependent tunneling between grains resulting in a large LFMR [18]. Also, the ferromagnetic ordering at low temperatures excludes the impact of $\Delta\rho_H$ by magnetic polarons due to the magnetic spin-disorder absence that characterizes ΔS, and this explains the deviation in behavior between ΔS and $\Delta\rho_H$ at low temperatures.

In conclusion, the analogy in ΔS(T), ρ(T) and MR(T) indicates the important role of the spin order/disorder feature around T_c in their correlation. This correlation has shown that ΔS scaling by ρ around T_c is meaningful, especially, ΔS can describe the short range spin-order [119] that characterizes resistivity around T_c [125], in addition, ΔS can be well scaled by $\Delta\rho_H$ through a ***K*** factor.

Summary and conclusion

This work is devoted to study the effect of artificial granularity on the magneto-transport properties of $La_{0.7}Ba_{0.3}MnO_3$ manganite compound. These goals have been carried out by introducing secondary phases with different ratio, and size into the $La_{0.7}Ba_{0.3}MnO_3$ compound.

The work involves multiple aims that have been achieved, the effect of (1) secondary phase ratio, (2) secondary phase size and (3) annealing temperature on the magneto-transport properties of the $La_{0.7}Ba_{0.3}MnO_3$ compound. In addition, an investigation discussing the correlation between the magnetocaloric effect and the transport properties in the $La_{0.7}Ba_{0.3}MnO_3$ compound has been performed. These goals have been carried out by introducing secondary phases with different ratio and size with the $La_{0.7}Ba_{0.3}MnO_3$ compound.

The samples were prepared in several steps as it is indicated in the next points:

1- $La_{0.7}Ba_{0.3}MnO_3$ compound was prepared by the sol-gel method.

2- TiO_2 nanotubes were prepared by the electrochemical anodization method.

3- Ni nanowires were prepared by the pulsed electrochemical deposition method.

4- Ni powder and Ag oxide powder were commercial raw.

5- $La_{0.7}Ba_{0.3}MnO_3/xTiO_2$ (x=0, 0.02, 0.04, 0.06 and 0.08), $La_{0.7}Ba_{0.3}MnO_3/Ni_{0.02}$ and $La_{0.7}Ba_{0.3}MnO_3/Ag_{0.02}$ systems were prepared by the solid-state reaction method, where, stoichiometric amounts of the $La_{0.7}Ba_{0.3}MnO_3$ and the secondary phases were mixed, pelletized and sintered at 800°C for 24 hours.

The XRD patterns show the coexistence of TiO_2 secondary phase with the LBMO compound, which reveals their interaction lack. The analysis of these XRD patterns proves the R3c Rhombohedral structure for all composites. Accordingly, TiO_2 is segregated between LBMO grains and accumulated at the boundaries increasing their resistance. This increase in the grain boundaries resistance increases the resistivity and decreases the T_{ms} of the $La_{0.7}Ba_{0.3}MnO_3$ compound with the increasing of TiO_2 content. The increase in grain boundaries resistance promotes the low field magnetoresistance peak of the $La_{0.7}Ba_{0.3}MnO_3$ compound from -3% to -3.3%, -3.5% and -3.7% with the TiO_2 addition for x= 0.02, 0.04 and 0.06, respectively.

On the other hand, the dc magnetization measurements show a T_c constant value for the LBMO compound with the additive TiO_2 that is attributed to the interaction lack. The T_c constant value has kept the same working temperature range concerning magnetocaloric properties. The MCE properties of the LBMO compound show a notable enhancement with the TiO_2 addition, where, the RCP value has been improved from 35 J/kg to 51 J/kg, 47 J/kg, 50 J/kg and 49 J/kg with increasing TiO_2 ratio up to 8 %. Also, the study shows that the annealing temperature can control the secondary phase distribution at grain boundaries which determine their resistance and the related properties. The best results for magnetic and magnetocaloric properties were achieved at high annealing temperature, where, composites annealed at 800°C show higher magnetization and RCP values than those annealed at 600°C.

The secondary phase size effect on the grain boundaries resistance and the related properties has been also studied. The grain boundaries resistance shows a high sensitivity for the introduced interface size. The $La_{0.7}Ba_{0.3}MnO_3$ results show an interface size dependent behavior in the magneto-transport properties. Composites doped with smaller interfaces size exhibit smaller resistivities and T_{ms} values than these doped with larger interfaces size. The LFMR is enhanced with the greater interface size, where, the room temperature MR of the $La_{0.7}Ba_{0.3}MnO_3$ compound (-1.23%) increases to -5.25 % and -7.9 % for Ag NPs and Ag oxide interfaces, respectively. However, the Ni doped composites shows a deviation from this behavior due to the Mn partial substitution in the Ni_{NWs}-LBMO composite. The RCP values are enhanced from 44 J/kg for LBMO to 107 J/kg and 167 J/kg for Ni powder and Ni Nws interfaces introduction, respectively, and 92 J/kg, 94 J/kg for Ag oxide and Ag NPs interfaces introduction, respectively.

In the $La_{0.7}Ba_{0.3}MnO_3$ compound, resistivity, MR and ΔS are observed to exhibit a maximum around T_c, which suggests a possible correlation. This interesting observation has motivated us to study the relation between the magnetocaloric effect and the transport properties in the $La_{0.7}Ba_{0.3}MnO_3$ compound. Results show that the observed similar behavior around T_c is attributed to the spin order/disorder feature that plays the main role in the magnetocaloric-transport properties correlation. However, in spite of this similarity, the correspondence among the experimental ΔS values and ΔS ones based on resistivity calculations is missing because the lattice polarons effect on resistivity as a result of the electron- phonon interaction. The magnetocaloric effect-

magnetoresistance relation was also studied and results show the contribution of additional factors in the magnetoresistance mechanism other than the spin disorder suppression as Jahn-Teller effect and electronic phase separation. According to the results, it can be concluded that the analogy in ΔS, ρ and MR behavior indicates the key role of spin order/disorder feature around T_c in their correlation, and ΔS can be well scaled by ρ around T_c, and by $\Delta\rho_H$ through a K factor.

Finally, from this work it can be concluded that the manganite/secondary phase is an interesting system for simultaneous magnetoresistive and MCE applications, where, all these properties are enhanced with the increase in secondary phase ratio and size.

Conclusiones

En resumen, el presente trabajo se ha centrado en estudiar la influencia del granulado artificial sobre las propiedades de magneto-transporte en la manganita $La_{0.7}Ba_{0.3}MnO_3$, introduciendo distintas fases secundarias en este compuesto.

Los objetivos planteados y alcanzados para lograrlo han incluido el análisis del (1) efecto de la proporción de fase secundaria adicionada a la manganita, del (2) tamaño de dicha fase, y además se ha estudiado como afecta un tratamiento térmico de recocido al magnetotrasporte de la manganita dopada. También se discute la correlación entre el efecto magnetocalórico y las propiedades de transporte presentadas por el compuesto $La_{0.7}Ba_{0.3}MnO_3$.

Las muestras estudiadas se prepararon en etapas sucesivas, tal y como se resume a continuación:

1- La manganita $La_{0.7}Ba_{0.3}MnO_3$ se preparó mediante la técnica sol-gel.

2- Los nanotubos de TiO_2 se fabricaron mediante el método de anodización electroquímica.

3- Los nanohilos de Ni se prepararon mediante el método de deposición electroquímica pulsada.

4- Para el Ni en polvo y la Ag oxidada igualmente en polvo se emplearon productos comerciales.

5- Los sistemas $La_{0.7}Ba_{0.3}MnO_3/xTiO_2$ (x=0, 0.02, 0.04, 0.06 and 0.08), $La_{0.7}Ba_{0.3}MnO_3/Ni_{0.02}$, y $La_{0.7}Ba_{0.3}MnO_3/Ag_{0.02}$ se prepararon mediante reacción de estado sólido, mezclando las cantidades estequiométricas de $La_{0.7}Ba_{0.3}MnO_3$ y de la correspondiente fase secundaria, comprimiendo para formar el pellet, y sinterizando a 800ºC durante 24 horas.

Los difractogramas de rayos X demostraron la coexistencia de la fase secundaria de TiO_2 junto con la correspondiente a la manganita $La_{0.7}Ba_{0.3}MnO_3$, revelando la ausencia de interacción entre ambas fases. El análisis de los difractogramas confirmó la estructura rombohédrica R3c para todos los materiales compuestos. En consecuencia, el TiO_2 se segrega entre los granos de la manganita acumulándose en las fronteras entre ellos e incrementando la resistencia de las mismas. Este incremento hace aumentar la resistividad y decrecer la temperatura de transición de fase metal-semiconductor, T_{ms}, de $La_{0.7}Ba_{0.3}MnO_3$ con el aumento del contenido de TiO_2. El incremento en la resistencia de las fronteras de grano aumenta el valor del máximo de la magnetorresistencia a bajo campo de $La_{0.7}Ba_{0.3}MnO_3$ desde -3% hasta -3.3%, -3.5%, and -3.7% con el incremento de TiO_2 para x= 0.02, 0.04 and 0.06, respectivamente.

Las medidas de la imanación en cc muestran que se mantiene el valor de la temperatura de Curie, T_c, de $La_{0.7}Ba_{0.3}MnO_3$ con la adición de TiO_2. Este resultado se atribuye a la ausencia de interacción entre las dos fases del material compuesto. Al mantenerse T_c constante, el rango de temperatura de interés para las propiedades magnetocalóricas no varía. Pero además, el efecto magnetocalórico se optimiza con la adición de TiO_2, incrementándose la capacidad de refrigeración desde 35 J/kg hasta 51 J/kg, 47 J/kg, 50 J/kg y 49 J/kg, en todos los casos hasta un incremento del 8% de TiO_2.

La temperatura de recocido permitió controlar la distribución de la fase secundaria en las fronteras de grano, que determinan su resistencia y propiedades relacionadas con ella.

Se puede concluir también que las propiedades magnéticas y magnetocalóricas se optimizaron para una alta temperatura de recocido de 800ºC de los materiales bifásicos, obteniéndose valores superiores tanto de la imanación como de la capacidad de refrigeración que los correspondientes a las muestras recocidas a 600ºC.

La resistencia de las fronteras de grano es altamente sensible al tamaño de la fase secundaria adicionada, observándose la dependencia de las propiedades de magneto-transporte con dicho tamaño. Así, las manganitas dopadas con fases de menor tamaño exhiben resistividades y temperaturas T_{ms} menores que las dopadas con fases de mayor tamaño. La magnetorresistencia a bajo campo se incrementa con la interfase de mayor tamaño; el valor para $La_{0.7}Ba_{0.3}MnO_3$ a temperatura ambiente de -1.23% se incrementa hasta -5.25 % y -7.9 % con la adición como fase secundaria de nanopartículas de Ag y de Ag oxidada en polvo, respectivamente. Sin embargo, los compuesto con Ni presentan una desviación de dicho comportamiento debido a la sustitución parcial de Mn en los compuestos manganita-nanohilos de Ni.

Los valores de la capacidad de refrigeración aumentan de 44 J/kg para la manganita hasta 107 J/kg, y 167 J/kg, con la adición de Ni en polvo y nanohilos de Ni, respectivamente. El incremento es menor para la adición como intefase de Ag oxidada en polvo (92 J/kg) y para nanopartículas de Ag (94 J/kg).

La resistividad (ρ), magnetorresistencia (MR) y variación de entropía (ΔS) de $La_{0.7}Ba_{0.3}MnO_3$ presentan un máximo en el entorno de T_c. Este comportamiento sugirió una posible correlación, que ha conducido a estudiarla entre el efecto

magnetocalórico y las propiedades de transporte de la citada manganita. El comportamiento similar con la temperatura alrededor de T_c se ha atribuido a la existencia del orden/desorden de spin en el material como determinante de la correlación entre propiedades transporte-magnetocalóricas. Sin embargo, hay que señalar que a pesar de dicha similitud, no hay clara correspondencia entre los valores experimentales de la variación de entropía y los derivados del cálculos de la resistividad, lo que se puede explicar por el efecto de los polarones de la red sobre la resistividad como consecuencia de la interacción electrón-fonón. La correlación efecto magnetocalórico-magnetorresistencia muestra que en el mecanismo de la magnetorresistencia existe la contribución de otros factores adicionales además además de la supresión del desorden de spin, tales como el efecto Jahn-Teller y separación de fase electrónica. Los resultados obtenidos indican el protagonismo ejercido por el orden/desorden de spin en el comportamiento análogo de ρ,. MR y ΔS alrededor de T_c en su correlación, y que ΔS puede ser escalada por ρ alrededor de T_c, y por Δρmediante un factor K.

Finalmente, se puede concluir que el sistema manganita/fase secundaria presenta gran interés para aplicaciones simultáneas magnetorresistivas y magnetocalóricas, puesto que dichas funcionalidades se optimizan con el incremento de la proporción y tamaño de la fase dopante.

References

1- G. H. Jonker, van santen J. H., physica, 16 (1950) 337.

2- C. Zener, Phy. Rev., 82 (1951) 403.

3- S. Jin, T. H. Tiefel, M. Mccormack, R. A. Fastnacht, R. Ramesh, L. H. Chen, Science, 264 (1994) 413.

4- S. K. Giri , P. Dasgupta, A. Poddar, T. K. Nath, J. Alloy. Compd., 631 (2015) 266.

5- J. Volger, Physica, 20 (1954) 49.

6- V. Sen, N. Panwar, A. Rao, C. K. Hsu, Y. K. Kuo, S. K. Agarwal, Solid State Commun., 145 (2008) 86.

7- W. Li, C. Y. Xiong, L. C. Jia, J. Pu, B. Chi, X. Chen, J. W. Schwank, J. Li, J. Power Sources, 284 (2015) 272.

8- N. Ghosh, S. Elizabeth, H.L. Bhat, G. Nalini, B. Muktha, T.N. Guru Row, J. Solid State Chem., 178 (2005) 120.

9- A. M. Ahmed, A. A. Mohamed, M. A. Abdelateef, H. A. Abd El-Ghany, Rare Metals, 35 (2016) 551.

10- I. Bozovic, J. N. Eckstein, Appl. Surf. Sci., 113 (1997) 189.

11- A. M. Ahmed, M. A. Abedellateef, H. A. Abd El-Ghanny, A. A. Mohamed, Phys. Status Solidi A, 212 (2015) 623.

12- S. Ricote, N. Bonanos, A. Manerbino, N. P. Sullivan, W. G. Coors, J. Mater. Chem. A, 2 (2014) 16107.

13- T. P. Pham, H. N. Luu, H. M. Do, D. T. h Tran, V. K. Nguyen, V. H. Le, X. P. Nguyen, Adv. Nat. Sci.: Nanosci. Nanotechnol., 2 (2011) 025003.

14- S.P. Issac, N.D. Mathur, J.E. Evetts and M.G. Blamire, Appl. Phys. Lett.,72 (1998) 2038.

15- A. M. Ahmed, H. F. Mohamed, A. K. Diab, A. A. Mohamed, A. E. A. Mazen. A. M. Mohamed, Indian J. Phys., 89 (2015) 561.

16- L.W. Lei, Z.Y. Fu, J.Y. Zhang, H. Wang, Mater. Sci. Eng. B, 128 (2006) 70.

17- Z.C. Xia, S.L. Yuan, W. Feng, L.J. Zhang, G.H. Zhang, J. Tang, L. Liu, S. Liu, G. Peng, D.W. Niu, L. Chen, Q.H. Zheng, Z.H. Fang, C.Q. Tang, Solid State Commun., 128 (2003) 291.

18- H. Hwang, S. W. Cheong, N. P. Ong, B. Batlogg, Phys. Rev. Lett. 77 (1996) 2041.

19- Y. Lu, X. W. Li, G. Q. Gong, G. Xiao, A. Gupta, P. Lecoeur, J. Z. Sun, Y. Y. Wang and V. P. Dravid, Phys. Rev. B, 54 (1996) R8357.

20- K. A. Gschneidner Jr., V. K. Pecharsky, A. O. Tsokol, Rep. Prog. Phys., 68 (2005) 1479.

21- S.Yu. Dankov, A.M. Tishin, V.K. Pecharsky, K.A. Gschneidner Jr., Phys. Rev. B, 57(1998) 3478.

22- S. Kallel, N Kallel, O. Pena, M. Oumezzine, Mater. Lett., 64 (2010) 1045.

23- V. K. Pecharsky., K. A. Gschneidner Jr., J. Magn. Magn. Mater., 167 (1997) L179.

24- V. K. Pecharsky, K. A. Gschneidner Jr., Phys. Rev. Lett., 78 (1997) 4494.

25- J. C. Debnath, R. Zeng, J. H. Kim, S. X. Dou, J. Appl. Phys., 107 (2010) 09A916.

26- A. Szewczyk, H. Szymczak, A. Wisniewski, K. Piotrowski, R. Kartaszynski, B. Dabrowski, S. Kolesnik, Z. Bukowski, Appl. Phys. Lett.,77 (2000) 1026.

27- B. Arayedh, S. Kallel, N. Kallel, O. Pena, J. Magn. Magn. Mater., 361 (2014) 68.

28- A. A. Mozhegorov, A. V. Larin, A. E. Nikiforov, The Phys. Met. Metallogr., 105 (2008) 219.

29- W. E. Pickett, D. J. Singh, Phys. Rev. B, 53 (1996) 1146.

30- L. P. Gor'kov, Z. K. Vladimir, Phys. Reports, 400 (2004) 149.

31- E. S. Bozin, X. Qiu, M. Schmidt, G. Paglia, J. F. Mitchell, P. G. Radaelli, T.Proffen, S. J. L. Billinge, Physica B, 385-386 (2006) 110

32- R. J. Radwanski, Z. Ropka, J. Magn. Magn. Mater., 272-276 (2004) 259.

33- E. Rezlescu, C. Doroftei, P. D. Popa, N. Rezlescu, J. Magn. Magn. Mater., 320 (2008) 796.

34- W. H. Meiklejohn, C. P. Bean, Phys. Rev., 102 (1956) 1413.

35- P. M. Woodward, D. E. Cox, T. Vogt, C. N. R. Rao, and A. K. Cheetham, Chem. Matter., 11 (1999) 3528.

36- C. Ritter, R. Mahendiran, M. R. Ibarra, L. Morellon, A. Maignan, B. Raveau, C. N. R. Rao, Phys. Rev. B, 61(2000) R9229.

37- M. Jaime, P. Lin, S. Chun, M. Salamon, P. Dorsey, M. Rubinstein, Phys. Rev. B, 60 (1999) 1028.

38- P. W. Anderson, H. Hasegawa, Phys. Rev., 100 (1955) 675.

39- J. B. Goodenough, Prog. Solid state chem., 5 (1971) 149.

40- H. A. Kramers, Physica, 1 (1934) 182.

41- J. B. Goodenough, Phy. Rev., 100 (1955) 564.

42- V. Goldschmidt, Geochemistry, Oxford University Press, (1958).

43- J. M. D Coey, M. Viret, Advs in Physics, 48 (1999) 167.

44- W. A.Harrison, Solid State Theory ,Dover Publications Inc, New York, (1979).

45- J. S. Griffith, Cambridge University Press, Cambridge, 1964.

46- N. M. Tallan, "Electrical Conductivity in Ceramics and Glass" Part A. New York: Marcel Dekker, Inc., (1974).

47- E. G. Larson, R. J. Arnott, D. G. Wickham, J. Phys. Chem. Solids, 23 (1962) 1771.

48- A. J. Moulson, J. M. Herbert, Electroceramics ,2nd Edition. West Sussex, England: John Wiley and Sons Ltd., (2003)

49- W. Thomson, Proc. R. Soc. London, Ser. A, 8 (1857) 546.

50- M. Baibich, J. Broto, A. Fert, V. D. F. Nguyen, F. Petroff , P. Eitenne, G. Creuzet, A. Friedrich, J. Chazelas, Phys. Rev. Lett., 61 (1988) 2472

51- R. V. Helmolt, J. Wecker, B. Holzapfel, L. Schultz, Kamwer S., Phy. Rev. Lett., 71 (1993) 2331.

52- K. Chahara, T. Ohno, M. Kasai, Y. Kozono, Appl. Phys. Lett., 63 (1993) 1990.

53- S. Ricote, N. Bonanos, A. Manerbino, N. P. Sullivan, W. G. Coors, J. Mater. Chem. A, 2 (2014) 16107.

54- A. M. Tishin, Cryogenics, 30 (1990) 127.

55- V. K. Pecharsky, K. A. Gschneidner Jr., J. Appl. Phys., 86 (1999) 565.

56- R. D. McMichael, J. J. Ritter, R. D. Shull, J.Appl.Phys.73(1993) 6946.

57- J. Mira, J. Rivas, L. E. Hueso, F. Rivadulla, M. A. L.Quintela, J. Appl. Phys., 91 (2002) 8903.

58- M. H. Phan, S. C.Yu, J. Magn. Magn. Mater., 308 (2007) 325.

59- C. Reig, M.D. C. Beltran, D. R. Munoz, Sensors, 9 (2009) 7919.

60- P. P. Freitas, R. Ferreira, S. Cardoso, F. Cardoso, J. Phys.: Condens. Matter, 19 (2007) 165221.

61- D.G. Kuberkar, R.R. Doshi, P.S. Solanki, U. Khachar, M. Vagadia, A. Ravalia, V. Ganesan, Applied Surface Science, 258 (2012) 9041.

62- V. Vega, M.A. Cerdeira, V.M. Prida, D. Alberts, N. Bordel, R. Pereiro, F. Mera, S. García, M. H. Vélez, M. Vázquez, J. Non-Cryst. Solids, 354 (2008) 5233.

63- X. Liu, J. Lin, Y. H. Tsang , X. Chen, P. Hing , H. Huang, J. Alloy. Compd., 607 (2014) 50.

64- D. Alberts, V. Vega, R. Pereiro, N. Bordel, V. M. Prida, A. Bengtson, A. S.Medel, Anal Bioanal Chem., 396:2833 (2010)2840.

65- H. M. Rietveld, J. Appl. Crystallography, 2 (1969) 65.

66- C. V. Vazquez, M. C. Blanco, M. A. L. Quintela, R. D. Sanchez, J. Rivas, S. B. Oseroff , *J. Mater. Chem*., 8 (1998) 991.

67- V. Sen, N. Panwar, A. Rao, C. K. Hsu, Y. K. Kuo, S. K. Agarwal, Solid State Commun., 145 (2008) 86.

68- A. Barnabe, F. Millange, A. Maignan, M. Hervieu, B. Raveau, Chem. Mater., 10 (1998) 252.

69- M. A. L. Quintela, L. E. Hueso, J. Rivas, F. Rivadulla, Nanotechnology, 14 (2003) 212.

70- B. Vertruyen, A. Rulmont, R. Cloots, M. Ausloos, S. Dorbolo, P. Vanderbemden, Mater. Lett., 57 (2002) 598.

71- N. Zhang, W. Ding, W. Zhong, D. Xing, Y. Du, Phys. Rev. B, 56 (1997) 8138.

72- B. x. Huang, Y. h. Liu, X. Yuan, C. J. Wang, R. Z. Zhang, L. M. Mei, J. Magn. Magn. Mater., 280 (2004) 176.

73- A. de Andres, M. G. Hernandez, J. L. Martinez, Phys. Rev. B, 60 (1999) 7328.

74- L. E. Hueso, J. Rivas, F. Rivadulla, M. A. L. Quintela, J. Appl. Phys., 86 (1999) 3881.

75- D. Das, C. M. Srivastava, D. Bahadur, A. K. Nigam, S. K. Malik, J. Phys. Condens. Mat., 16 (2004) 4089.

76- N. F. Mott, E. A. Davis. Electronics Process in Non Crystalline Materials, Second ed., Clarendon Press, Oxford, 1979.

77- M. Viret, L. Ranno, J. M. D. Coey, Phys. Rev. B., 55 (1997) 8067.

78- S. Ravi, M. Kar, Physica B, 348 (2004) 169.

79- N. Mahamdioua, A. Amira, S. P. Altintas, A. Varilci, C. Terzioglu, Physica B, 429 (2013) 12.

80- S. Gupta, R. Ranjit, C. Mitra, P. Raychaudhuri, R. Pinto, Appl. Phys. Lett., 78 (2001) 362.

81- M. Eshraghi, H. Salamati, P. Kameli, J. Alloy. Compd. 437 (2007) 22.

82- T. F. Zhou, G. Li, N. Y. Wang, B. M. Wang, X. G. Li, Y. Chen, Appl. Phys. Lett., 88 (2006) 232508.

83- X. J. Liu, Z. Q. Li, A. Yu, M. L. Li, W. R. Li, B. L. Li, P. Wu, H. L. Bai, E. Y. Jiang, J. Magn. Magn. Mater., 313 (2007) 360.

84- H. J. Kim, S. I. Yoo, J. Alloy. Compd., 521 (2012) 30.

85- S. Karmakar, S. Taran, B. K. Chaudhuri, H. Sakata, C. P. Sun, C. L. Huang, H. D. Yang, J. Phys. D Appl. Phys., 38 (2005) 3757.

86- G. Venkataiah, P. V. Reddy, J. Magn. Magn. Mater., 285 (2005) 343.

87- A. Dutta, N. Gayathri, R. Ranganathan, Phys. Rev. B, 68 (2003) 054432.

88- Y. Fu, Appl. Phys. Lett., **77** (2000) 118.

89- A. Arrott, Phys. Rev., 108 (1957) 1394.

90- S. K. Banerjee, Phys. Lett., 12 (1964) 67.

91- S. G. Min, K. S. Kim, S. C. Yu, H. S. Suh, S. W. Lee, IEEE Trans. Magn., 41(2005) 2760.

92- A. Rostamnejadi, M. Venkatesan, P. Kameli, H. Salamati, J. M. D. Coey, J. Magn. Magn. Mater., 323 (2011) 2214.

93- S. K. Barik, C. Krishnamoorthi, R. Mahendiran, J. Magn. Magn. Mater., 323 (2011) 1015.

94- H. Oesterreicher, F. T. Parker, J. Appl. Phys., 55 (1984) 4334.

95- V. Franco, A. Conde, *Int. J. Refrig*., 33 (2010) 465.

96- V. Franco, C. F. Conde, A. Conde, L. F. Kiss, *Appl. Phys.Lett*., 90 (2007) 052509.

97- V. Franco, J. S. Blazquez, A. Conde, *Appl. Phys. Lett*., 89 (2006) 222512.

98- V. Franco, J. S. Blazquez, A. Conde, *Appl. Phys. Lett*., 100 (2006) 064307

99- M. Pekala, *J. Appl. Phys*., 108 (2010)113913.

100- L. D. Landau, E. M. Lifshitz, Statistical Physics, Pergamon, Oxford, 1967.

101- J. Inoue, M. Shimizu, J. Phys. Lett., 85 (1982) A90.

102- V. S. Amaral, J. S. Amaral, *J. Magn. Magn. Mater*., 272 (2004) 2104.

103- A. Mleiki, S. Othmani, W. C. Koubaa, M. Koubaa, A. Cheikhrouhou, E. K. Hlil, *J. Alloy Compd*., 645 (2015) 559.

104- S. Othmani, M. Bejar, E. Dhahri, E. K. Hlil, *J. Alloy Compd.,* 475 (2009) 46.

105- R. Dhahri, F. Halouni, *J. Alloy Compd.,* 381(2004) 21.

106- R. N. Bhowmik, A. Poddar, R. Ranganathan, C. Mazumdar, J. Appl. Phys., 105 (2009) 113909.

107- R.N. Bhowmik, J. Magn. Magn. Mater., 323 (2011) 311.

108- I. P. Muthuselvam, R. N. Bhowmik, *J. Alloy Compd,.*511 (2012) 22

109- O. A. Shlyakhtin, K. H. Shin, Y. J. Oh, *J. Appl. Phys*., 91 (2002) 7403.

110- Z. Sheng, Y. Sun, X. Zhu, W. Song, P.Yan, J. Phys. D: Appl. Phys., 40 (2007) 3300.

111- W. J. Lu, Y.P. Sun, X.B. Zhu, W. H. Song, J. J. Du, Mater. Lett., 60 (2006) 3207.

112- L. Yan, L. B. Kong, T. Yang, W. C. Goh, C. Y. Tan, C. K. Ong, Md. A. Rahman, T. Osipowicz and M. Q. Ren, J. Appl. Phys., 96 (2004) 1568.

113- M. Pekala, K. Pekala, V. Drozd, J.F. Fagnard, P. Vanderbemden, J. Alloy. Compd., 629 (2015) 98.

114- M. F. Hundley, M. Hawley, R. H. Heffner, Q. X. Jia, J. J. Neumeier, J Tesmer, J. D. Thompson, X. D. Wu, Appl. Phys. Lett., 67 (1995) 860.

115- J. O'Donnell, M. Onellion, M. S. Rzchowski, J. N. Eckstein, I. Bozovic, Phys. Rev. B, Condens. Matter, 54 (1996) R684.

116- B. Chen, C. Uher, D. T. Orelli, J. V. Mantese, A. M. Mance, A. L. Micheli, Phys. Rev. B, 53 (1996) 5094.

117- C. M. Xiong, J. R. Sun, Y. F. Chen, B. G. Shen, J. Du, Y. X. Li, IEEETrans.Magn., 41 (2005) 122.

118- R. Rawat, I. Das, J. Phys.: Condens. Matter, 13 (2001) L379.

119- N. Sakamoto, T. Kyomen, S. Tsubouchi, M Itoh, Phys. Rev. B, 69 (2004) 092401.

120- M. Patra, K. De, S. Majumdar, S. Giri, Appl. Phys. Lett., 94 (2009) 092506.

121- S. Lee, M. S. Anwar, F. Ahmed, B. H. KOO, Trans. Nonferrous Met. Soc. China, 24 (2014) 141.

122- T. S. Tripathi, R. Mahendiran, A. K. Rastogi, J. Appl. Phys., 113, (2013) 233907.

123- A. J. Millis, P. B. Littlewood, B. I. Shraiman, Phys. Rev. Lett., 74, (1995) 5144.

124- J. Burgy, E. Dagotto, M. Mayr, Phys. Rev. B, 67 (2003) 014410.

125- M. E. Fisher, J. S. Langer, Phys. Rev. Lett., 20 (1968) 665.

Publications and attended conferences

PhD thesis outcome publications

- **Abd El-Moez A. Mohamed**, V. Vega, M. Ipatov, A. M. Ahmed, B. Hernando, "Magnetoresistive and magnetocaloric response of manganite/insulator system", *J. Alloys Compd. 657 (2016) 495*.
- **Abd El-Moez A. Mohamed**, V. Vega, M. Ipatov, A. M. Ahmed, B. Hernando, "Annealing temperature effect on magnetic and magnetocaloric properties of manganites", J. *Alloys Compd. 665 (2016) 394.*
- **Abd El-Moez A. Mohamed**, B. Hernando, A. M. Ahmed, "Magnetocaloric -transport properties correlation in doped manganites", *J. Solid State Commun. 233 (2016) 15.*
- **Abd El-Moez A. Mohamed**, Mohamed A. Mohamed, V. Vega, B. Hernando, A. M. Ahmed, "Tuning magnetoresistive and magnetocaloric properties via grain boundaries engineering in granular manganites", *RSC adv. 6 (2016) 77284.*

Related publications

- **Abd El-Moez A. Mohamed**, B. Hernando, "The expected low field magnetocaloric effect of $La_{0.7}Ba_{0.3}MnO_3$ manganite at room temperature", *Phys. Lett. A,* 380 (2016) 1763.
- **Abd El-Moez A. Mohamed**, B. Hernando, A. M. Ahmed, Magnetic, magnetocaloric and thermoelectric properties of nickel doped manganites, *J. Alloy. Compds, 692 (2017) 381*.

- **Abd El-Moez A. Mohamed,** B. Hernando, M. E. Díaz-García, Room temperature magneto-transport properties of $La_{0.7}Ba_{0.3}MnO_3$ manganite, *J. Alloy. Compds, In press, DOI* 10.1016/j.jallcom.2016.11.177.

Attended conferences and congresses related to this PhD thesis

- The 2nd international conference on Recent trends in Nanomagnetism, Spintronics and their applications (RTNSA), Palacio Barrena, Ordizia (Gipuzkoa), Spain 2015.
- Donostia International Workshop on Energy, Materials and Nanotechnology (DINEMN), Donostia-San Sebastian, Guipuzkoa, Spain, 2015.
- 20th International Conference on Solid Compounds of Transition Elements (SCTE 2016), Zaragoza, Spain, 2016.
- XIV Congreso Nacional de Materiales, Gijón, España, 2016.
- Solitons and Skyrmion Magnetism (Sol-SkyMag 2016), Donostia-San Sebastian, Gipuzkoa, Spain, 2016.

Financial support and scholarships

- The own financial support was provided by the Egyptian Ministry of Higher Education.
- Work and conferences attendance financial support was provided by MAT201347231-C2-1-P, MINECO MAT2013-48054-C2-2-R, and FC-15-GRUPIN14-085 research projects.